Jörg Krug, BSc

Main Influences on Air Spring Stiffness

Master Thesis for the Acquirement of the Academic Degree of
Master of Science

Graz University of Technology

Faculty of Mechanical Engineering and Economic Sciences

Field of Study: Production Science and Management

Institute of Lightweight Design

Ass. Prof. Dipl.-Ing. Dr.techn. Moser

Graz, 2015

In Cooperation with:

Siemens AG Österreich

STATUTORY DECLARATION

I declare that I have authored this thesis independently, that I have not used other than the declared sources / resources, and that I have explicitly marked all material which has been quoted either literally or by content from the used sources.

…… ……..

date (signature)

Acknowledgement

First, I would like to thank my wife for her endless love and patience, for driving me on when I was ready to give up and for everything else. To my daughter Karolina for making me smile each and every day and for showing me how much richer my life has become since she joined us.
Then, I would like to thank all my family for believing in me and supporting me all these years and also for raising me to be who I am today.
Thanks to all my colleagues at the university, to Ass. Prof. Dipl.-Ing. Dr.techn. Moser for approval of this thesis topic and his leadership and especially Dipl.Ing. Markus Götz who supported me and provided me with direction throughout the whole writing process.

Abstract

The motivation to write this thesis stems from the growing demand for faster and more accurate manufacturing of air springs for railed vehicles. At the moment, air springs are developed using different empirical methods. For instance, a prototype is manufactured, tested and tweaked, then re-tested etc. until the air spring's characteristics comply with the requirements. Since these methods consume excessive time and money, the industry has been pushing for development to be optimised. To address this issue, a first model for a finite-element simulation was developed by Marco Talasz. In the paper at hand, his model was developed further and adapted for a comparison of three different air spring models. The main focus of this thesis is the simulation and evaluation of the different influences on the axial, lateral and torsional stiffness. These influences include the different material models and the geometry of the air spring. Also, a more detailed model for the examination of occurring damage has been developed and tested. Options for further research are presented in the concluding chapter.

Kurzfassung

Den Anstoß zu dieser Masterarbeit gab die steigende Nachfrage nach schnellerer und genauerer Herstellung von Luftfedern für Schienenfahrzeuge. Im Moment werden Luftfedern mit verschiedenen empirischen Methoden entwickelt. Eine dieser Methoden ist das Fertigen eines Prototyps mit anschließenden Tests und das Wiederholen dieses Prozesses, bis die Luftfeder die angeforderten Eigenschaften besitzt. Nachdem diese Art der Herstellung mit immensem Zeitaufwand und daher hohen Kosten verbunden ist, verlangt die Industrie nach optimierten Entwicklungsmethoden. Um diese Forderungen zu erfüllen wurde von Marco Talasz bereits eine Masterarbeit veröffentlicht, in der ein erstes Finite-Elemente-Modell zur Simulation der Balg-Eigenschaften entwickelt wurde. Aufbauend auf diesem Modell wird die Finite-Elemente-Simulation in dieser Arbeit weiterentwickelt und für drei verschiedene Luftfedermodelle angepasst. Der Hauptfokus dieser Arbeit liegt auf der Simulation und Bewertung der Einflüsse – verschiedene verwendete Materialmodelle sowie Geometrieeigenschaften) auf die axialen, lateralen und torsionalen Steifigkeiten der Luftfedern. Zusätzlich wird für die Untersuchung von auftretenden Schädigungen ein Detailmodell entwickelt und getestet. Abschließend wird ein Ausblick auf zukünftige Forschungsmöglichkeiten gegeben.

Table of Contents

1 Introduction

The company Siemens AG, Rail Systems Division, uses a large variety of air spring systems in their railed vehicles. In this thesis, three different models will be simulated and compared to each other as well as to the measurement data. The air spring is part of the secondary spring system and is used as suspension between the bogie frame and the car body. Prior to this work, another Master Thesis, titled "Simulation der Bauteilsteifigkeit eines Elastomer-Faser-Verbundes", was conducted by Marco Talasz, whereupon this thesis will be based. In this prior work, a simulation model using the finite element method was developed to simulate different aspects of the air spring like the diameter, internal pressure and so on. In this current work, the stiffness in axial, lateral and torsional direction is the main focus. To get sufficient results, a new and improved simulation model had to be developed and the different parts of the air spring had to be analysed with regard to their influence on the stiffness.
The whole project was launched for two reasons:
Firstly, the manufacturing of air springs needs to be optimised. So far, manufacturers have been relying on an inefficient best-guess approach, drawing on experience from prior projects and involving extensive testing after the first manufacturing stage. Springs are manufactured, tested, tweaked, tested, tweaked etc. until they fulfil the specifications defined by Siemens AG. A simulation of the air spring characteristics which could be done before manufacturing the first prototype would accelerate the whole process and save the manufacturer time as well as money.
Secondly, Siemens would like to use the simulations for lifespan estimations of the different air spring models. These simulations will also have to deal with problems of the air springs which occurred during use. Since these problems mostly arise in specific places, the air springs have to be investigated and the cause of these problems has to be found. The simulation of the stiffness of the air spring is the first step in this process.

1.1 Aim of the Work

To develop a simulation, like the one mentioned above, all the influences on the characteristics, major and minor, have to be understood and factored into the development of the programme. The fundamentals were already covered in Marco Talasz's thesis and will be used in this work. The main goal of this thesis will be to define and fully understand the major influences on the axial, lateral and torsional stiffness of an air spring used in railed vehicles. This also requires building a

sufficiently accurate FE-model which can support all the required tests to first define and afterwards verify or disprove the different approaches.

The goals are defined as follows:

- Development of an FE-model for simulation of stiffness
- Definition of possible influences on air spring stiffness
- Simulation of axial stiffness
- Simulation of lateral stiffness
- Simulation of torsional stiffness
- Comparison of stiffness data from simulations with actual measurements (carried out by Siemens AG)
- Definition of minor and major influences on air spring stiffness

1.2 Course of Action

This thesis consists of two main parts:
First, there will be some literature research, which will cover the history and fundamentals of air spring systems in railed vehicles and determine important input parameters for the simulation software. For the further use in a simulation software, different characteristics of the air spring have to be analysed in detail and the data has to be prepared for the software.
These main characteristics are:

- Material characteristics of the elastomer-cord composite.
    - Characteristics of the rubber.
    - Characteristics of the cord inlays.
- The geometrical form of the air spring.
    - Changes during manufacturing.
    - Before and after inflation.
    - Foldovers at clamping ring and rim.

Furthermore, different parts of the simulation software have to be tested and assessed to ascertain the best possible outcome. This will be done by studying the different help and example files of MSC Marc Mentat as well as testing the different possibilities in simulations.

These features include:

- Definition of contact between the different contact bodies
    - Segment-to-segment contact
    - Node-to-segment contact
- Material Model
    - Elastomer
    - Cord
- Element
    - Type
    - Size
- Method of result evaluation

The knowledge gained from prior research will be used for the development of a suitable simulation model. For the simulations, the software MSC Marc Mentat was selected because of its superiority compared to similar software regarding simulation of nonlinear geometric and material behaviour.

The second part is the main part of the work. The model developed in part one of the thesis will be used to simulate and evaluate influences on the stiffness of the air spring. The results will then be classified into minor and major influences on the stiffness.
For the evaluation and interpretation of the results, graphs and calculations done in MS Excel will be used.

2 Bogies in Railed Vehicles

A railed vehicle's bogie is the connection between the car body and the rails. The bogie has many functions, the majority of which are essential for the function of the whole railed vehicle.
Bogies perform the following functions:

- Bear the weight of the whole railed vehicle
- Run stably on straight as well as curved tracks
- Absorb most of the vibrations and thus improve comfort for the passengers
- Minimise track irregularities and reduce the forces between wheels and tracks[1]

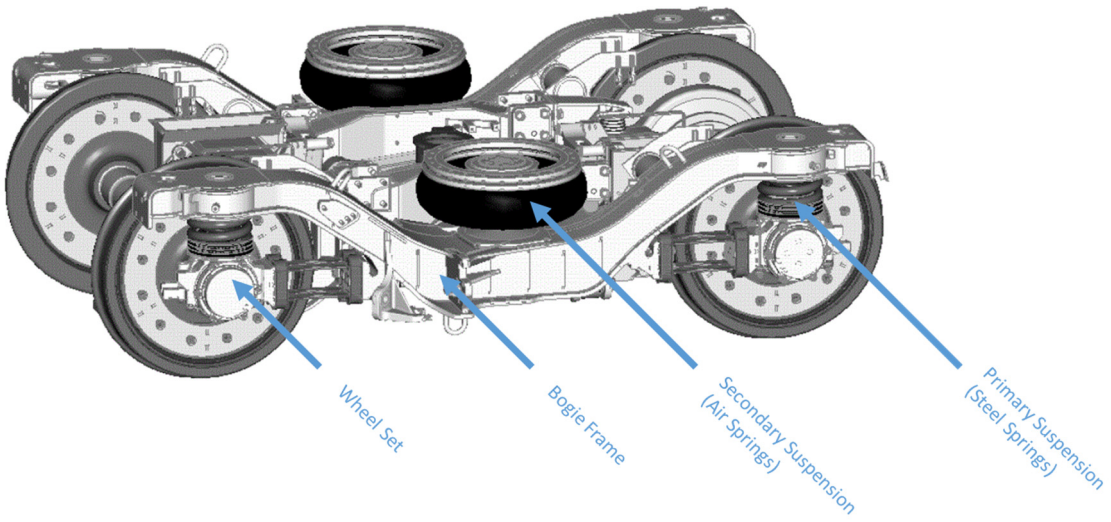

Figure 2-1: Example of a bogie and its main parts.[2]

2.1 Wheel Set

The wheel set consists of the wheel set axle and 2 force-fitted wheels. The axle mounts the wheel set bearing, the attachments for the brake disks and the drive carrier. The wheels mostly consist of only one component. Modern railed vehicles sometimes even use sound absorbers that come in different designs.
The bearings are normally roller bearings and only older designs still use friction bearings.[3]

[1] (Okamoto, 1998)
[2] (Haigermoser, 2002, p. 183)
[3] (Haigermoser, 2002, pp. 183-185)

2.2 Suspension

As shown in the figure above (Figure 2-1), the primary suspension is located between the wheels and the bogie frame. The secondary suspension connects the bogie frame to the car body. The two suspension systems fulfil different functions: The secondary is mainly responsible for passenger comfort, the primary for the stability of the whole construction as well as for bearing all the weight.[4] The secondary suspension is shown here as a combination of two air springs. This kind of suspension evolved over time. The first designs with suspension only had laminated steel springs. Afterwards designs were developed where steel springs were and still are used. In the 1960s the first air suspension was introduced. Since then, it has become a standard fitting for passenger vehicles.[5]

2.3 Bogie Frame

The design of the bogie frame is predefined not only by the drive, brake, suspension and wheel sets, but also by the dimensions of the vehicle body. The frame can either be an H-form or a closed form. The bogie frame in modern railed vehicles is built by welding metal sheets and edge profiles or it can even be cast in one piece.
The bogie frame's torsional stiffness is very important as a safeguard against derailment of the vehicle.[6]

[4] (Haigermoser, 2002, pp. 195-201)
[5] (Railway Technical Web Pages, 1998)
[6] (Haigermoser, 2002, p. 204)

3 Air Springs in Railed Vehicles

3.1 Air Spring Characteristics

Characteristics of air springs in general are:

- Spring characteristics curve is linear
- Spring stiffness is load-dependent
- Automatic levelling is possible
- Internal damping exists
- Stiffness is reduced by increasing volume[7]

3.1.1 Functionality

Air springs are gas springs and thus use the compressibility of air as suspension.
The stiffness of an air spring depends on two factors:

- Compressibility of air
- Change of effective area A_{eff}[8]

The force in an air spring behaves according to the following formula (3.1):

$$F = p_i * A_{eff} \qquad (3.1)^{8}$$

[7] (Prehofer, 2014, p. 22)
[8] For this and the following, see (Haigermoser, 2002, p. 199)

During compression of the bellows, the effective area changes and the stiffness of the air spring behaves as follows:

$$c = \frac{dF}{dz} = \frac{d(p_i * A_{eff})}{d_z} = p_i * \frac{dA_{eff}}{dz} + \frac{dp_i}{dz} * A_{eff} \quad (3.2)^8$$

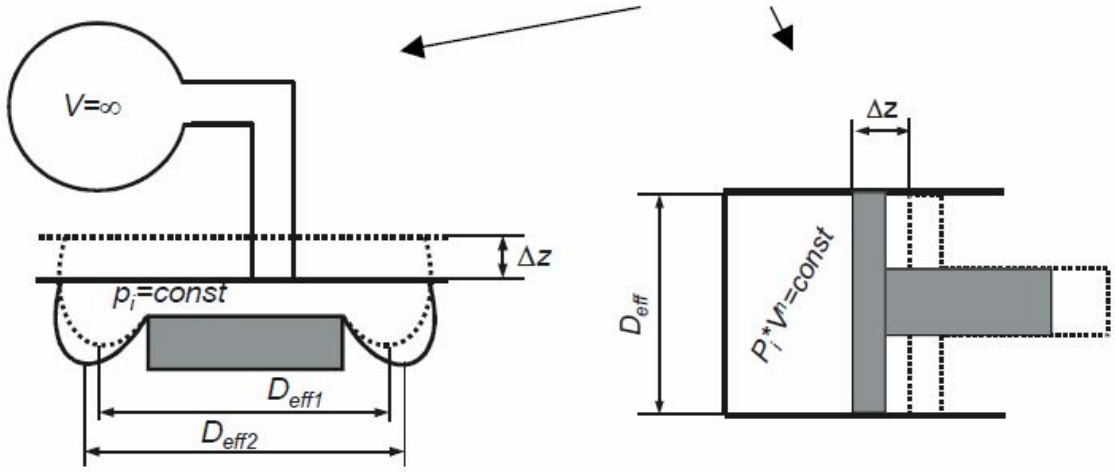

Figure 3-1: Compression of an air spring and its influence on the stiffness8

$$p * V^n = const \quad (3.3)^8$$

If the approach above (3.3) is combined with the formula for the stiffness of an air spring (3.2), then a new conclusion is reached:

$$c = p_i * \frac{dA_{eff}}{dz} + n * (p_a + p_i) * \frac{{A_{eff}}^2}{V} \quad (3.4)^8$$

3.1.2 Safety

The following illustration (Figure 3-2) shows the exploded view of a secondary suspension system designed by ContiTech AG. The different parts of the system are described with regard to their functionality as safeguards.

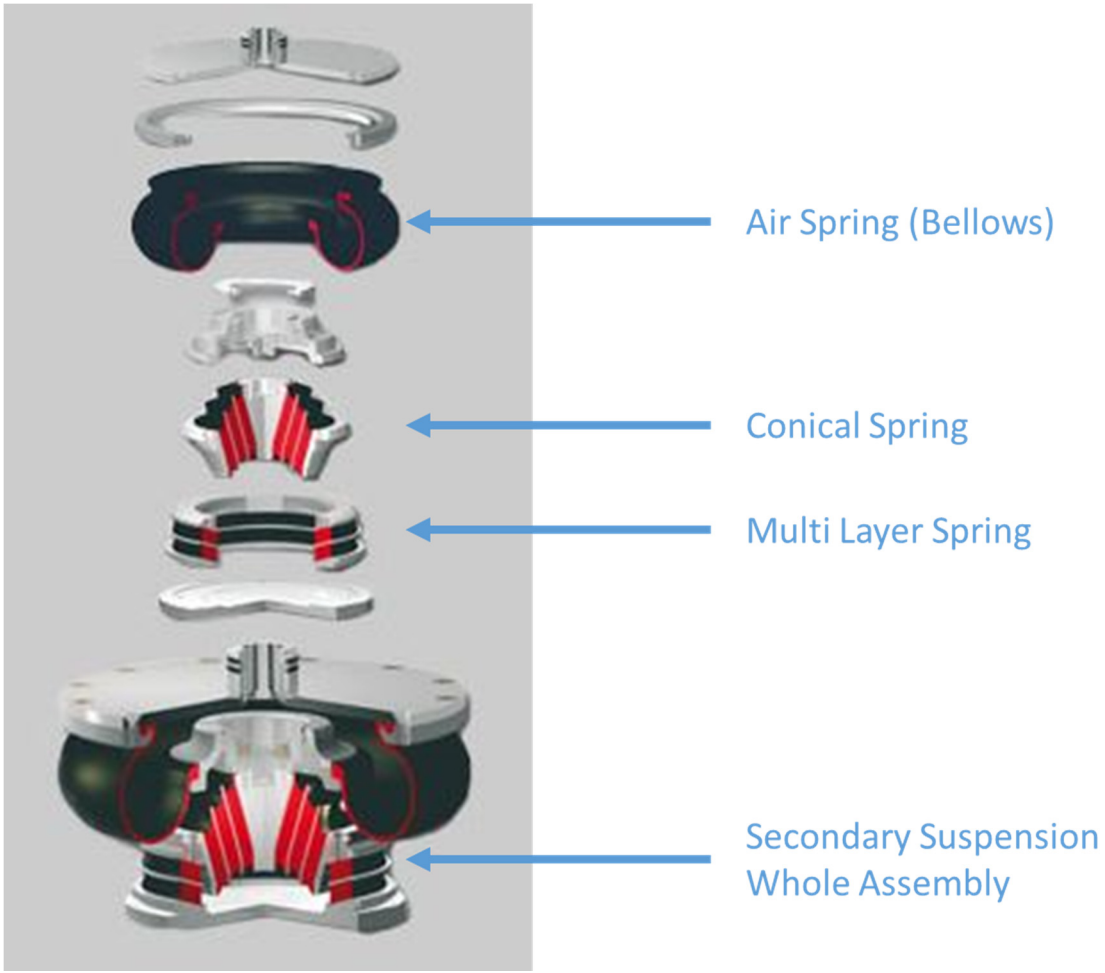

Figure 3-2: Secondary suspension system – Exploded view[9]

Conical springs facilitate a large variation in vertical and horizontal stiffness within a confined space. They often eliminate the need for an auxiliary damper.[10]
The spring acts as the emergency spring for vertical translations as well as rotations around the vertical axis.

Multi-layer springs ensure maintenance-free bearing of primary and secondary suspension systems.[10]The multi-layer spring acts as the horizontal safeguard in case of emergency.[11]

[9] (Secondary Suspension Systems - Suspension Systems for Rail Vehicles, Contitech AG)
[10] (ContiTech AG, 2006)
[11] (Prehofer, 2014, p. 23)

3.2 Air Spring Designs

3.2.1 Double Convoluted Air Springs

This air spring type was used in vehicles at the beginning of air spring development. Today, it is still in use in elevators and as a replacement for the classical pneumatic cylinders, but its use in vehicles has come to an end.[12]
The key feature of this spring is its high-lift capability.[13]
A sectional view of a double convoluted air spring can be seen in Figure 3-3. Both ends are being held in place by clamping rings.

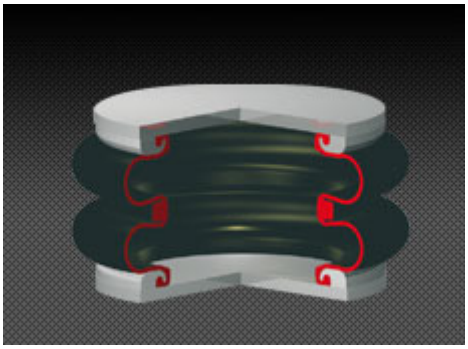

Figure 3-3: Double convoluted air spring[13]

3.2.2 Rolling Lobe Air Spring

This special air spring is used in low-floor bogies with extreme spatial limitations and in trams.[13]Rolling lobe air springs can be either guided (Figure 3-5) or not guided (Figure 3-4). Neither design has a clamping ring, instead they have a bulge on both ends of the bellows. The guided lobe air spring offers additional load capacity as well as more protection against harmful external influences. [14]

[12] (Pahl, 2002, p. 58)
[13] (Air Spring Designs - Secondary Suspension Systems, Contitech AG)
[14] (Talasz, 2013)

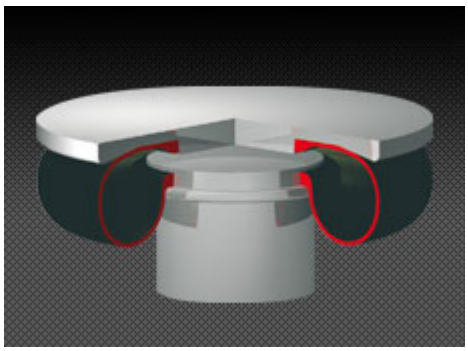

Figure 3-4:Rolling lobe air spring[13]

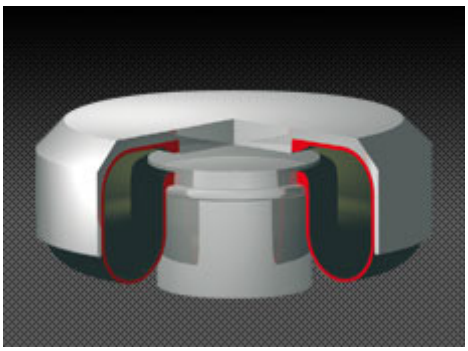

Figure 3-5:Guided lobe air spring[13]

3.2.3 Convoluted Air Spring

The convoluted air spring is prevalent in modern bogies used in high-speed trains and in Metro systems as well as in bolsterless bogies. The key feature which makes this spring perfect for those uses is its extra high lateral deformability.[13]
In Figure3-6, the sectional view of a convoluted air spring is shown. One end of the bellows is held in place by a clamping ring, the other end has a bulge and no clamping ring.

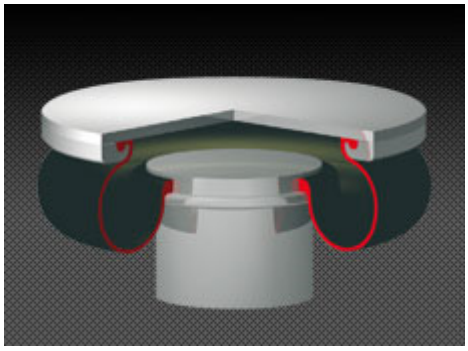

Figure3-6:Convoluted air spring[13]

3.2.4 Belted Air Spring

The belted air spring's key features are its high load-bearing capacity as well as good lateral deformability. It is intended mainly for bolster bogies.[13]In the sectional view of a belted air spring shown below (Figure 3-7), the bulges on both sides of the bellows can be seen. No clamping rings are used for this spring.

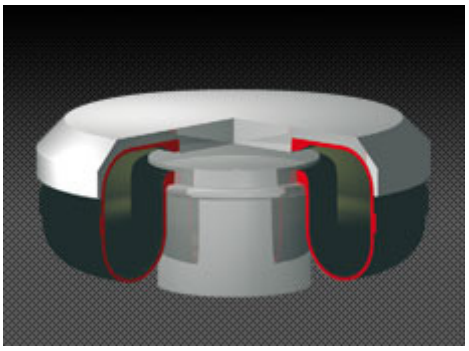

Figure 3-7: Belted air spring[13]

4 Air Springs in this Paper

In this thesis, three different types of air springs will be simulated, evaluated and then compared to the measurements of each specific spring. The three models will be termed Model A, Model B and Model C in this thesis. All three models are used in railed vehicles by Siemens AG.

4.1 The Air Spring System

All three air springs are convoluted air springs, as described in 3.2.3, and have some similarities as well as differences.

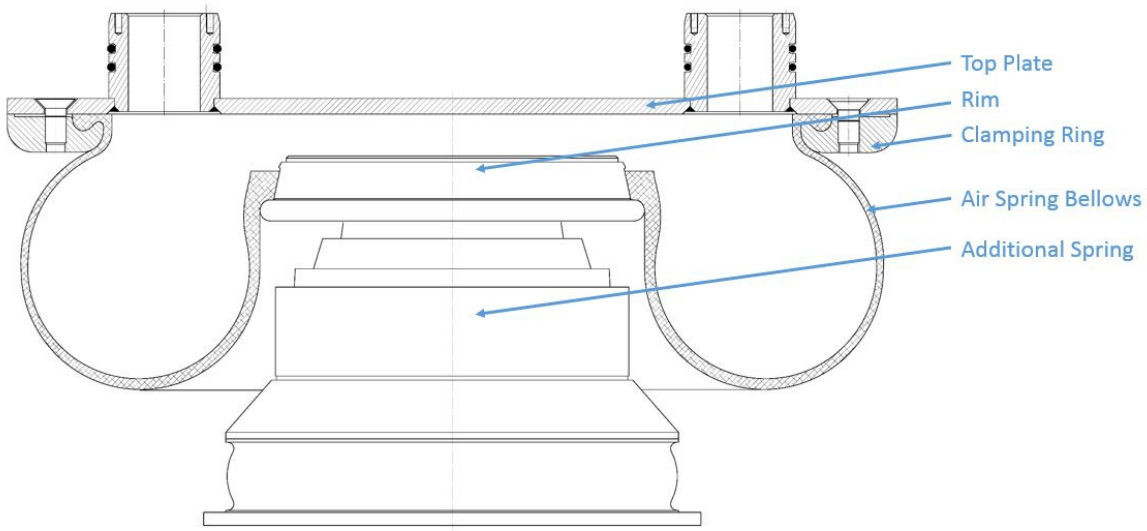

Figure 4-1: Sectional view of an air spring system (GMT, Art. Nr. 170063)[15]

The air spring system shown above (Figure 4-1) is similar to the air springs in this paper in the way that the clamping ring is screwed to the top plate and holds on to one end of the bellows. The other end has a bulge and is in contact with the rim, but it is not held in place by an extra element like a clamping ring.

4.2 The Air Spring

All three air springs consist of a bellows and two steel wire-cores. The bellows itself is based on an elastomer and cord inlays. The cord is the reinforcement and main

[15] (GMT GmbH, Primär- und Sekundärfederung - Schienenfahrzeuge, 2010, p. 20)

carrier material. At both wire-cores, there are foldovers, which means that the elastomer-cord mix entwines the cores. All these parts can be seen in the sectional view of the air spring (Figure 4-2).[16]

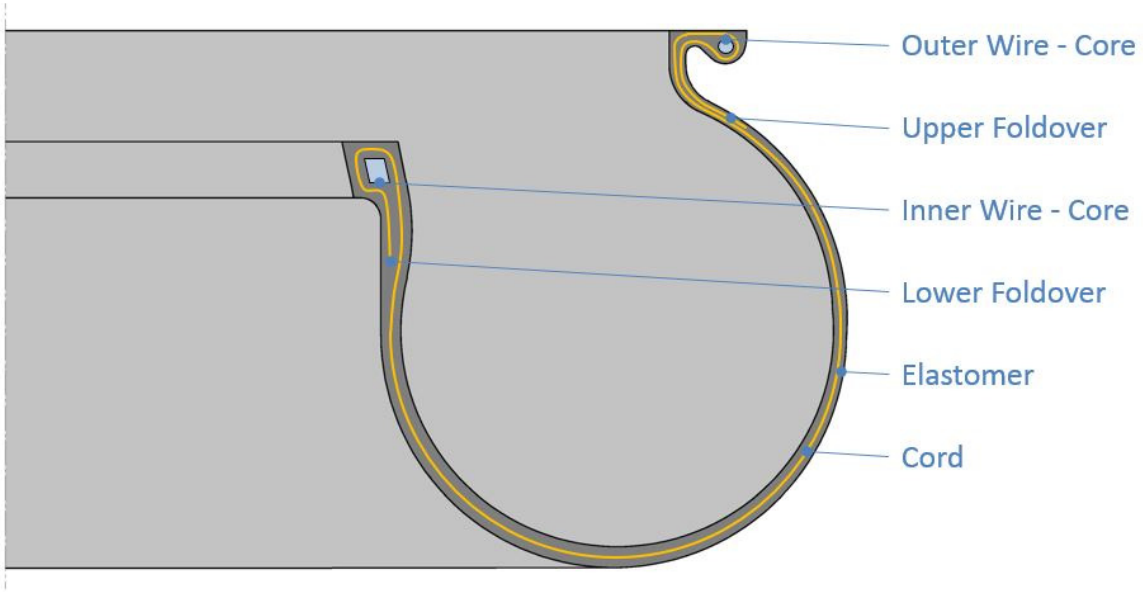

Figure 4-2: Sectional view of an air spring[17]

There are some differences in the geometry of the three models. These differences will be shown in the next section.

Model	Diameter inner Steel Wire-Core	Diameter outer Steel Wire-Core	Strap Length	Largest Diameter	Maximum Working Pressure
Model A	277 mm	558 mm	475 mm	727 mm	7.0 bar
Model B	284 mm	564 mm	495 mm	735 mm	7.0 bar
Model C	254 mm	533 mm	375 mm	670 mm	6.0 bar

Table 4-1: Geometry parameters of the different air spring models

The diameters of the steel wire-cores were taken from the documentation as well as the largest diameter of the air spring at each air spring's specific maximum working pressure. The strap length was measured by the author of this paper. This was done using strips that were cut out of the air springs. The strap length in this thesis is

[16] (Talasz, 2013, p. 11)
[17] (Talasz, 2013, p. 12)

defined as the length of the air spring bellows starting at the inner steel wire-core at the extension of the bulge and ending at the spot that is in contact with the upper plate. In Figure 4-3, the strap length is represented by the yellow line and the blue arrow shows the direction.

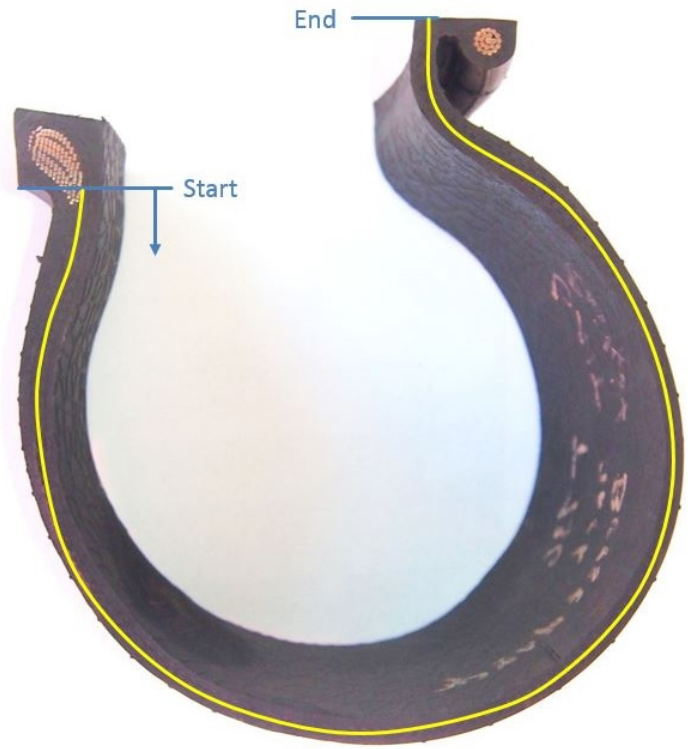

Figure 4-3: Definition of strap length

4.3 Material Properties

4.3.1 Elastomer

The elastomer takes up most of the volume of the air spring, but due to its low stiffness, on its own it cannot withstand the high loads that the air spring has to absorb during operation. The most common solution to this problem is to use the elastomer in combination with a load carrier material. In the case of the air spring, the carrier material is the cord described in chapter 4.3.2.

The typical properties of an elastomer are high elongation and only minimal plastic deformation after removal of the outside forces. The elongation can be up to ten times the length of the original. These properties are mainly influenced by the mixture of natural and synthetic rubber, because the natural rubber, also called caoutchouc, has plastic characteristics and does not behave like the final product. A chemical-

technical process initiates the linkage of the molecules and thus makes the rubber elastic. The number of these links has a defining influence on the properties of the final product.

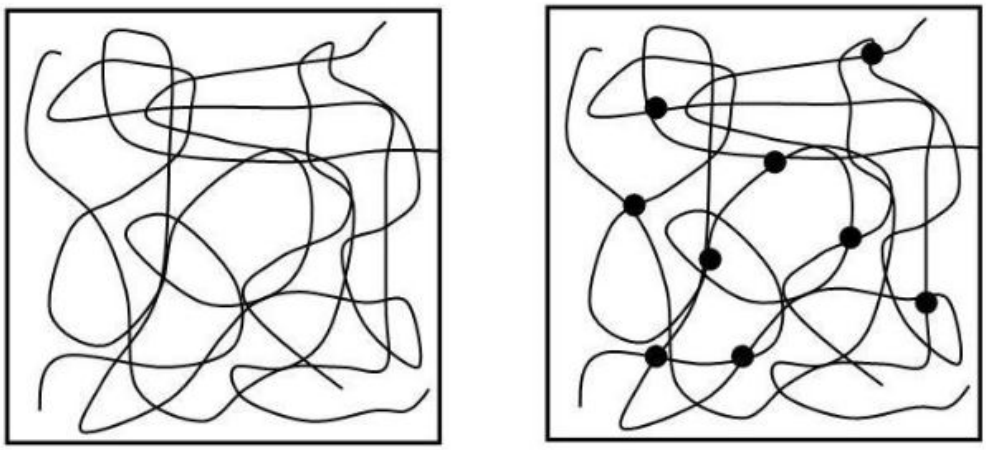

Figure 4-4: Schematic display of the linkage of the molecules[18]

The development of these links is shown in the pictures above (Figure 4-4). If the number of the links is lower than the optimum, the material is still plastic, but if it gets too high, the elasticity decreases rapidly. The pressure, temperature and time during this vulcanisation influence the outcome heavily.[19]

An example of criteria that an elastomer used in air springs has to fulfil after vulcanisation can be seen in the following table (Table 4-2):

Characteristic	Value Range	Unit	Test Standard
Hardness	58-63	Shore A	DIN 53 505
Density	1,13-1,16	g/cm^3	DIN 1183 T1
Flexibility of Shock	36-42	%	DIN 53 512
Tear-Growth Resistance	Min. 12,5	MPa	DIN 53 504
Elongation at Break	Min. 370	%	DIN 53 504

Table 4-2: Criteria for the rubber mixture[20]

[18] (Lehrstuhl Physikalische Chemie Universität Köln, 2009, p. 6)
[19] (Lehrstuhl Physikalische Chemie Universität Köln, 2009, pp. 3-6)
[20] (GMT GmbH, Datenblatt, 2008)

A tensile test was conducted on the material used in the air spring which was tested by Marco Talasz. The results of the test are displayed in the following table (Table 4-3):

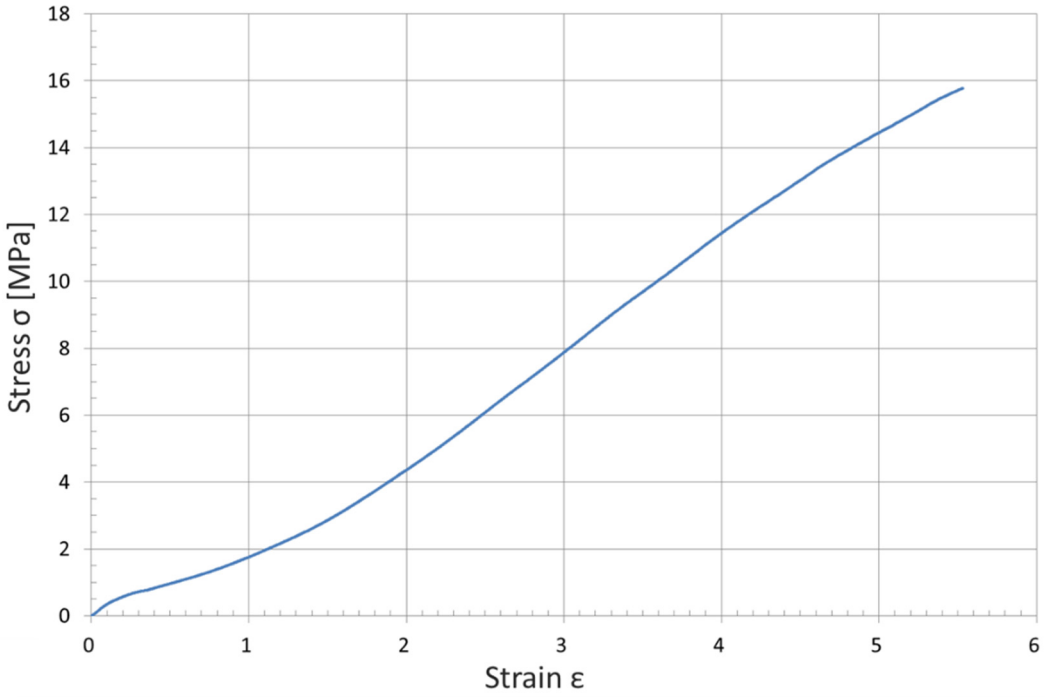

Table 4-3: Stress-strain curve of the elastomer

Since there is no adequate documentation of the elastomer properties used in the three different air spring models and since it is reasonable to assume that the influence of the elastomer is very small, the same material properties will be used for all three models. The influence of the elastomer properties on the stiffness will be shown in chapter 8.1.1.

4.3.2 Cord

The cord is the main carrier material in air springs. It consists of two polyamide 6.6 wires which are twisted together. The polyamide 6.6 is made from polycondensation of hexamethylene diamine (HDMA) and adipic acid. Adipic acid is made from benzene, and HDMA is produced from either butadiene or from propylene.[21] The filaments are manufactured by first melting the above materials and then pressing

[21] (PCI Nylon, 2011)

them through small jets. After cooling, the filaments have low resistance at high elongations. To increase the resistance, the wire is stretched up to six times its original length. During this process, the resistance is increased from about 90 MPa up to 950 MPa. At the same time, the elastic modulus rises from a range of 1.6-3.7 GPa up to about 6 GPa and thus gives the polyamide cord its final characteristics.[22]
The direction of the cord inlays in the elastomer can change the characteristics of the air spring drastically, as can be seen in the following picture (Figure 4-5):

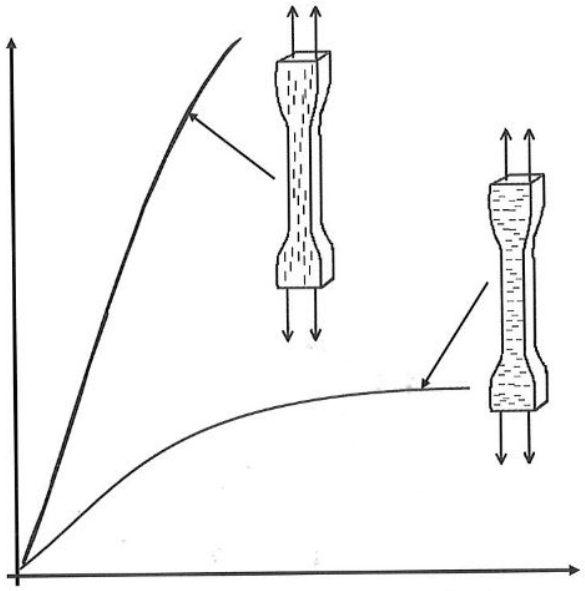

Figure 4-5: Impact of the direction of the cord inlays in the elastomer matrix

The three air springs used in this paper all have four cord layers which form a multidirectional laminate.[23] The structure consists of two layers of elastomer on the outside of the air spring and four layers of cord embedded in the elastomer in-between. These four layers always have a layer with positive angles next to one with negative angles.
In conclusion, the properties of cord-elastomer composites offer high resistance, high stiffness and great reliability even in extreme conditions.[24]

In the following course of this paper, the terminology rebar will often be used. Rebar is more commonly known as a description for steel reinforced concrete but the program MSC Marc Mentat uses the term for any reinforcing material such as the cord in this model. In this thesis, the term rebar is always equivalent to the cord – material.

[22] (Röthemeyer & Sommer, 2006, p. 824)
[23] (Wahl, 2010, p. 14)
[24] (Wahl, 2010, p. 12)

The main differences between the three air spring models concerning the cord are:

- Rebar angle
- Number of cord strings per length unit

Model	Original Rebar Angle	#/m
Model A	15°/-15°	950
Model B	18°/-18°	1100
Model C	7°/-7°	1500

Table 4-4: Cord parameters of the different air spring models

The original rebar angles were taken from the documentation of the air springs, the number of cord strings per length unit was measured by cutting out a small part of the specific air spring at a position where the diameter of the air spring correlates with the diameter of the winding cylinder, counting the strings and upscaling the number for the whole air spring.
These angles were also verified during the measurement of the rebar angles along the strap length, as described in the following chapter (4.3.2.1).

4.3.2.1 Rebar Angle along Strap Length

The rebar angle along the contour has to be determined, too. Therefore, a strip of the bellows was roughened and layers of the elastomer were removed, until the cord was exposed. The following picture shows the air spring strip after removing the upper layers of the elastomer:

Figure 4-6: Air spring after preparation for determination of the rebar angle

Then, the rebar angle was determined for the different cord threads. The measurements were taken about every centimetre along a path following the strap length as defined in chapter 4.3.1 (Figure 4-3). The lines for measuring the angles are

marked in blue and the path is shown in yellow in the detailed image below (Figure 4-7).

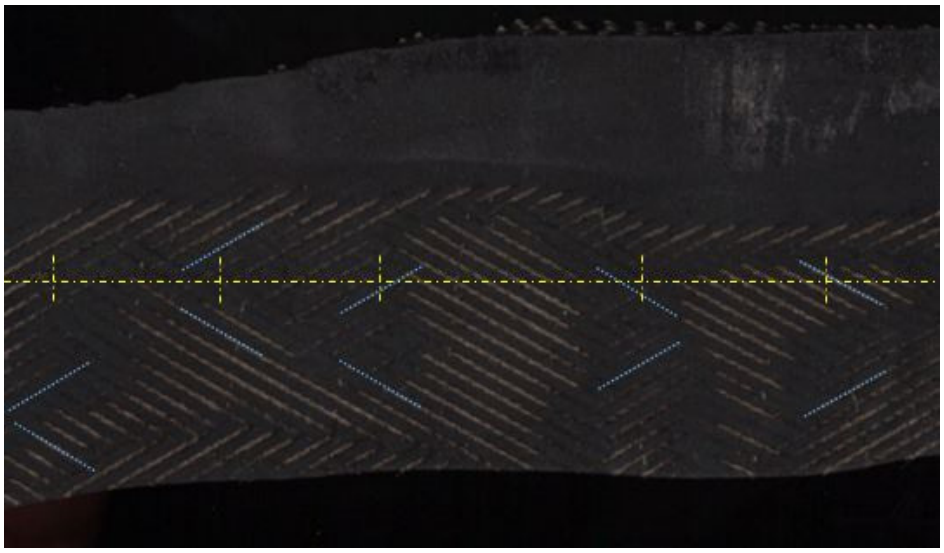

Figure 4-7: Detailed view of the cord layers and the measurement of the angles

In the first column of Table 4-5, the distance from the starting point as defined in Figure 4-3 in millimetres is listed. The next two columns are the measured angles (θ_1, θ_2) of the different cord layers, first the positive layer, then the negative layer.
The absolute angle (θ_x) of the two measured layers was calculated using the following formula (4.1):

$$\Theta_x = \frac{\Theta_1 + \Theta_2}{2} \tag{4.1}$$

Distance from inner Wire-Core [mm]	Angle of positive Cord Layer θ_1 [°]	Angle of negative Cord Layer θ_2 [°]	Absolute Cord Angle θ_x [°]
12	19	-13	16.0
45	21	-11	16.0
61	21	-13	17.0
126	22	-17	19.5
147	20	-17	18.5
167	24	-15	19.5
191	26	-21	23.5
204	28	-25	26.5
228	28	-29	28.5
247	31	-30	30.5
275	30	-30	30.0
292	30	-30	30.0
310	31	-31	31.0
358	32	-29	30.5
388	28	-30	29.0
407	30	-28	29.0
431	31	-25	28.0
452	30	-26	28.0

Table 4-5: Measured cord angles of air spring model A

The resulting data points were put into a plot diagram in MS Excel and an approximation was done to get a function where measurement inaccuracies were smoothened and eliminated.

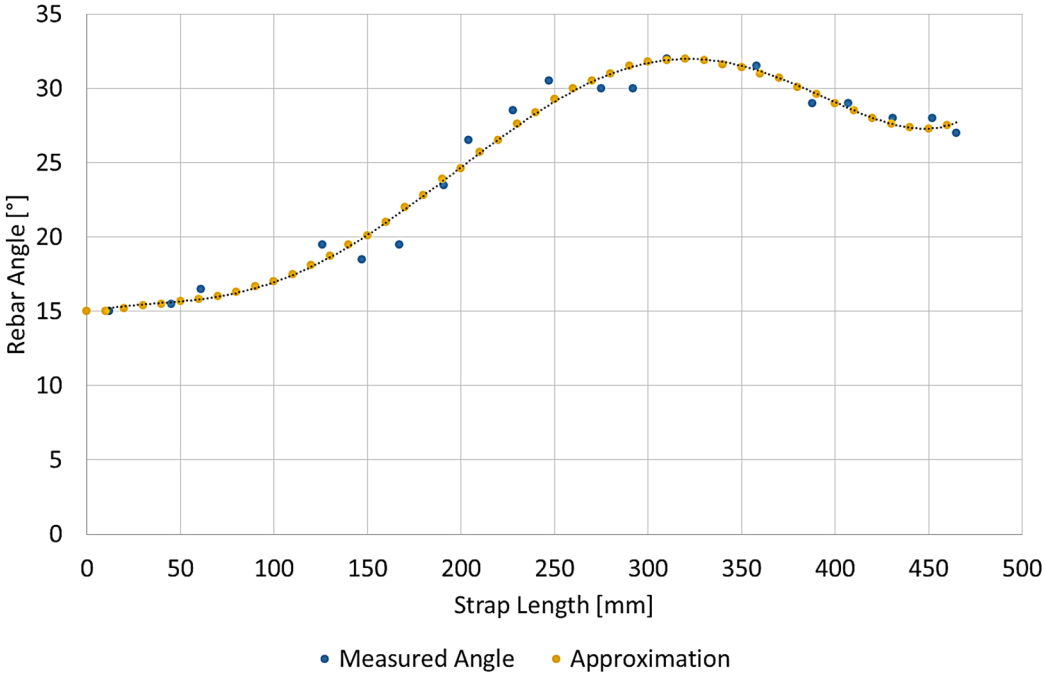

Table 4-6: Measured rebar angles along strap length

In Table 4-6, the approximation of the rebar angle is displayed. The whole process was done with all three air springs and the comparison of the different rebar angles is shown in Table 4-7.

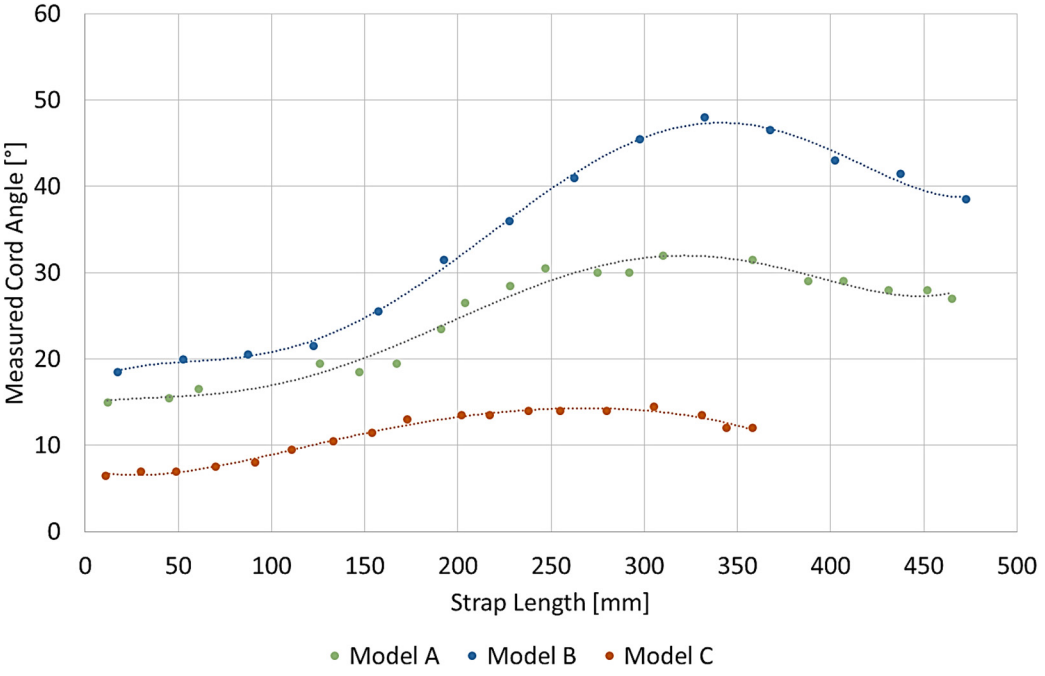

Table 4-7: Rebar angle of the different air springs

4.3.2.2 Material Model for the Cord

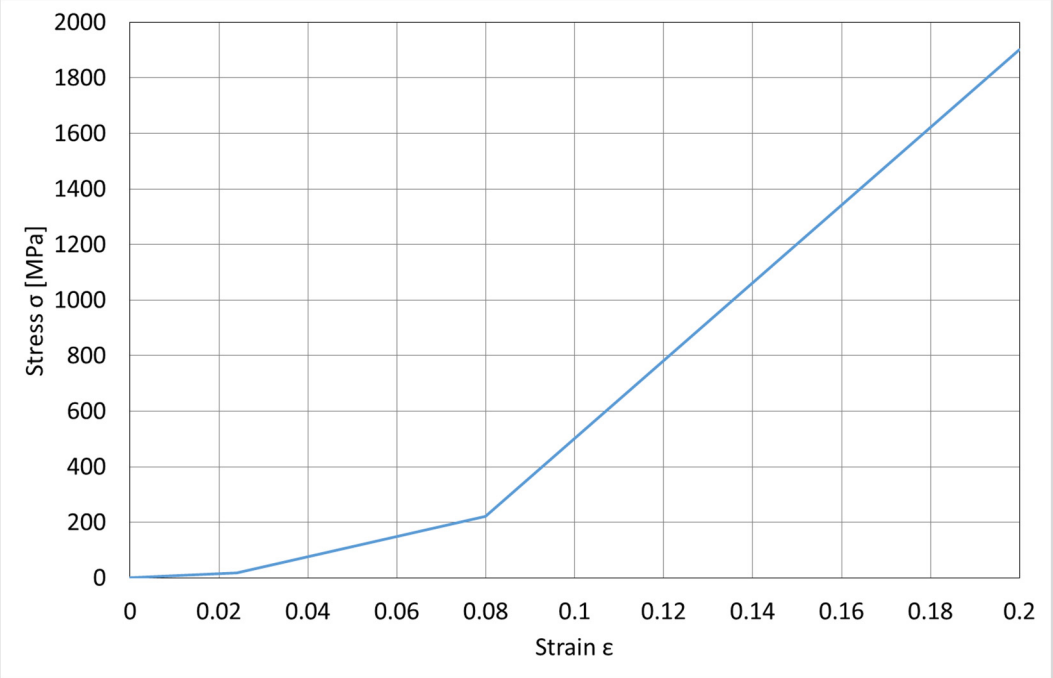

Table 4-8: Stress-strain diagram of the polyamide fiber[25]

Regarding the material properties, the model developed by Marco Talasz was used for all three air springs. The three sections, as shown in Table 4-8, each have a different modulus of elasticity.

Section	Strain [%]	Modulus of Elasticity [GPa]
Section 1	0,0 – 2.4	0.8
Section 2	2.4 – 8.0	3.6
Section 3	From 8.0	14.0

Table 4-9: Properties of the different sections of the polyamide fiber[26]

The model is thoroughly described in the prior thesis done by Marco Talasz, but to make it more readily understandable, a short summary of the three sections will be given:

[25] (Talasz, 2013, p. 60)
[26] (Talasz, 2013, p. 60)

Section 1:
The first section is influenced by the elongation of the entwined fibers. At first, the fibers are undeformed and have a specific length. When force is applied, which in our case happens during the inflation of the air spring, the entwined fibers elongate until they are tensed and up to that point, the fibers themselves do not elongate and thus, the modulus of elasticity is very low. The value of 0.8 was found by Marco Talasz through parameter variation.

Section 2:
In this section, different influences are important:

- Length differences of the fibers
- Differences between undeformed and deformed structure
- Differences of the position of the cord inside the elastomer during deformation

It is generally assumed that the length of the fibers in the elastomer matrix is not always the same. This means that at first only a few fibers have to stand up to all the forces until more fibers tense and can take loads as well.
There is a non-load part during the application of the forces – in this case the inflation of the air spring –which can be accredited to the deformation of the structure.
The position of the cord inside the elastomer matrix changes during the application of the forces. All three effects have some influence on the stiffness of the cord and are grouped together in section 2 of the material model. A value of 3.6 GPa was found by Marco Talasz through parameter variation.

Section 3:
This section depicts the elongation of the fiber itself. The value of 14 GPa for the modulus of elasticity was obtained by linearising the curve resulting from a tensile test on the fiber itself.[27]

The influence on the stiffness of the three different sections (Table 4-9) will be shown in chapter 8.1.2.

[27] (Talasz, 2013, pp. 61-65)

4.3.3 Steel Wire-Cores

The steel wire-cores, their diameters and positioning, give the air spring its basic form. The steel is the main carrier material and ensures the secure connection of the air spring to other parts of the suspension system. Compared to the other materials involved, the deformations in the steel wire-cores are negligible.[28]

A modulus of elasticity of 210 GPa and a Poisson's ratio of 0.3 will be used for all three models.

4.4 Manufacturing of the Air Spring

This chapter will only give a short summary of the whole manufacturing process of an air spring. The more detailed version of the process can be looked up in chapter 5 of Marco Talasz's Master Thesis.[29]Only some parts will be described in detail, since they are relevant for the cord angle of the final air spring and thus also relevant for the stiffness.

In the first part of the process, the elastomer is formed into rubber plates and rubber-cord-composite plates. These plates already have the desired cord angles. So, for example, if the cord angle of the air spring on the winding cylinder is requested to be 15°, the cord is already fused with the elastomer at an angle of 15°.[30]

The general overview of this part of the process is displayed in Figure 4-8:

[28] (Talasz, 2013, p. 18)
[29] (Talasz, 2013, p. 19)
[30] (Stumpf, 1997, pp. 60-71)

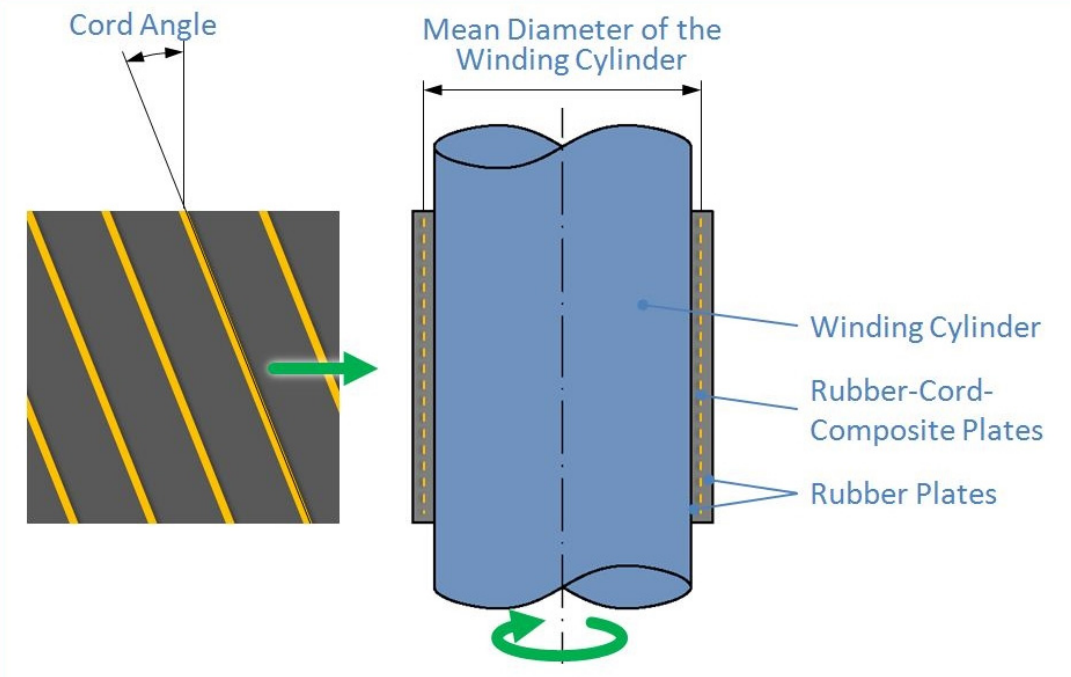

Figure 4-8 Plates on the winding cylinder[31]

The next step in the manufacturing process is the application of the inner steel wire-core. It is put into position while the air spring is still on the winding cylinder. Then the remaining part of the rubber is folded over the steel core and pressed onto itself to form a flap that holds the core.

The outer, larger, steel wire-core is put into position after the air spring is removed from the winding cylinder and the diameter of the loose end is widened to fit the outer steel core. Then a flap is formed as on the inner steel core. At the end of these steps, the so-called trumpet is ready for vulcanisation, as can be seen in Figure 4-9.[32]

[31] (Talasz, 2013, p. 23)
[32] (Talasz, 2013, p. 24)

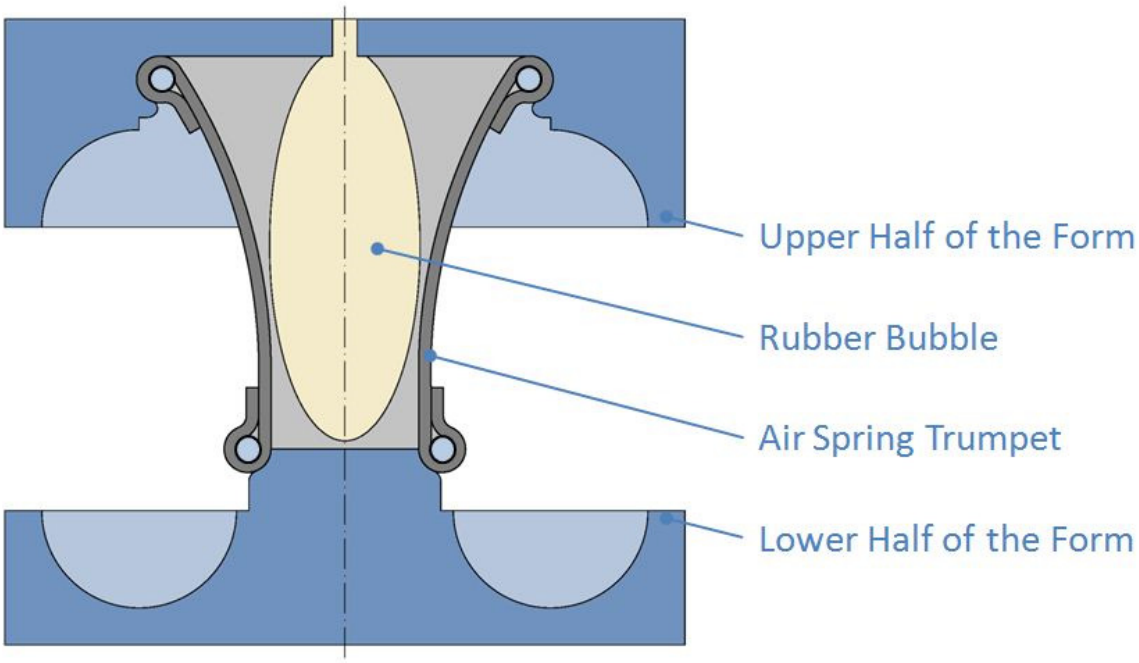

Figure 4-9: The air spring trumpet in the vulcanisation form[33]

For vulcanisation, the trumpet is put into the vulcanisation form, and then internal pressure is applied via a rubber bubble while the upper and the lower part of the vulcanisation form move towards each other.[34]

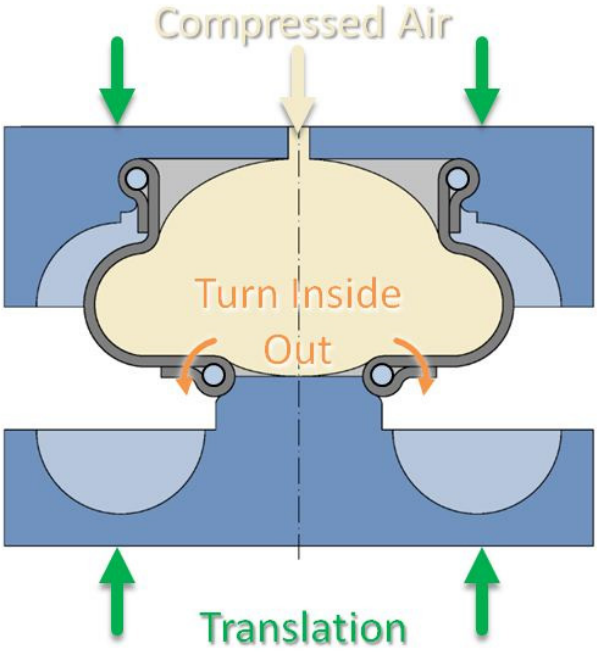

Figure 4-10: Closing of the vulcanisation form[35]

[33] (Talasz, 2013, p. 25)
[34] (Talasz, 2013, p. 25)

The result of this is that the lower part of the air spring trumpet turns inside out and achieves its final form. It is then vulcanised in the closed form for about an hour while the internal pressure remains constant.[36]

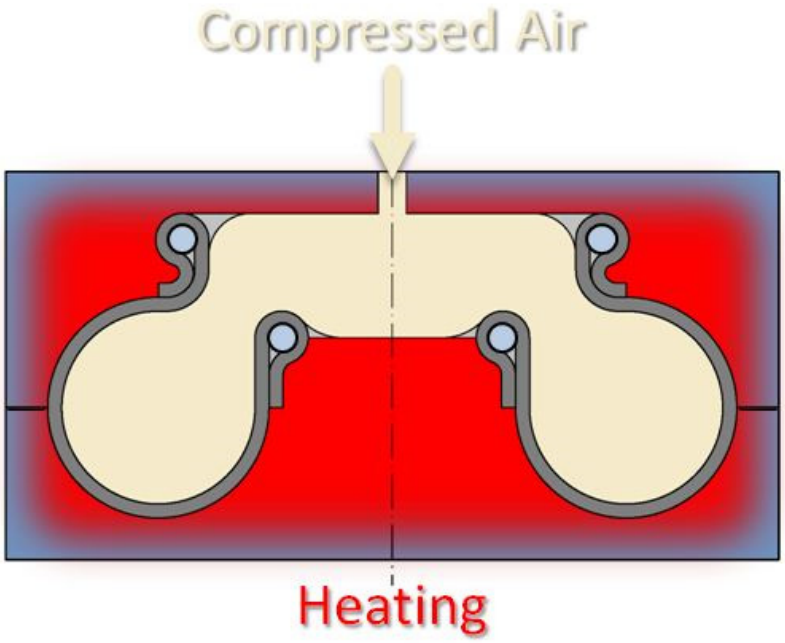

Figure 4-11: Vulcanisation of the air spring[37]

Important parts of the whole manufacturing process can be seen in Figure 4-8 to Figure 4-11.

[35] (Talasz, 2013, p. 26)
[36] (Talasz, 2013, p. 26)
[37] (Talasz, 2013, p. 26)

5 Summary of Previous Simulations

5.1 Model

The simulation model used by Marco Talasz will be described in this chapter. There will also be a description of the results he managed to get with this model and an outline of which problems were encountered.

The geometry was taken directly from the construction drawing used by GMT for the manufacturing. The drawing shows the air spring with an internal pressure of 1 bar. The contour was copied and imported into MSC Marc Mentat. Then the geometry was meshed with quad-elements. The result is shown in the picture below:

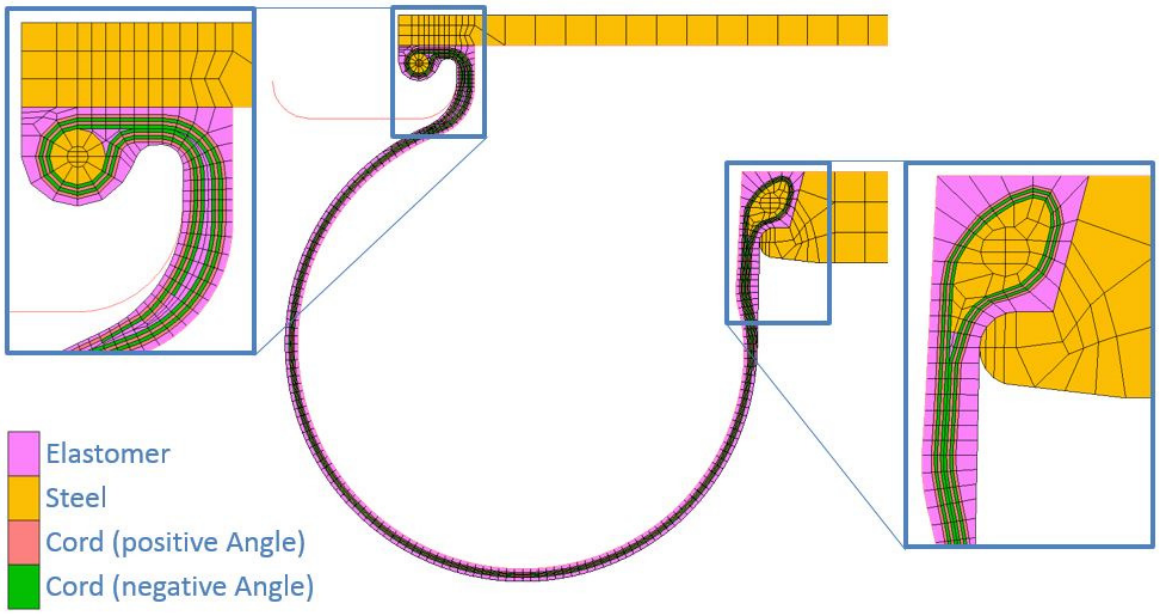

Figure 5-1: Model for prior simulations[38]

The model is very detailed and was used primarily for axisymmetric simulations to keep the duration of the simulation to a minimum. It was expanded to a full model, but because of the degree of detail, the duration of the simulations rose dramatically. For simulations where the model seen above (Figure 2-1) was not sufficient, a full model made of shell elements was developed. Its results were sufficient to meet the requirements of the paper and the simulation time got much shorter.

[38] (Talasz, 2013, p. 49)

A sectional view of this model can be seen in the following picture:

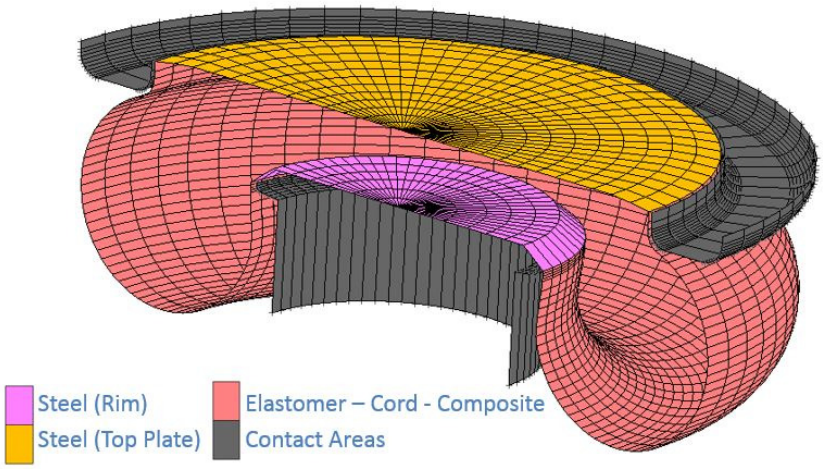

Figure 5-2: Shell model for simulations in lateral direction[39]

Both models were used for the first simulations of stiffness in this paper, but were found to be insufficient and had to be remodeled to better fit the needs. Details of the models used in this thesis are shown in chapter 6.

5.2 Results

The main focus of Marco Talasz's thesis was the development of a simulation model as well as of sufficient material properties. The following tables show the results achieved during his work (Table 5-1 to Table 5-4). For the first three simulations, the axisymmetric model shown in Figure 5-1 was used. Only the results of Table 5-4 had to be calculated with the three-dimensional model. The simulation results are all inside the scatter band of the measurements except for the first part of the lateral translation-lateral force diagram. The superposition angle near the lower foldover is the cause of this deviation.

[39] (Talasz, 2013, p. 51)

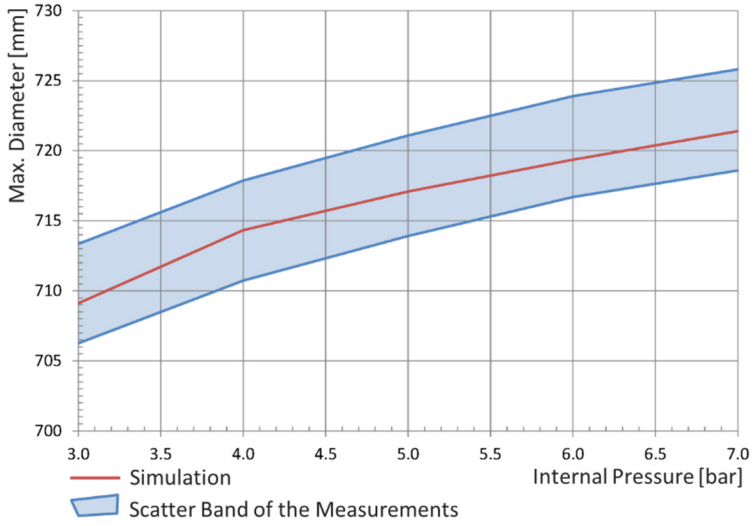

Table 5-1: Diameter-pressure curve of the air spring[40]

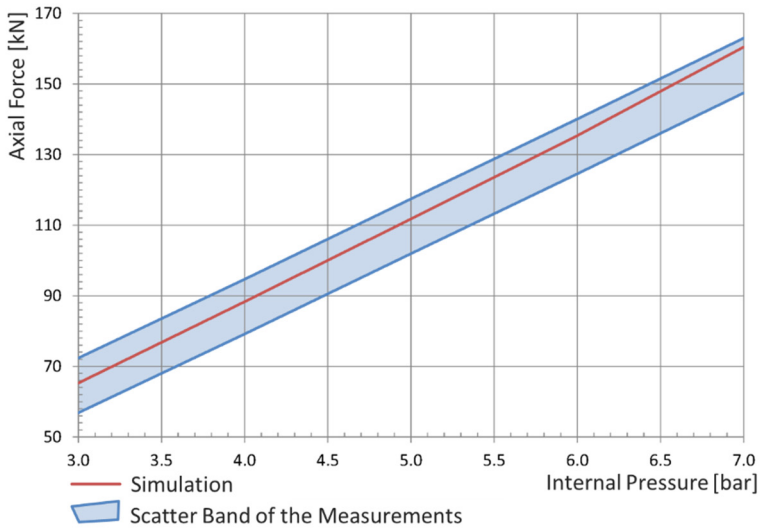

Table 5-2: Axial force-pressure curve of the air spring[41]

[40] (Talasz, 2013, p. 73)
[41] (Talasz, 2013, p. 74)

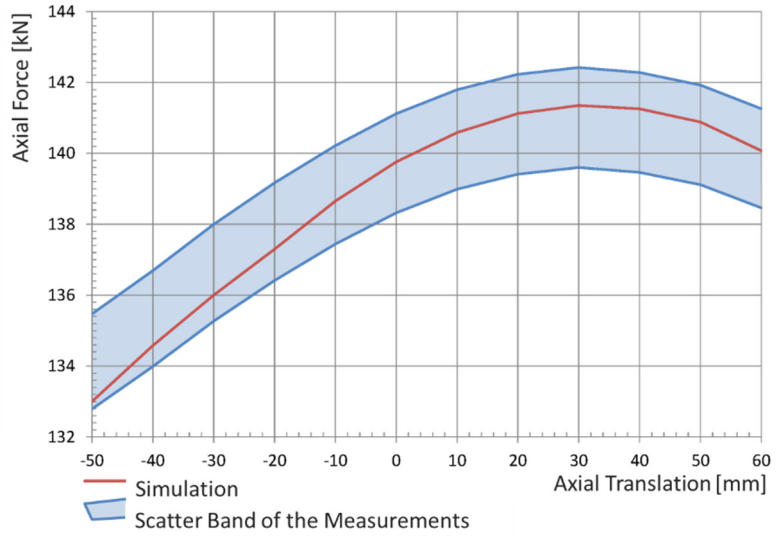

Table 5-3: Axial translation-axial force curve of the air spring[42]

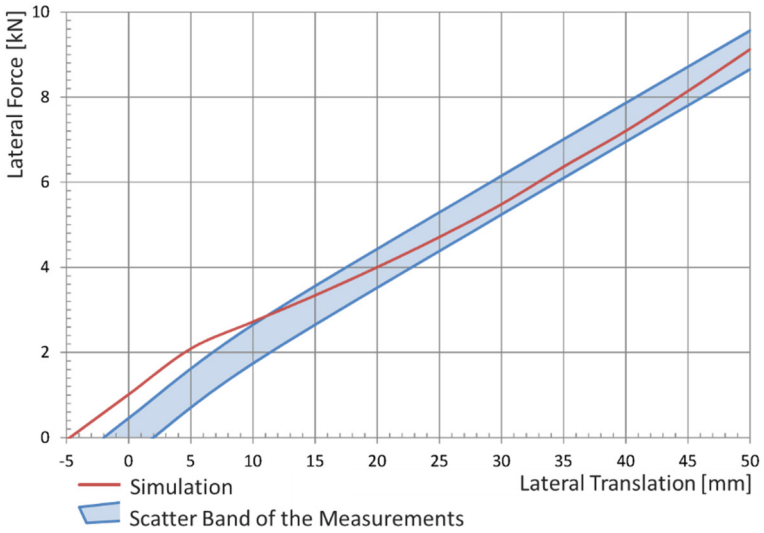

Table 5-4: Lateral translation-lateral force curve of the air spring[43]

[42] (Talasz, 2013, p. 76)
[43] (Talasz, 2013, p. 75)

6 Simulation Model

6.1 Stiffness Simulations with Prior Model

The first step was to use the simulation models described in chapter 5.1. At this point, a few problems were encountered:

a. Due to the immense number of elements and the complexity of the simulation, the simulation times for the lateral and the torsional stiffness were unacceptably long.
b. Maximum principal stress of the rebar layer could not be displayed correctly.
c. The simulated lateral and torsional stiffness results were far below the results derived from measurements.

6.1.1 Evaluation Method

Since it was reasonable to assume that the rebar angles might also be off because the display of their stress values was incorrect, this problem was addressed first. There was also strong reason to believe that this might heavily influence the results of the stiffness simulations and might lead to a breakthrough for point c.
After trying many different approaches, the reason behind the wrongly displayed rebar angles was found. The so called RBEs, which function as rigid links between the primary node and all the attached secondary nodes and which were used to move the upper plate as well as evaluate the results, were unusable together with rebar elements.
The solution to this problem was a rigid body consisting of a curve attached to the upper edge of the upper plate in combination with the curve depicting the clamping ring. Together, they form one rigid body which can move the upper plate in every direction as well as rotate it and can be used to evaluate the resulting forces. The rigid body can be either load-controlled or position-controlled. Load-controlled means that it does the same as a single node which is chosen as the primary node, and position-controlled means that the rigid body itself gets instructions on how to move.
Unfortunately, tests with this new evaluation method revealed that the results stayed the same.

In the new version of MSC Marc Mentat (v2014.0), this display error has already been solved.

6.2 Model with Contour Calculation

To achieve better results for the stiffness of the air spring, it was assumed that a new model had to be developed. The first part of every model is its geometry. In previous models, the geometry was copied from the construction drawing; then it was meshed and used. The problem with this procedure is that the construction drawing shows the air spring with an internal pressure of 1bar. This means, that the contour is already different from the contour of the air spring without internal pressure. Since the original contour has an influence on the rebar angle, which in turn has an influence on the stiffness, in the development process of the new model it was assumed that it is very important to get the real contour of the air spring without internal pressure.

This chapter deals with the development of the new contour from scratch. All the pictures and data show air spring model A. Models for air spring B and C were built analogously.

6.2.1 Contour Calculation

For the calculation of the contour without internal pressure, the rebar angle values are needed. How to arrive at those angles was described in chapter 4.3.2.1.
According to Hans Pahl, the contour of an air spring can be calculated by using the following formula:

$$\Theta_x = \arcsin[\frac{L_x}{L_0} * \sin(\Theta_0) * (1 - \varepsilon)] \qquad (6.1)^{44}$$

Pahl calls this a simplified substitute model to calculate the changed cord angle of an air spring. L_0 is the original length and L_x is the deformed length of the air spring part which is taken into consideration. The same principle applies to Θ_x as the deformed cord angle and Θ_0 as the original angle. When Pahl is talking about the original length or the original angle, he means the angle or length of the air spring while still in production and still on the winding drum.

A similar approach was taken by Marco Talasz, who simplified this formula by using the assumption that the cord will not expand and only changes its angle in the composite, as seen in Figure 6-1. This is also the reason why the original contour has a big influence on the angles of the rebar in the final air spring.

[44] (Pahl, 2002, p. 31)

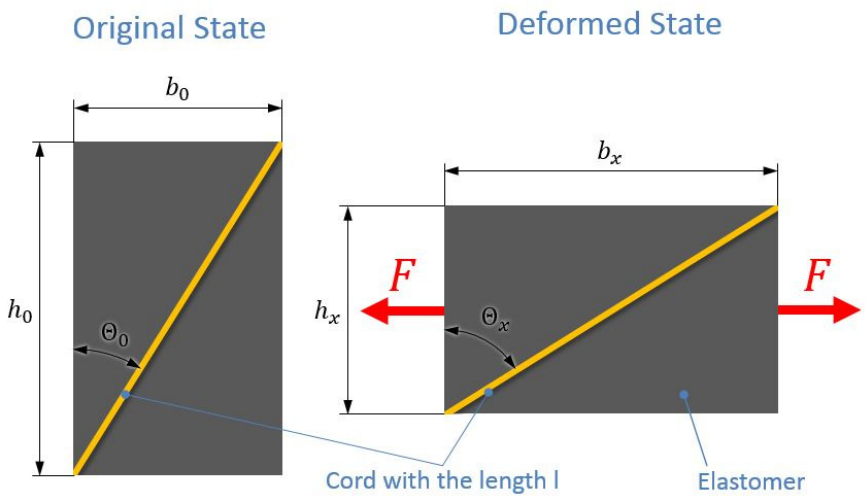

Figure 6-1: Change of cord angle during deformation[45]

In the figure, h_0 is the original height and h_x is the deformed height of whichever air spring part is under consideration at that stage. The same principle applies to b_0 and b_x as well as to Θ_x as the deformed cord angle and Θ_0 as the original angle.

$$\sin \Theta_0 = \frac{b_0}{l} \qquad (6.2)[46]$$

$$\sin \Theta_x = \frac{b_x}{l} \qquad (6.3)[46]$$

$$\Theta_x = \arcsin[\frac{b_x}{b_0} * \sin \Theta_0] \qquad (6.4)[46]$$

$$\frac{b_x}{b_0} = \frac{d_x}{d_0} \qquad (6.5)[46]$$

$$\Theta_x = \arcsin[\frac{d_x}{d_0} * \sin \Theta_0] \qquad (6.6)[46]$$

In this model, the cord angle is calculated with the sine-function. Since the length of the cord is assumed to remain the same during the deformation, the formula (6.2) can be inserted into the formula (6.3) to arrive at the following conclusion (6.4). The breadth of the original and the deformed state have the same ratio as the original diameter to the deformed diameter of the air spring, as can be seen in (6.5). Using this formula, the final conclusion is reached in formula (6.6).[47]

[45] (Talasz, 2013, p. 43)
[46] (Talasz, 2013, p. 44)
[47] (Talasz, 2013, p. 43)

The formula (6.6) in combination with the measured angles shown in chapter 4.3.2.1 was used to calculate the contour of the air spring without internal pressure. The calculations were done in MS Excel and the schematic contour is shown in the figure below (Figure 6-2).

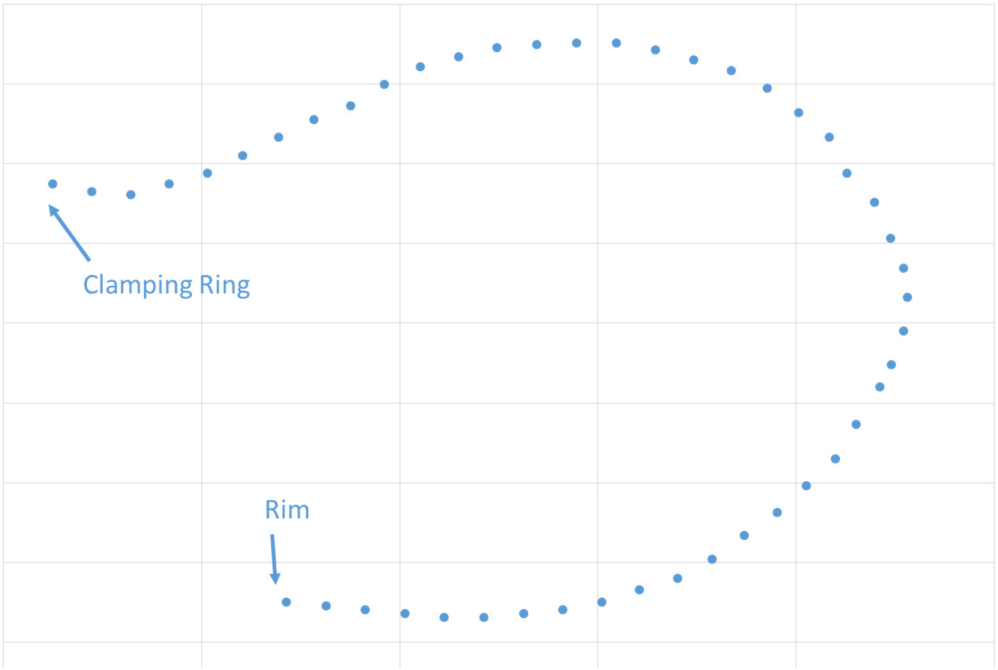

Figure 6-2: Schematic model derived from the contour calculation

For easier use in MSC Marc Mentat, the contour was then modified in MS Excel to include the width of the elements. This just meant that on either side of the data points, another point at a distance of 3 mm was added. This final contour was then imported into MSC Marc Mentat and meshed. Since the calculated contour does not give any indication as to how long the foldover might be, the upper and lower foldover had to be modeled manually. The length was measured at the air spring strips, which were cut out of the whole bellows to get the rebar angles along the strap length. The final meshed model is depicted in Figure 6-3.

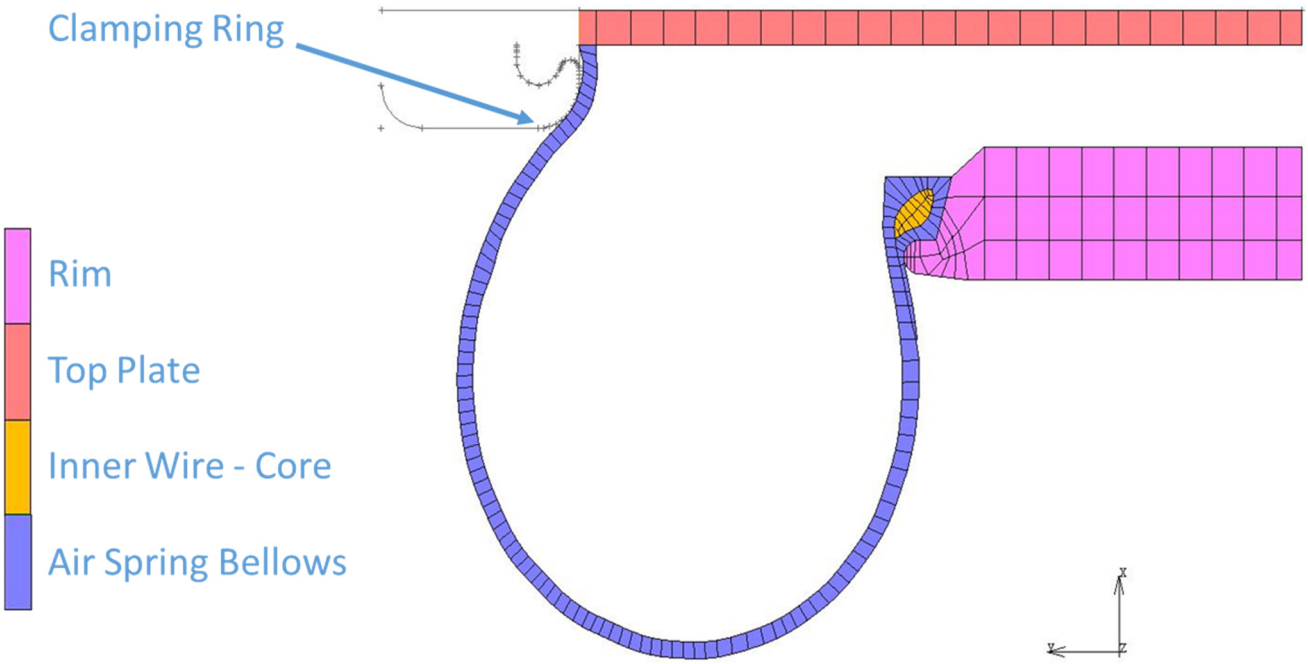

Figure 6-3: Model with contour calculation

Even though, overall, the rebar angles yielded by the evaluation of data from this simulation model matched the ones measured on the air springs itself well, some tests with this new model revealed that the results still showed similar deviation with regard to stiffness as the older models. Thus the new main task for this thesis was finding the main influences on the stiffness of the air spring.

6.3 Final Simulation Model

A new model was developed based on the knowledge gained from the contour calculation as well as the prior models. This model will now be described in detail.

6.3.1 Geometry

6.3.1.1 Contour

Since the rebar angles from the contour calculation model in chapter 6.2 matched the measured rebar angles well, that contour was used as the basic geometry for the final model. Only the areas near the upper and lower foldover had to be adapted to resemble the real air springs more closely. For those parts, the contour was taken from the construction drawings. Also, the area around the clamping ring was cut off for the main simulation model to simplify the model and make the calculations more

stable. In chapter 8.2.6, this area will be fully modeled and differences in the results will be shown.

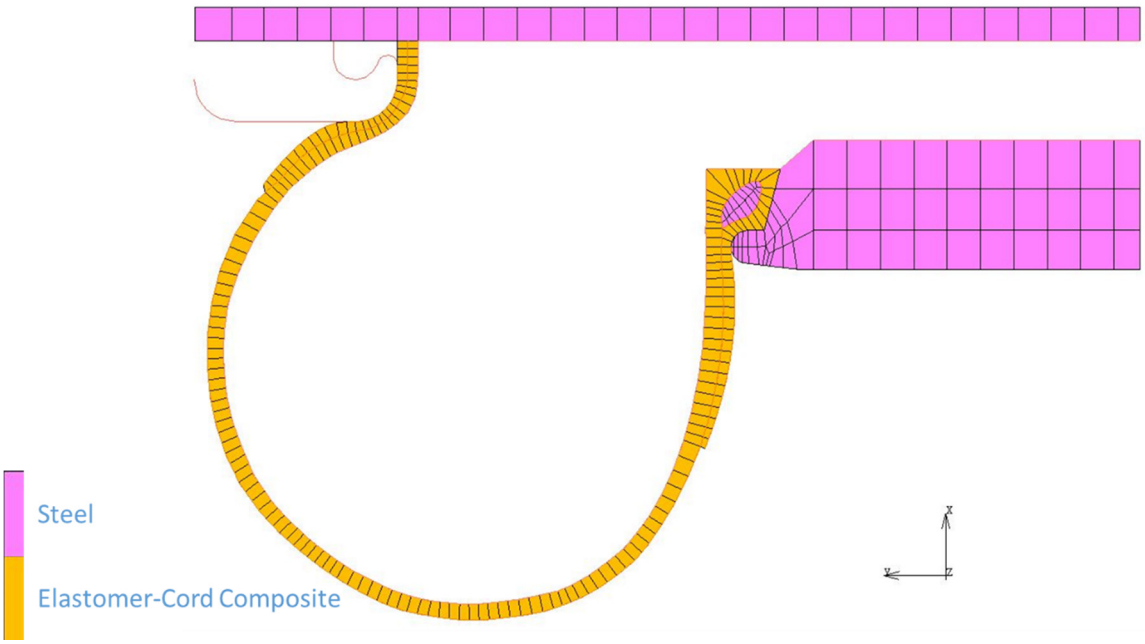

Figure 6-4: Model for air spring A

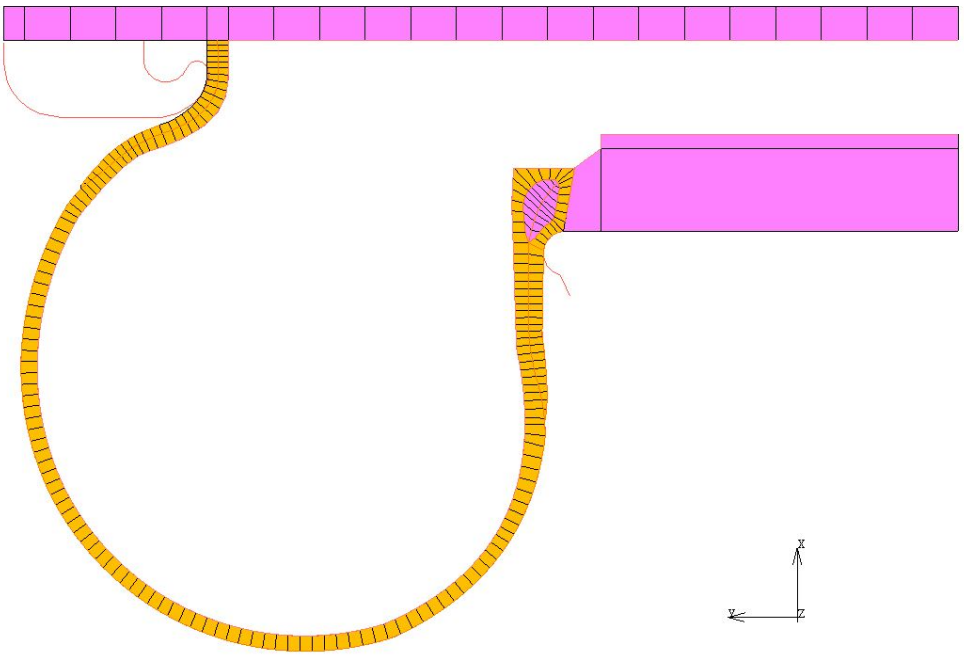

Figure 6-5: Model for air spring B

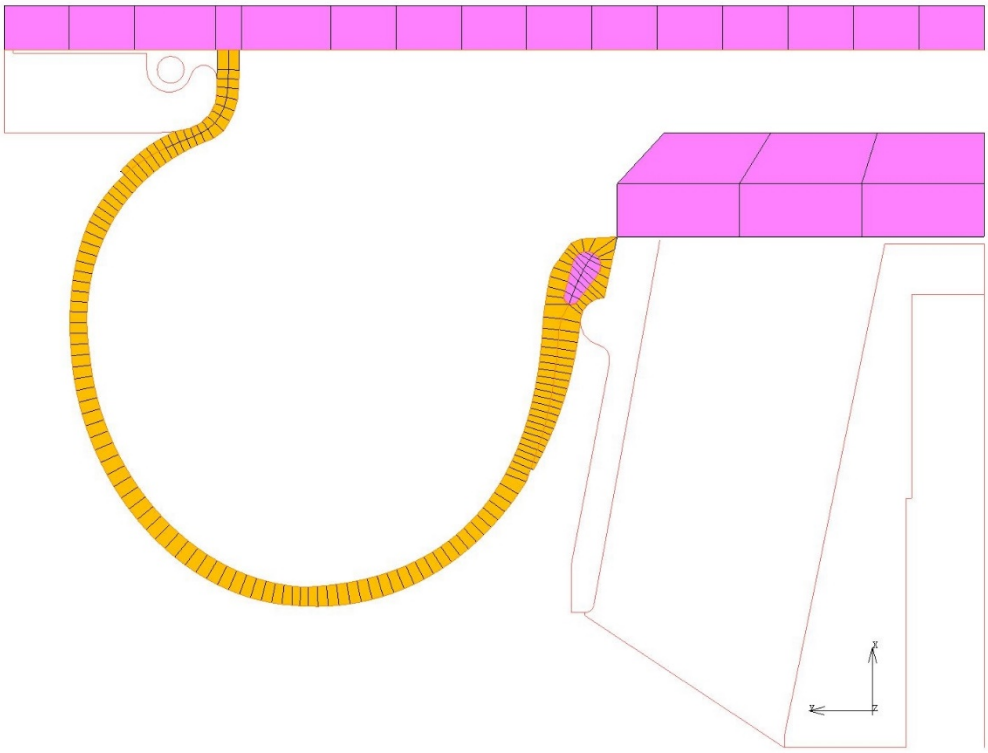

Figure 6-6: Model for air spring C

The comparison of the rebar angles yielded from the results of the simulation models and the angles of the cord from the measurements can be seen in the following table (Table 6-1):

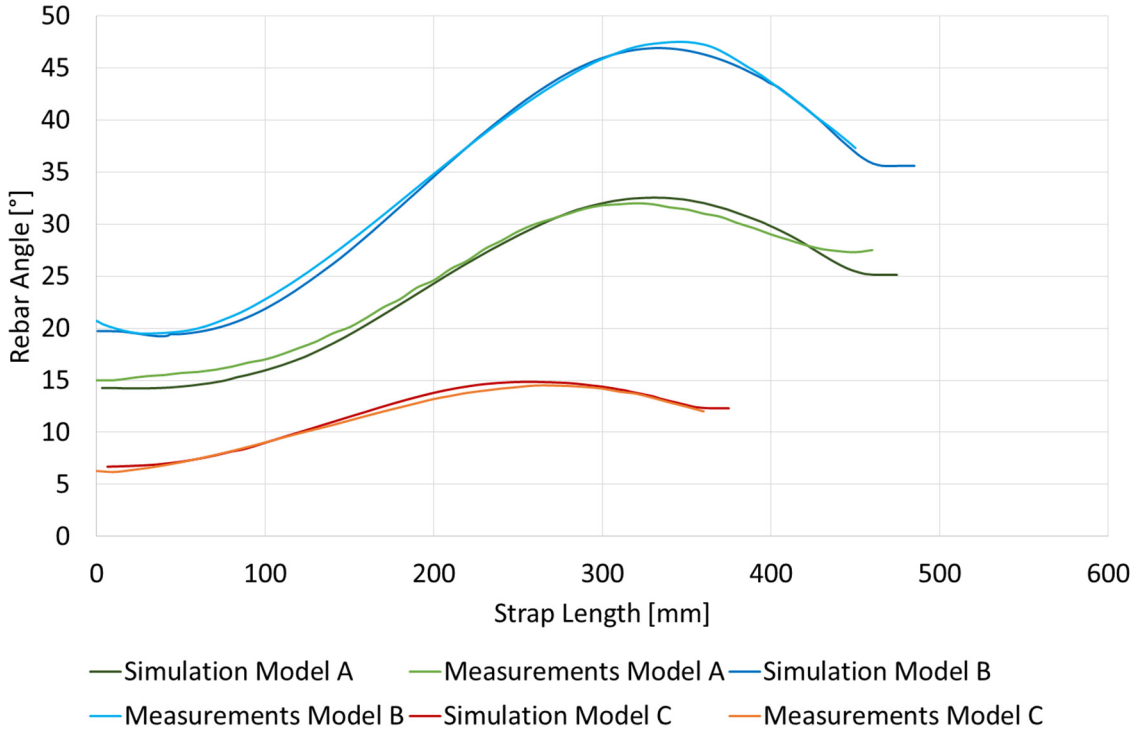

Table 6-1: Comparison of measured and simulated rebar angles

6.3.2 Simulation Parameters

6.3.2.1 Element Types

Two element types were used for the simulation model:

Element Type 10:
The element type 10 is an isoparametric arbitrary quadrilateral element with four nodes per element. It is written specifically for axisymmetric simulations. The use of other elements like higher-order elements with for example 8 nodes per element was considered, but was dismissed due to the superiority of the element type 10 in a contact analysis. Since the whole evaluation of the forces is done with a rigid contact body, the contact analysis has to be very accurate.
Element type 10 was used for all steel parts as well as the elastomer parts of the air spring.[48]

Element Type 144:
The element type 144 was used for the cord inlays of the air spring. Elements of this type are isoparametric rebar elements written for axisymmetric simulations and are used with four node host elements such as elements of the type 10. The number and

[48] (MSC Software Corporation, 2012, p. 144)

position of the rebar layers as well as the rebar angle, number of inlays per length unit, surface area of one cord and the diameter of the winding cylinder are parameters for the exact definition of the used materials. The element uses the same four nodes as the host element.[49] This means that first the contour has to be meshed, and then all the air spring elements have to be duplicated and copied onto the original elements. These elements "lie" on top of each other. Then the nodes of both element layers have to be merged to gain double elements with one part rebar and one part elastomer but only 4 nodes per element pair.

6.3.2.2 Element Size

The element size of the final simulation model was radically increased compared to the prior models (Figure 5-1).
The element size affects the simulation in different ways. The simulation runs faster and is more stable due to the smaller number of elements, but the results also change. For example the stiffness generally decreases with increasing number of elements. This has to be taken into account when comparing the models from prior works to models in this paper. A more detailed model will be shown in chapter 8.2.7.

6.3.3 Material Properties

6.3.3.1 Elastomer

For the elastomer material model, the stress strain diagram shown in chapter 4.3.1 (Table 4-3) was used to calculate mooney parameters for the yeoh-model. The yeoh-model was chosen because the calculated curve greatly matched the measurement data for strains up to 300% and the fitting of this specific model can be done if only the measurement data of the tensile strength test is available because it is a function of only one invariant. The calculated curve was modeled with the experimental fit option implemented in MSC Marc Mentat. The alignment of the experimental fit and the original measurement data can be seen in the following table (Table 6-2):

[49] (MSC Software Corporation, 2012)

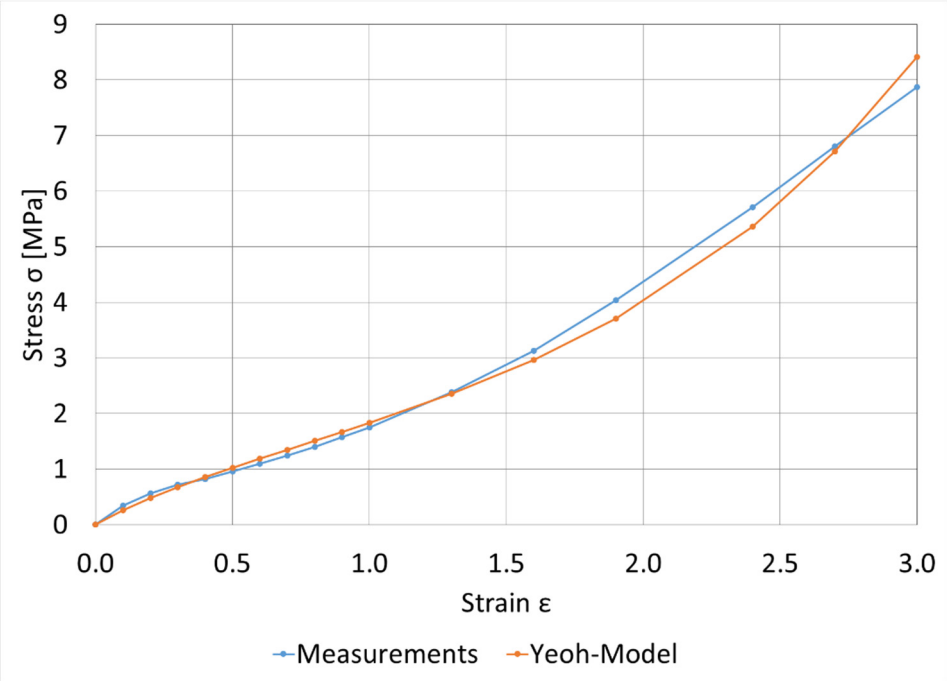

Table 6-2: Experimental fit of mooney parameters for the yeoh-model

As described in chapter 4.3.1, the same material model was used for all three air springs. The influence of the material is shown in chapter 8.1.1.

6.3.3.2 Cord

A variation of the material model shown in chapter 4.3.2.2 was used for the cord in all three models. This value of the third section of the model was calculated for a cord with a cross-sectional area of 0.08 mm^2. The diameter of the entwined cord filaments in the three air spring models in this paper was measured with a caliper rule and averaged at about 0.56 mm for all three models. The rebar area was then calculated as 0.2463 mm^2. A value of 0.25 mm^2 will be used as the rebar area for all three air springs. When using this value for the calculation of the modulus of elasticity, the value 3.6 GPa instead of 14 GPa for the third section is gained. This number was used in the material model. The number of cord fibers per length unit as well as the original angles of the cord were used as shown in Table 4-4.
The influences on the stiffness of the different sections of the material model will be shown in chapter 8.1.2.

6.3.3.3 Steel

As described in chapter 4.3.3, a modulus of elasticity of 210 GPa and a Poisson's ratio of 0.3 will be used for all three models.

6.3.4 Contact Control

In MSC Marc, there are two different models for the contact control. On the following pages, the advantages and disadvantages of the different methods will be explained and an example will be given.

6.3.4.1 Node-to-Segment Contact:

This contact algorithm works with nodes being in contact with a segment (= element edge, curve, surface...). It is the contact algorithm which has been used for many years and has thus become established in the industry.

Still, there are some problems with this algorithm:

- The node-to-segment algorithm has problems with maintaining stress continuity across the contact interface of deformable bodies. This happens because the non-penetration constraint is enforced on a nodal basis.[50]

- To get valuable results, the multi-point constraint equations must be optimised since the solution depends on the selection of the master and the slave nodes. In other words, the solution depends on which nodes are touching and which nodes are being touched. Optimisation of these constraint equations is generally achievable, but in some models, there can be problems.[50]

- There can also be problems with double-sided shell contact.[50] For example, if a shell element is touched on the top by an element and on the bottom by another element, there will be an error, because the node-to-segment contact cannot handle this situation for shell elements.[51]

- Main problems also include jumps when slave nodes slide off the master surface. This means, that the contact status between two elements changes from "in contact" to "no contact" and vice versa and thus changes the results for the worse.[52]

6.3.4.2 Segment-to-Segment Contact

Since 2010, Marc Mentat has been using a new contact algorithm called segment-to-segment, which addresses the problems pointed out above. Contact detection for segment-to-segment method is more refined than the node-to-segment method. Here, every element gets a predefined number of auxiliary points, which are only used during the contact detection phase. Contact detection works in two stages:[53]

- Distance Check: First the program checks if one of the auxiliary points is inside the distance tolerance.
- Direction Check: The next step is to check, if the angle between the normal vector at the auxiliary point and the normal vector of the contacted segment is larger than the threshold value α. Default value of α is 120°.

Only if both checks satisfy positive results, the segments are defined as being in contact.[54] An overview is shown in Figure 6-7:

[50] (MSC Software Corporation, Marc 2012 - Volume A: Theory and User Information, 2012, p. 584)
[51] (Shetty, 2013, p. 6)
[52] (Puso & Laursen, 2003, p. 3)
[53] (Shetty, 2013, p. 7)
[54] (Shetty, 2013, p. 8)

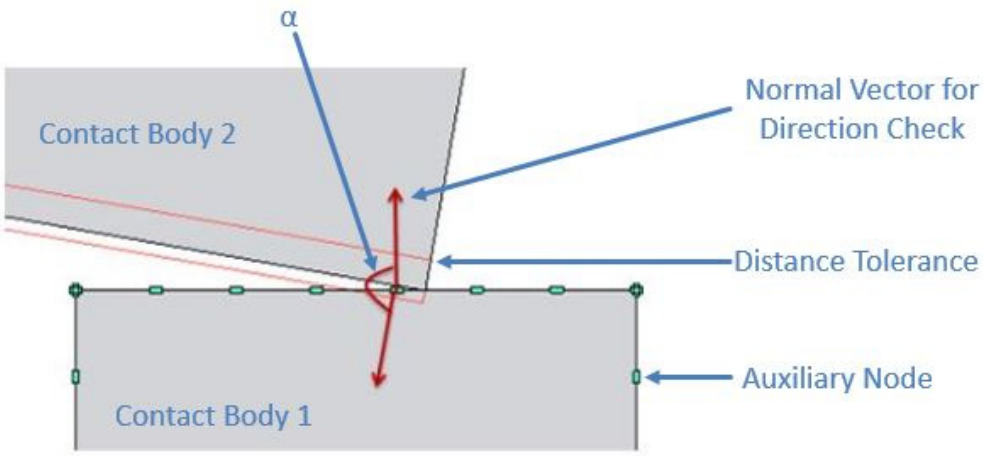

Figure 6-7: Segment-to-segment contact detection[55]

Since the segment-to-segment contact approach has not matured as much as the node-to-segment contact, there are still a few limitations:

- Only mechanical contact is supported. Thermal or coupled contact cannot be calculated with this contact model.
- The auto increment load stepping algorithm is not supported.

In the simulations for this thesis, both of those limitations can be neglected.

The following example will make this theory more understandable and show the differences between the two contact algorithms. It is also described in the MSC Marc Mentat – User's Guide. Figure 2-1 shows an overview of the system before any forces are applied.

[55] (Shetty, 2013, p. 8)

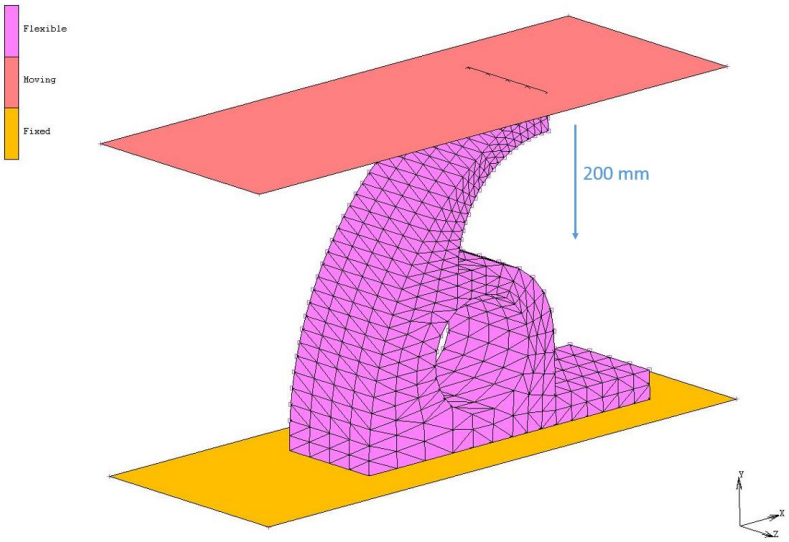

Figure 6-8: Segment-to-segment example: Overview[56]

Parameters:

- Material for flexible body: Neo-Hookean material model (Mooney, C_{10}=100)
- Upper rigid body is moved 200 mm downwards in –Y direction
- Lower rigid body is fixed at its position[57]

During application of the forces, the flexible body will be deformed and compressed. To compare the differences between the two contact models, the same simulation was performed twice with the only difference being the contact algorithm. The results are shown in Figure 6-9 and Figure 6-10. The yellow parts indicate contact between outer element edges, and blue means no contact.

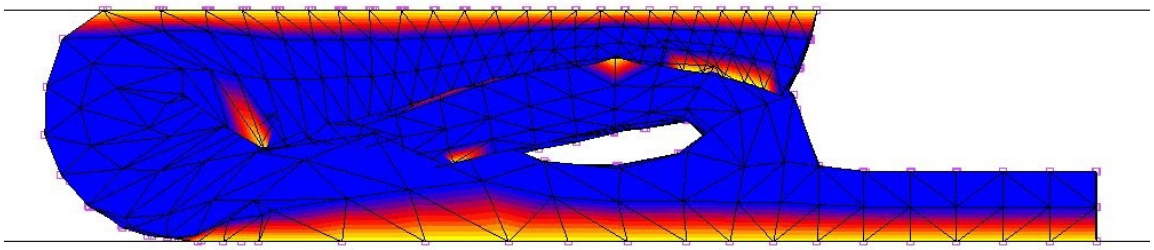

Figure 6-9: Segment-to-segment example: Result of node-to-segment contact

In Figure 6-9, some nodes can be seen that penetrate the edges of the elements on the opposite side of the contact and only a few nodes in contact are shown.

[56] (Own Picture)
[57] (MSC Software Corporation, Marc 2012 - User's Guide, 2012, p. 728)

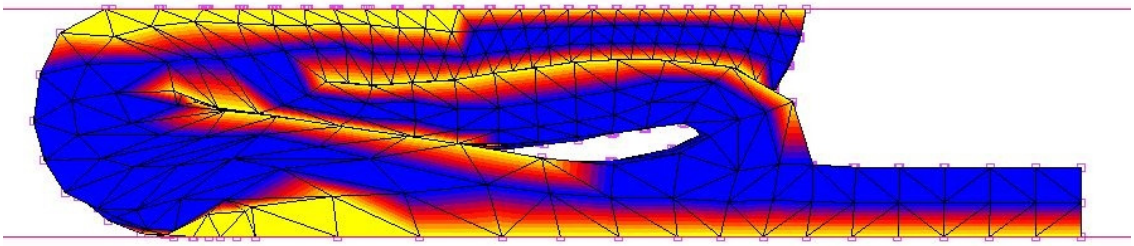

Figure 6-10: Segment-to-segment example: Result of segment-to-segment contact

In the second picture (Figure 6-10), the results of the simulation using the segment-to-segment contact are shown. Compared to the result of the node-to-segment simulation (Figure 6-9), there is clearly a more defined contact band. Also, no penetrations occur and the performance is better.

A similar test was done with the developed model of the air spring to see how the contact control influences the stability of the results. In the example, the air spring is fully modeled and the main focus lies on the clamping ring, because the contact in this area is the most complicated. In both simulations, the same parameters were used except for the contact control.

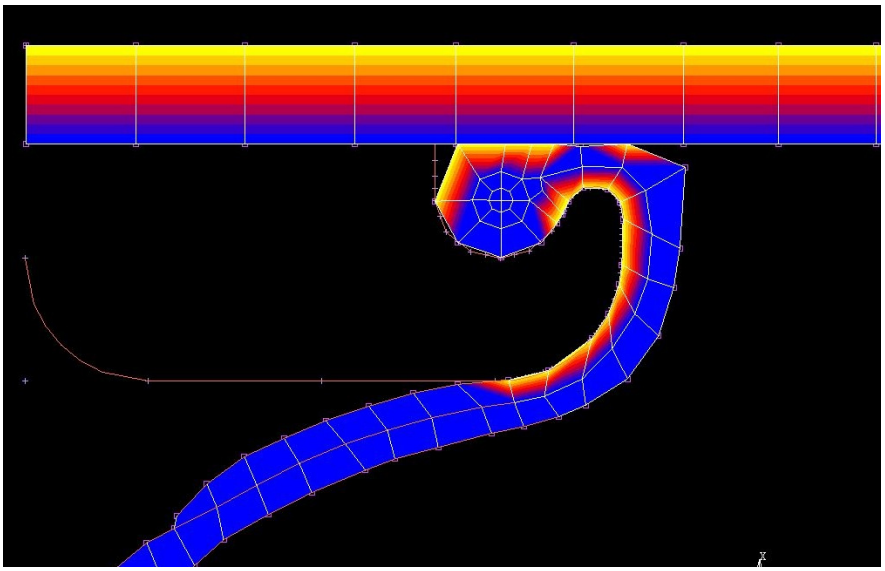

Figure 6-11: Clamping ring detail using node-to-segment contact

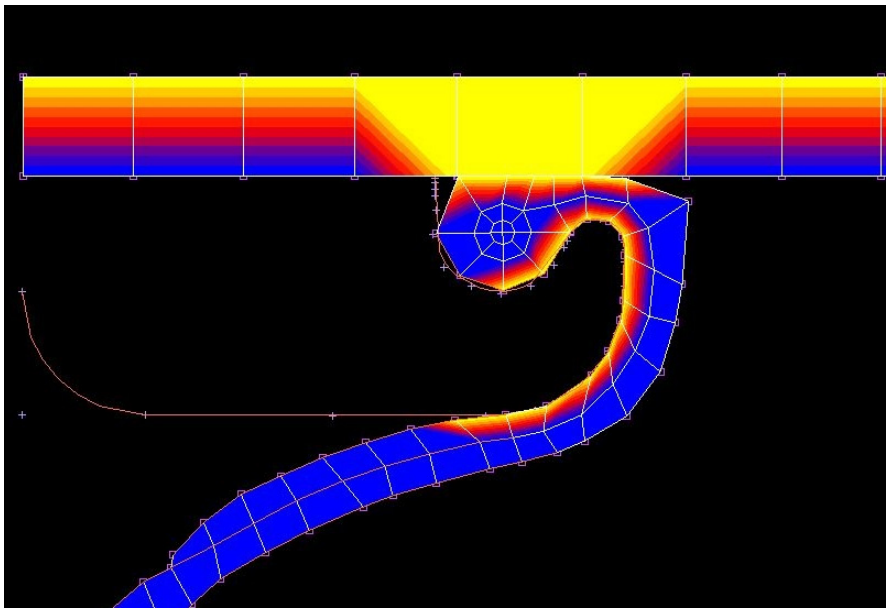

Figure 6-12: Clamping ring detail using segment-to-segment contact

Both pictures show the air spring at the operating pressure of 7 bar. The contact between the upper plate and the air spring elements is the main focus of the pictures. The contact band in the second picture (Figure 6-12) clearly displays a smoother contact, compared to the node-to-segment contact of the first picture (Figure 6-11). The resulting curves of the lateral stiffness display the same trend: The segment-to-segment contact smoothes the results and makes the whole simulation more stable.

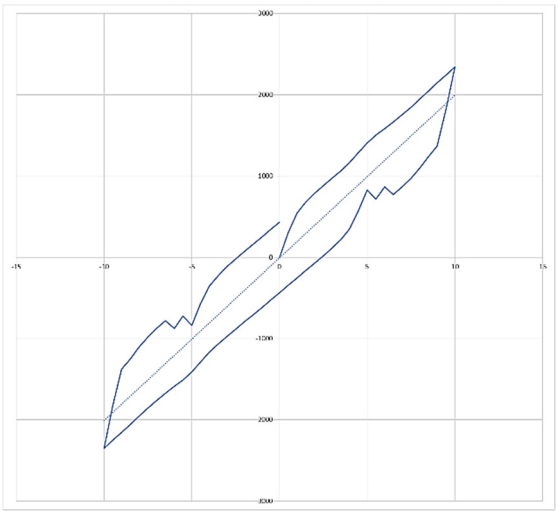

Table 6-3: Results of node-to-segment contact

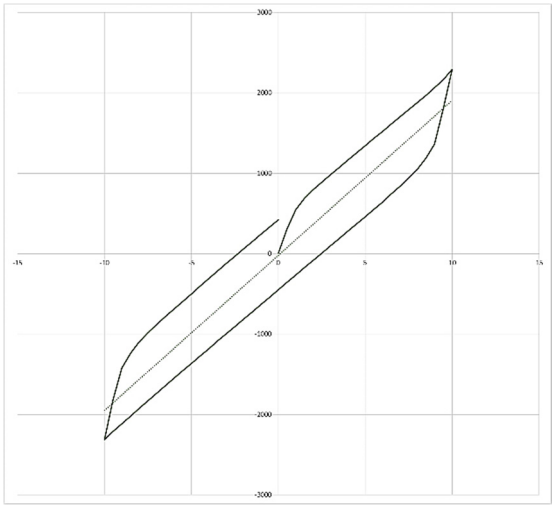

Table 6-4: Results of segment-to-segment contact

7 Comparison between Measurement Data and Simulation Results

In this chapter, the three models will be compared to the available measurement data to show the deviations and limitations of the simulation models.

7.1 Testing Procedure

First, the testing procedure of air spring stiffness has to be explained. For testing, the air spring is mounted on the testing machine and the rim is fixed in a specific position. Then it is filled with pressurised air until it is at working pressure and the upper plate is lowered by the testing machine to get to the operating height of the air spring. The operating height is defined as the height between the lower edge of the upper plate and the lower edge of the bulge of the air spring bellows as shown in the following depiction (Figure 7-1). At this point, the inflation is stopped and the whole air spring is sealed off to ensure isochoric behaviour for the whole testing process.

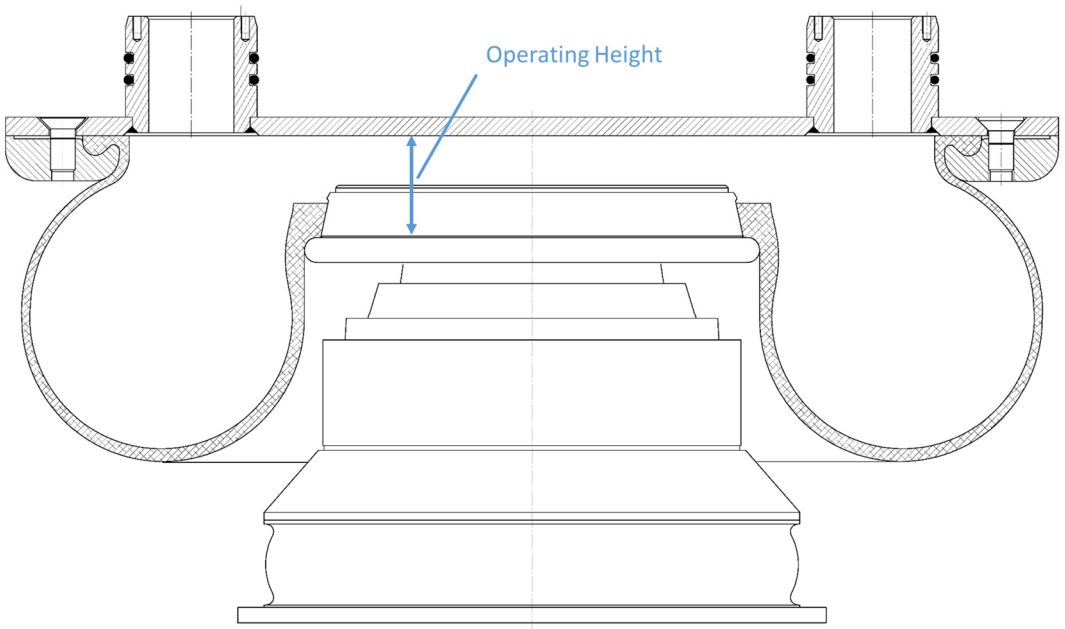

Figure 7-1: Definition of operating height of an air spring[58]

At this point, the air spring is ready for testing:

[58] (GMT GmbH, Primär- und Sekundärfederung - Schienenfahrzeuge, 2010, p. 20)

- For the axial stiffness, the upper plate moves 10 mm in positive and 10 mm in negative vertical direction.
- For the lateral stiffness, the upper plate moves 10 mm in positive and negative horizontal direction.
- For torsional stiffness, the upper plate is rotated by 0.5° around its own axis in positive and negative direction.

7.2 Results of the Simulation

The simulation is done exactly the same as during the real testing process. The elements of the rim are totally restrained, which means that they cannot move or rotate in any direction. The upper plate is held at operating height and the air spring is inflated until it reaches working pressure. Then, the closed cavity function is used to simulate the sealed air spring and to ensure isochoric behaviour. Finally, the upper plate is moved in the demanded direction and the reaction forces on the upper plate and the clamping ring in relation to the translations are evaluated. This results in a hysteresis around the starting point by either a translation of 10 mm in X- or Y-direction for axial and lateral stiffness or 0.5° rotation for the torsional stiffness. The evaluated data points are then imported into excel to produce the diagrams seen below (Table 7-1 to Table 7-3). The curve is then linearised to get the values depicted in the diagrams, which are then used for the evaluation of the results.

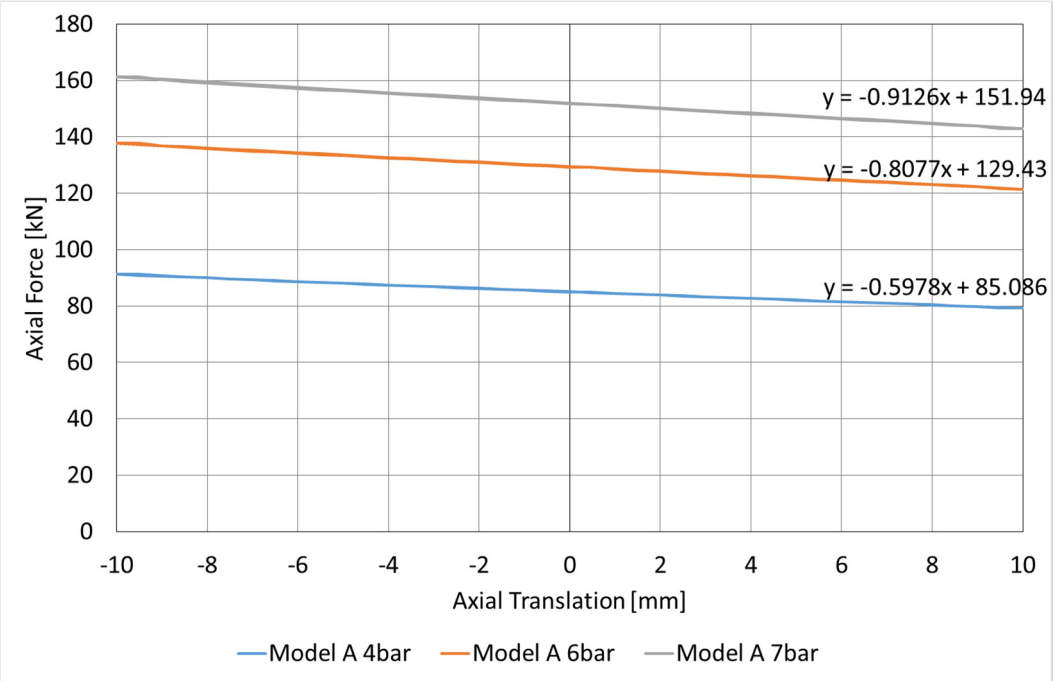

Table 7-1: Simulation of axial stiffness at different pressure levels: Model A

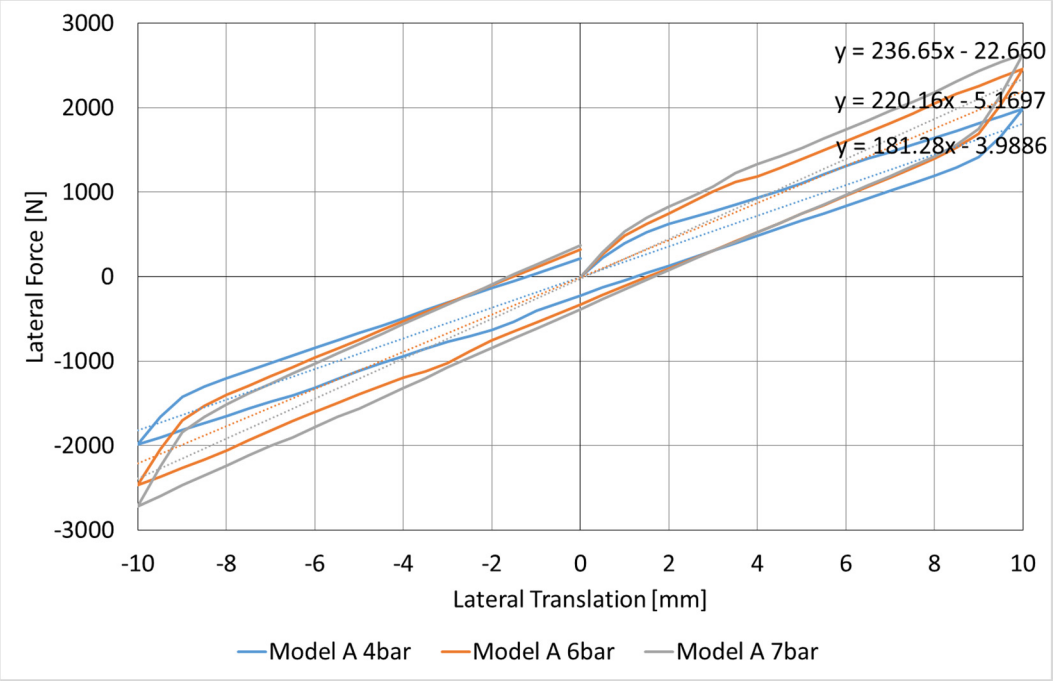

Table 7-2: Simulation of lateral stiffness at different pressure levels: Model A

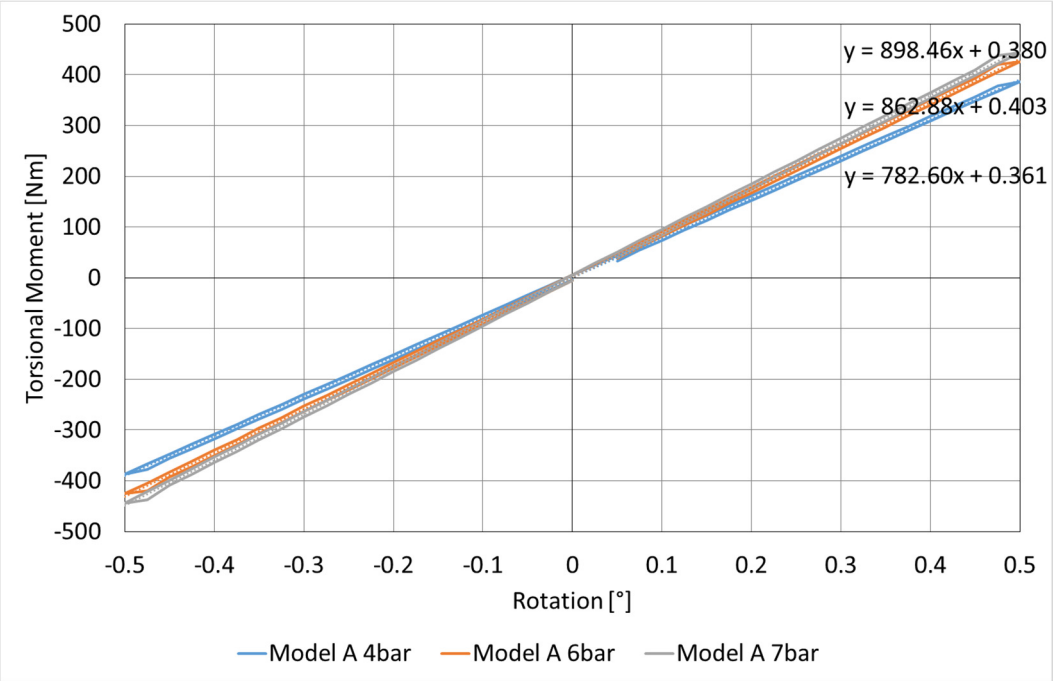

Table 7-3: Simulation of torsional stiffness at different pressure levels: Model A

The three tables above (Table 7-1 to Table 7-3) show the simulation results of air spring model A at different working pressure levels of 4, 6 and 7 bar. The results for air spring Model B and Model C show similar curves and can be found in the appendix. In the tables below, the comparison of the measurement data and the simulation results is shown and the deviation is calculated.

Model A		Axial Force [kN]	Deviation [%]	Axial Stiffness [N/mm]	Deviation [%]	Lateral Stiffness [N/mm]	Deviation [%]	Torsional Stiffness [Nm/°]	Deviation [%]
Measurement	7 bar	156.4		946.5		234.4		1159.6	
Simulation	7 bar	151.9	2.9	912.6	3.6	236.7	1.0	898.5	22.5
Measurement	6 bar	132.1		840.4		216.8		864.6	
Simulation	6 bar	129.4	2.0	807.7	3.9	220.2	1.5	862.9	0.2
Measurement	4 bar	86.0		630.3		195.7		808.4	
Simulation	4 bar	85.1	1.0	597.8	5.2	181.3	7.3	782.6	3.2

Table 7-4: Comparison of measurements and simulation: Model A

Model B		Axial Force [kN]	Deviation [%]	Axial Stiffness [N/mm]	Deviation [%]	Lateral Stiffness [N/mm]	Deviation [%]	Torsional Stiffness [Nm/°]	Deviation [%]
Measurement	7 bar	142.1		664.3		220.0		1016.7	
Simulation	7 bar	137.1	3.5	647.4	2.5	230.3	4.7	968.7	4.7
Measurement	6 bar	120.4		595.2		208.4		936.0	
Simulation	6 bar	116.7	3.1	576.1	3.2	217.4	4.3	920.2	1.7
Measurement	4 bar	77.9		450.3		185.4		754.3	
Simulation	4 bar	76.7	1.5	432.8	3.9	185.2	0.1	844.9	12.0

Table 7-5: Comparison of measurements and simulation: Model B

Model C		Axial Force [kN]	Deviation [%]	Axial Stiffness [N/mm]	Deviation [%]	Lateral Stiffness [N/mm]	Deviation [%]	Torsional Stiffness [Nm/°]	Deviation [%]
Measurement	6 bar	112.0		937.0		221.0		-	
Simulation	6 bar	110.4	1.4	939.2	0.2	216.4	2.1	487.6	
Measurement	5.58 bar	103.0		871.0		215.0		-	
Simulation	5.58 bar	102.5	0.5	893.2	2.5	208.9	2.9	475.5	
Measurement	4.7 bar	86.0		775.4		194.0		-	
Simulation	4.7 bar	85.7	0.3	768.0	1.0	192.4	0.8	442.1	

Table 7-6: Comparison of measurements and simulation: Model C

The results of all three models show good correlation in axial and lateral stiffness. The maximum value of deviation in these categories is 7 %. The limitations of the simulation can be seen when it comes to the torsional stiffness: Here, the different pressure levels cannot be reproduced accurately and deviation goes up to 22.5 %. For Model C, no torsional stiffness measurement data is available.

8 Definition of Main Influences on Stiffness

In this chapter, the influences on the stiffness of the air springs will be defined, simulated and then the results will be categorised by their influence on the stiffness.

8.1 Material parameters

First, the material parameters of the different components of the air spring will be discussed and the way to incorporate them in the simulation will be described.

8.1.1 Elastomer

To test the elastomer's influence on the stiffness of the air spring, the material parameters for simulation had to be simplified to make it easier to change them without having to do a new experimental fit for the parameters each time. The simplest Mooney-model is the NeoHook–model. In contrast to the 3-parametric Yeoh–model, it only uses the shear modulus for the description of the model. The shear modulus G equals 2 times the value C_{10}, which is used for the NeoHook-model description. According to literature, the NeoHook-model gives good correlation with experimental data up to 40 % strain[59] and is sufficiently accurate even up to 70 % strain.[60] The maximum value of total strain was analysed using Marc Mentat and the highest value reached was 0.38.

$$\varepsilon = \frac{\Delta L}{L_0} \tag{8.1}$$

$$d\varepsilon' = \frac{dL}{L} \tag{8.2}$$

$$\varepsilon' = \ln(\frac{L}{L_0}) \tag{8.3}$$

$$\varepsilon' = \ln(1 + \varepsilon) \tag{8.4}$$

ε' represents the true strain and ε the nominal engineering strain.

[59] (MSC Marc Mentat, 2011, p. 185)
[60] (Technische Universität Berlin, p. 43)

Using the formula above (8.4), a value of 0.46 for the nominal engineering strain was reached. This number is within the sufficiently accurate area of the NeoHook-model. Since the NeoHook-model can be easily varied due to its only parameter being the shear modulus, this model was used to test the influence of the elastomer on the stiffness of the air spring.

The value of the NeoHook-parameter C_{10} was calculated using the experimental fit option in MSC Marc Mentat. The following table (Table 8-1) shows the comparison of the measurement data, the Yeoh-model and the NeoHook-model up to a strain of 3. The NeoHook is similar to the Yeoh-model up to a strain of about 1, then it deviates strongly from the measurements.

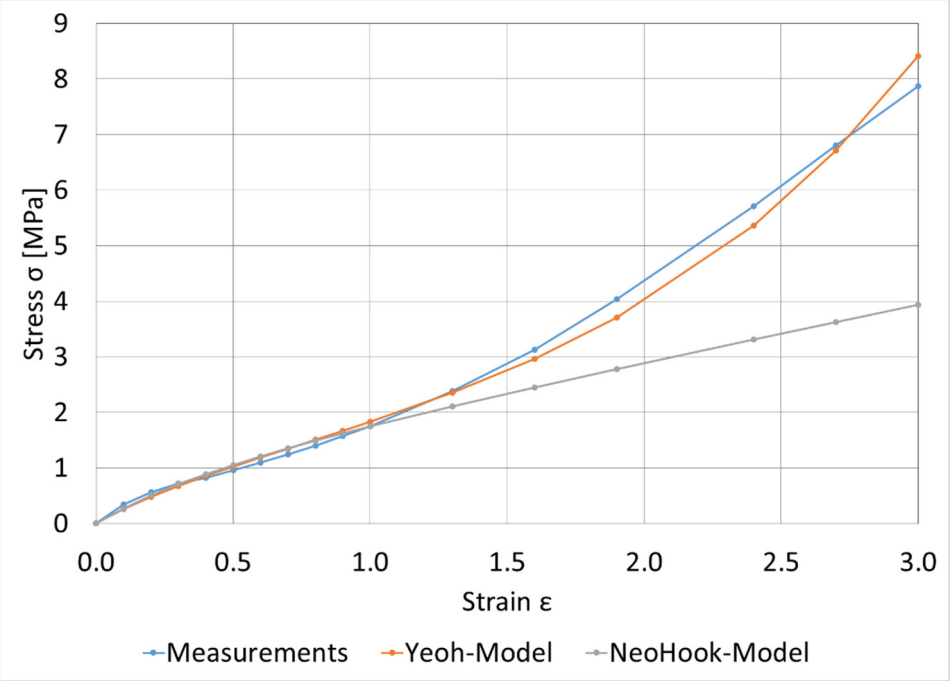

Table 8-1: Comparison of yeoh and neohook-model

Since the elements in the model have a maximum strain of 0.46, only this area is of interest. The detailed view of this area can be seen in the following table (Table 8-2). The correlation between the two models is clearly very good and the deviation from the measurement data is very small. This shows that the neohook-model can be used for the testing of the influence of the elastomer on the air spring stiffness.

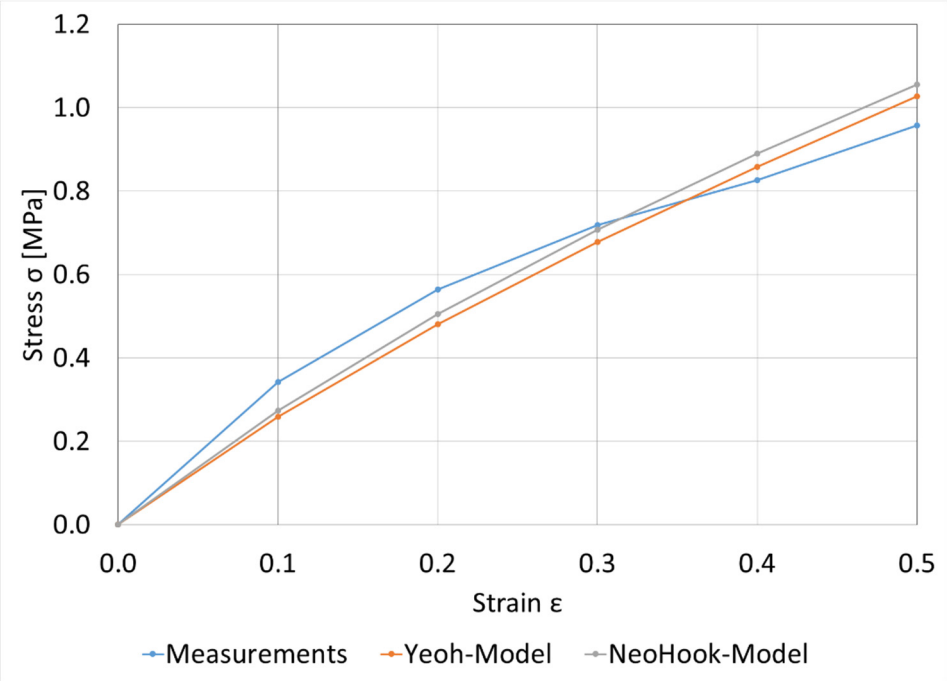

Table 8-2: Comparison of yeoh and neohook-model: Detailed view

For the simulation of the influence of the elastomer material model, the NeoHook-parameter C_{10} which was used varied from 60 % up to 140 % of its calculated value. The results can be seen in the tables below:

Model A	%	Axial Force [kN]	Axial Stiffness [N/mm]	%	Lateral Stiffness [N/mm]	%	Torsional Stiffness [Nm/°]	%
Mooney Model - NeoHook	60	152.8	907.9	99.2	221.6	93.1	863.1	94.5
	80	152.2	911.6	99.6	232.6	97.7	895.0	98.0
	100	151.7	915.4	100.0	238.1	100.0	913.4	100.0
	120	151.2	921.0	100.6	243.2	102.2	936.3	102.5
	140	150.8	927.3	101.3	253.4	106.5	954.7	104.5

Table 8-3: Simulation results for varying elastomer material stiffness: Model A

Model B	%	Axial Force [kN]	Axial Stiffness [N/mm]	%	Lateral Stiffness [N/mm]	%	Torsional Stiffness [Nm/°]	%
Mooney Model - NeoHook	60	137.5	634.3	97.4	222.4	93.4	939.5	96.7
	80	137.2	644.4	99.0	231.8	97.4	971.2	99.9
	100	136.9	651.2	100.0	238.0	100.0	971.7	100.0
	120	136.7	658.2	101.1	243.5	102.3	993.9	102.3
	140	136.6	666.4	102.3	249.8	105.0	1014.9	104.4

Table 8-4: Simulation results for varying elastomer material stiffness: Model B

Model C	%	Axial Force [kN]	Axial Stiffness [N/mm]	%	Lateral Stiffness [N/mm]	%	Torsional Stiffness [Nm/°]	%
Mooney Model - NeoHook	60	111.4	921.1	98.4	201.9	90.9	467.0	94.5
	80	110.7	929.8	99.3	213.4	96.1	471.1	95.3
	100	110.0	936.5	100.0	222.1	100.0	494.2	100.0
	120	109.5	941.5	100.5	231.8	104.4	505.2	102.2
	140	108.9	945.6	101.0	240.9	108.5	516.1	104.4

Table 8-5: Simulation results for varying elastomer material stiffness: Model C

The influence of the elastomer material on the axial stiffness is clearly negligible, since a variation of 80 % (60 % to 140 %) only resulted in a deviation of 2 to 4 %. For the lateral as well as the torsional stiffness, the influence is more pronounced. The 80 % variation leads to a maximum of 18 % deviation for the lateral and 8 % for the torsional stiffness for the air spring model C. The two models A and B, which are very similar to each other, show less deviation at a maximum of 12 % for the lateral stiffness. These factors corroborate the assumption put forward in chapter 4.3.1: A small change in the elastomer material will not have a great influence on the air spring stiffness.

8.1.2 Cord

Since the input parameters of the cord material (polyamide 6.6) were generated empirically for a specific simulation model, the different sections of the 3-part model have to be tested to determine the significance of each individual section.

8.1.2.1 Section 1

8.1.2.1.1 Length of Section 1

The first parameter that was tested was the length of the first section of the material model. The length was tested from 80 % to 120 % of its original length. A graphic representation of this variation is shown in the table below (Table 8-6).

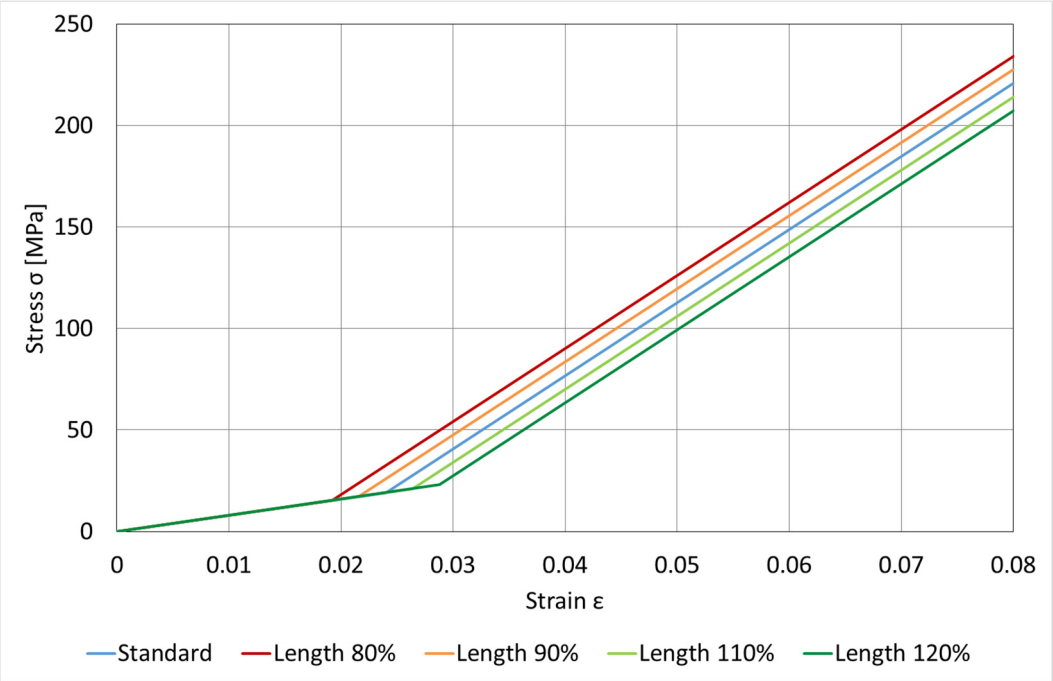

Table 8-6: Variation of cord material section 1: Length

The material model is only shown up to a strain of 0.08 because section 3 does not have an influence on the simulations. A further explanation is given in chapter 8.1.2.3.

Model A	%	Axial Force [kN]	Axial Stiffness [N/mm]	%	Lateral Stiffness [N/mm]	%	Torsional Stiffness [Nm/°]	%
Cord Model Section 1 - Length	80	151.5	916.8	100.5	239.9	101.4	912.9	101.6
	90	151.7	914.7	100.2	238.5	100.8	902.8	100.5
	100	151.9	912.6	100.0	236.7	100.0	898.6	100.0
	110	152.2	911.7	99.9	234.4	99.0	895.6	99.7
	120	152.4	910.6	99.8	232.9	98.4	892.9	99.4

Table 8-7: Simulation results for varying length of section 1 of the cord: Model A

Model B	%	Axial Force [kN]	Axial Stiffness [N/mm]	%	Lateral Stiffness [N/mm]	%	Torsional Stiffness [Nm/°]	%
Cord Model Section 1 - Length	80	136.6	649.5	100.3	233.9	101.6	991.1	102.3
	90	136.8	648.6	100.2	232.2	100.8	986.9	101.9
	100	137.1	647.4	100.0	230.3	100.0	968.7	100.0
	110	137.3	645.8	99.8	228.0	99.0	946.2	97.7
	120	137.6	644.5	99.6	226.0	98.1	934.2	96.4

Table 8-8: Simulation results for varying length of section 1 of the cord: Model B

Model C	%	Axial Force [kN]	Axial Stiffness [N/mm]	%	Lateral Stiffness [N/mm]	%	Torsional Stiffness [Nm/°]	%
Cord Model Section 1 - Length	80	110.2	937.7	99.8	218.6	101.0	489.3	100.4
	90	110.3	938.5	99.9	218.6	101.0	488.0	100.1
	100	110.4	939.2	100.0	216.4	100.0	487.6	100.0
	110	110.5	939.5	100.0	215.3	99.5	487.0	99.9
	120	110.7	938.2	99.9	214.2	99.0	484.5	99.4

Table 8-9: Simulation results for varying length of section 1 of the cord: Model C

According to the results shown above (Table 8-7 to Table 8-9), the influence of the length of the first section of the cord material model on the overall characteristics of the air spring is minimal. The axial force increases slightly with increasing length. Lateral and torsional stiffness decrease with increasing length but the total deviation remains insignificant. For air spring model B, the values are slightly higher with a maximum of 3.5 % lateral and 5 % torsional deviation.

8.1.2.1.2 Stiffness of Section 1

The other important parameter of the section 1 of the cord material model is the modulus of elasticity. The original value is 800 MPa and the variations range from 640 MPa (80 %) to 960 MPa (120 %). The change of the material stiffness of section 1 doesn't influence the stiffness of the second section, which remains at a value of 3.6 GPa (Table 8-10).

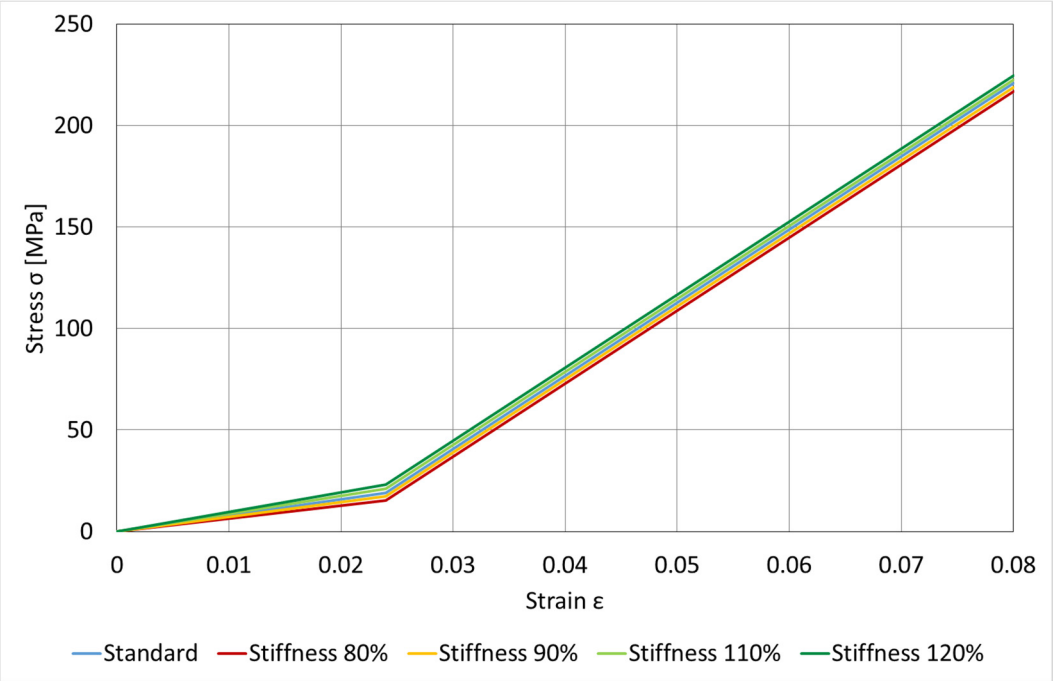

Table 8-10: Variation of cord material section 1: Stiffness

When comparing the graphic representations of the different material models for varying length (Table 8-6) and varying stiffness (Table 8-10) of section 1, it is assumed that the variation of section 1's stiffness is negligible compared to the variation of the length because it only slightly influences the overall material model.

Model A	%	Axial Force [kN]	Axial Stiffness [N/mm]	%	Lateral Stiffness [N/mm]	%	Torsional Stiffness [Nm/°]	%
Cord Model Section 1 - Stiffness	80	152.1	913.4	100.1	233.0	98.4	904.2	100.6
	90	152.0	908.2	99.5	236.7	100.0	899.6	100.1
	100	151.9	912.6	100.0	236.7	100.0	898.6	100.0
	110	151.9	912.9	100.0	236.3	99.8	897.8	99.9
	120	151.8	913.1	100.1	236.9	100.1	897.6	99.9

Table 8-11: Simulation results for varying stiffness of section 1 of the cord: Model A

Model B	%	Axial Force [kN]	Axial Stiffness [N/mm]	%	Lateral Stiffness [N/mm]	%	Torsional Stiffness [Nm/°]	%
Cord Model Section 1 - Stiffness	80	137.2	646.7	99.9	229.2	99.5	970.0	100.1
	90	137.1	646.5	99.9	229.9	99.9	972.9	100.4
	100	137.1	647.4	100.0	230.3	100.0	968.7	100.0
	110	137.0	647.2	100.0	230.5	100.1	963.1	99.4
	120	136.9	647.1	100.0	230.9	100.3	959.1	99.0

Table 8-12: Simulation results for varying stiffness of section 1 of the cord: Model B

Model C	%	Axial Force [kN]	Axial Stiffness [N/mm]	%	Lateral Stiffness [N/mm]	%	Torsional Stiffness [Nm/°]	%
Cord Model Section 1 - Stiffness	80	110.5	939.0	100.0	215.8	99.7	488.1	100.1
	90	110.5	938.7	99.9	215.8	99.8	484.2	99.3
	100	110.4	939.2	100.0	216.4	100.0	487.6	100.0
	110	110.4	938.0	99.9	215.0	99.4	480.4	98.5
	120	110.3	936.8	99.7	215.8	99.7	482.6	99.0

Table 8-13: Simulation results for varying stiffness of section 1 of the cord: Model C

The results corroborate the previously made assumption. The variation of the modulus of elasticity of section 1 by 40 % results only in very minor changes of the characteristics of the air spring. In contrast to the results of the varying length of section 1 in chapter 8.1.2.1.1, the stiffness variation only has a very small influence on lateral and torsional stiffness. These minor changes can be deemed negligible. Still, the importance of the first section of the cord material model cannot be neglected entirely since it influences the expansion of the air spring during inflation.

8.1.2.2 Section 2

The modulus of elasticity was varied for section 2 in the same way as it was done for section 1 in chapter 8.1.2.1.2. The original value was 3600 MPa and was tested from a minimum of 2880 MPa up to a maximum of 4320 MPa. Since the variation only starts at the end of section 1, this section is completely the same as in the original simulations.

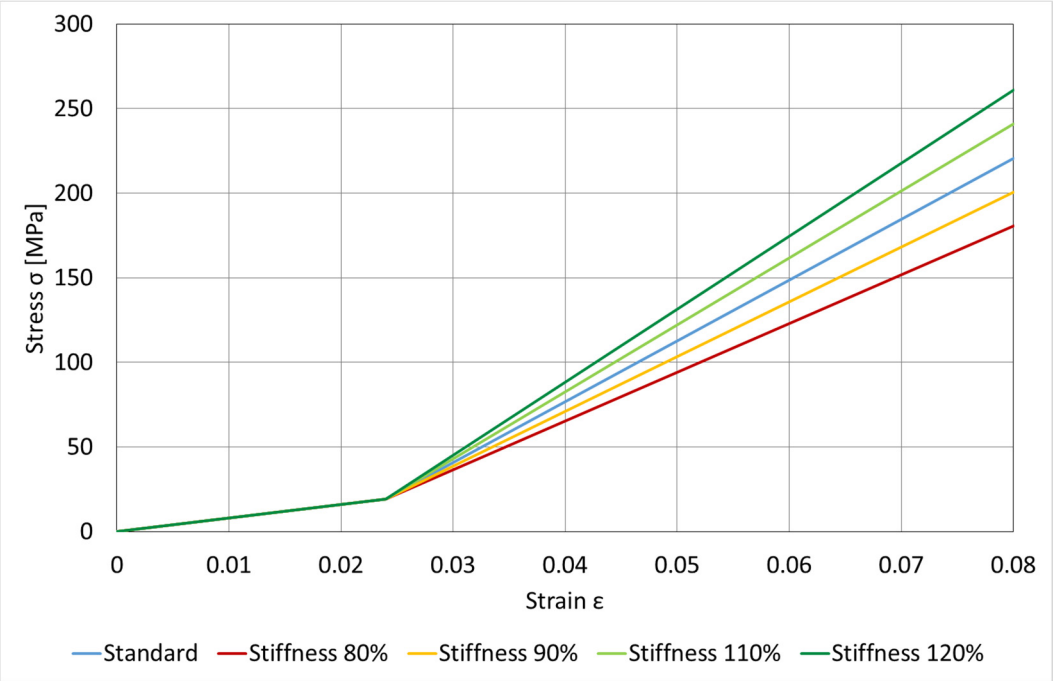

Table 8-14: Variation of cord material section 2: Stiffness

The difference between the variations shown in the table above (Table 8-14) and the variations shown in chapter 8.1.2.1 is blatant. Looking at the values at a strain of 0.08, which occurs at the end of section 2, the difference between the highest and the lowest value equals 80.64 MPa. By comparison, the same calculation done for the variation of the length of section 1 results in a change of 26.88 MPa and the variation of the stiffness of section 1 amounts to only 7.68 MPa. Since the strain during testing does not reach the value 0.8 but stays under it, the results do not differ as drastically.

Model A	%	Axial Force [kN]	Axial Stiffness [N/mm]	%	Lateral Stiffness [N/mm]	%	Torsional Stiffness [Nm/°]	%
Cord Model Section 2 - Stiffness	80	152.8	902.4	98.9	215.1	90.9	786.7	87.5
	90	152.2	908.1	99.5	224.4	94.8	845.3	94.1
	100	151.9	912.6	100.0	236.7	100.0	898.6	100.0
	110	151.6	908.0	99.5	244.8	103.4	951.2	105.9
	120	151.4	920.9	100.9	256.0	108.2	1000.6	111.4

Table 8-15: Simulation results for varying stiffness of section 2 of the cord: Model A

Model B	%	Axial Force [kN]	Axial Stiffness [N/mm]	%	Lateral Stiffness [N/mm]	%	Torsional Stiffness [Nm/°]	%
Cord Model Section 2 - Stiffness	80	138.2	638.0	98.5	205.1	89.0	833.0	86.0
	90	137.6	643.1	99.3	218.4	94.8	903.7	93.3
	100	137.1	647.4	100.0	230.3	100.0	968.7	100.0
	110	136.6	650.4	100.5	240.9	104.6	1031.4	106.5
	120	136.3	653.0	100.9	250.2	108.7	1092.1	112.7

Table 8-16: Simulation results for varying stiffness of section 2 of the cord: Model B

Model C	%	Axial Force [kN]	Axial Stiffness [N/mm]	%	Lateral Stiffness [N/mm]	%	Torsional Stiffness [Nm/°]	%
Cord Model Section 2 - Stiffness	80	110.6	934.5	99.5	204.2	94.4	439.8	90.2
	90	110.5	937.2	99.8	210.6	97.3	464.6	95.3
	100	110.4	939.2	100.0	216.4	100.0	487.6	100.0
	110	110.4	939.0	100.0	222.3	102.7	504.0	103.4
	120	110.3	940.2	100.1	225.8	104.4	523.1	107.3

Table 8-17: Simulation results for varying stiffness of section 2 of the cord: Model C

The simulated results show a negligible influence on the axial force as well as the axial stiffness for all three air spring models. The influence on the lateral stiffness and the torsional stiffness is very interesting because it can be used as a corroboration of the results in chapter 8.1.1. There, it was shown that the variation of the elastomer model had the biggest influence on the air spring model C. By comparison, the simulations in this chapter show the influence of the cord material and thus should have a counter tendency in that the influence of the cord on the stiffness of the air spring model C should be the smallest. The results above (Table 8-15 to Table 8-17) proove this assumption as the influence on the lateral stiffness of model A and B with a maximum value of 20 % is higher than the one on model C with only 10 %. This effect can be accredited to the angle of the cord layers, which influences how much force the cord can take and how much the elastomer has to absorb.

8.1.2.3 Section 3

After many test series with the stiffness and length of section 3, it was discovered, that this section does not influence the stiffness because this part is never reached during the different tests (axial, lateral and torsional stiffness simulations). The section, however, should continue to be included in the material model in the event of tests focusing on different factors than the ones carried out here.

8.1.3 Steel

The steel wire-cores are much stiffer than the rest of the materials of the air springs. They do not deform under the working conditions and thus a simulation of different materials will not deliver any valuable results.

8.2 Geometry

The second part of the variations deals with the geometry of the simulation models. In chapter 6.2.1, it was described, how the contour of the simulation models was developed and which problems were encountered. To get an idea how the contour affects the characteristics of the whole airs spring, the different parts will be varied and evaluated separately.

8.2.1 Rebar Angle

This part deals with the original rebar angle which is used during the manufacturing of the air spring. The exact process is described in chapter 4.4. The rebar angle of the air spring can be easily varied during the manufacturing by changing the original rebar angle. To show the influence, the original rebar angle will be varied in the simulation. Since only integral numbers were used for the rebar angle, the percentage difference between the different variations changes between the three different air spring models.

Model A	%	Axial Force [kN]	Axial Stiffness [N/mm]	%	Lateral Stiffness [N/mm]	%	Torsional Stiffness [Nm/°]	%
13 °	86.7	156.0	968.2	106.1	221.2	93.5	798.8	88.9
14 °	93.3	154.0	937.9	102.8	229.2	96.9	849.9	94.6
15 °	100.0	151.9	912.6	100.0	236.7	100.0	898.6	100.0
16 °	106.7	149.5	874.2	95.8	234.8	99.2	954.9	106.3
17 °	113.3	147.1	836.4	91.7	239.9	101.4	990.4	110.2

Table 8-18: Simulation results for varying rebar angles: Model A

Model B	%	Axial Force [kN]	Axial Stiffness [N/mm]	%	Lateral Stiffness [N/mm]	%	Torsional Stiffness [Nm/°]	%
16 °	88.9	146.3	764.5	118.1	195.9	85.1	940.8	97.1
17 °	94.4	141.9	706.2	109.1	213.4	92.7	961.6	99.3
18 °	100.0	137.1	647.4	100.0	230.3	100.0	968.7	100.0
19 °	105.6	131.7	582.5	90.0	238.1	103.4	957.4	98.8
20 °	111.1	125.9	513.5	79.3	245.3	106.5	923.8	95.4

Table 8-19: Simulation results for varying rebar angles: Model B

Model C	%	Axial Force [kN]	Axial Stiffness [N/mm]	%	Lateral Stiffness [N/mm]	%	Torsional Stiffness [Nm/°]	%
5 °	71.4	111.1	947.3	100.9	186.3	86.1	357.3	73.3
6 °	85.7	110.8	941.0	100.2	199.7	92.3	413.5	84.8
7 °	100.0	110.4	939.2	100.0	216.4	100.0	487.6	100.0
8 °	114.3	110.1	947.8	100.9	231.9	107.2	557.0	114.2
9 °	128.6	109.4	914.5	97.4	248.2	114.7	631.7	129.6

Table 8-20: Simulation results for varying rebar angles: Model C

As the simulation results above (Table 8-18 to Table 8-20) show, the whole process is not as simple as it might seem. Logic would dictate that if the customer wants an air spring with higher stiffness, the easiest way would be to change the rebar angle during manufacturing. It is clearly shown that the rebar angle has a big influence on the characteristics of air springs, but there are many factors which interact. This can be seen here as well. The axial stiffness of the air spring model C barely changes (<3 %) while the axial stiffness of the other two models varies strongly, up to 40 %. The same effect can be witnessed for the torsional stiffness, even though here the influence ranges from a minimum of 5 % for model B with the overall highest rebar angles to a huge deviation of 60 % for model C, which has the smallest rebar angles. The lateral stiffness differs between the three air spring models, but not as much as the axial and torsional stiffness.

8.2.2 Number of Cord Strings

The number of cord strings was measured on a small part of the air springs and then upscaled as described in chapter 4.3.2. Since this method depends heavily on the exactness of the measurements, the influence of the number of cord strings has to be tested. As before in chapter 8.2.1, the percentage difference between the different

variations changes between the 3 different air spring models, but due to the fact that the measured values had to be upscaled to arrive at the standard values, variations smaller than 50 were deemed unrealistic because the measurements would not be exact enough.

Model A	%	Axial Force [kN]	Axial Stiffness [N/mm]	%	Lateral Stiffness [N/mm]	%	Torsional Stiffness [Nm/°]	%
850 #	89.5	152.4	906.5	99.3	224.2	94.7	841.7	93.7
900 #	94.7	152.2	910.2	99.7	232.1	98.1	870.9	96.9
950 #	100.0	151.9	912.6	100.0	236.7	100.0	898.6	100.0
1000 #	105.3	151.7	914.7	100.2	240.3	101.5	925.1	102.9
1050 #	110.5	151.5	916.8	100.5	245.3	103.6	952.7	106.0

Table 8-21: Simulation results for varying number of cord strings: Model A

Model B	%	Axial Force [kN]	Axial Stiffness [N/mm]	%	Lateral Stiffness [N/mm]	%	Torsional Stiffness [Nm/°]	%
1000 #	90.9	137.6	643.8	99.4	219.3	95.2	912.6	94.2
1050 #	95.5	137.3	645.6	99.7	224.8	97.6	940.8	97.1
1100 #	100.0	137.1	647.4	100.0	230.3	100.0	968.7	100.0
1150 #	104.5	136.8	648.7	100.2	235.3	102.2	994.8	102.7
1200 #	109.1	136.6	650.2	100.4	240.3	104.4	1019.7	105.3

Table 8-22: Simulation results for varying number of cord strings: Model B

Model C	%	Axial Force [kN]	Axial Stiffness [N/mm]	%	Lateral Stiffness [N/mm]	%	Torsional Stiffness [Nm/°]	%
1400 #	93.3	110.5	938.4	99.9	212.0	98.0	469.6	96.3
1450 #	96.7	110.5	939.0	100.0	214.2	99.0	478.6	98.2
1500 #	100.0	110.4	939.2	100.0	216.4	100.0	487.6	100.0
1550 #	103.3	110.4	939.4	100.0	216.3	100.0	485.2	99.5
1600 #	106.7	110.3	939.6	100.0	218.3	100.9	493.9	101.3

Table 8-23: Simulation results for varying number of cord strings: Model C

As shown in the tables above (Table 8-21 to Table 8-23), the number of cord strings was varied by about 20 %. This should cover the inaccuracies of the measurements and the upscaling of the results. The effect on the axial stiffness with less than 1.5 % deviation is clearly negligible. A minor change of the number of cord strings also only results in small deviations for lateral and torsional stiffness. The whole simulation ensures the sufficient accuracy of the measurement system of the number of cord

strings. At the same time it shows that a large variation of the number of cord strings during the manufacturing will influence the characteristics of the air spring.

The stiffness of the elastomer-cord composite is defined, among other factors, like the rebar angle, by the ratio of cord to elastomer. Since this value is influenced by the number of cord strings and the rebar area, the correlation between those two parameters had to be examined further. For the test, the rebar area was multiplied by 1000 and divided by 950 to see if the results match those of model A with 1000 cord strings per meter.

Model A	Axial Force [kN]	Axial Stiffness [N/mm]	Lateral Stiffness [N/mm]	Torsional Stiffness [Nm/°]
1000 #	151.7	914.7	240.3	925.1
A-Rebar 1000/950	151.7	914.7	240.3	925.1

Table 8-24: Comparison of varied rebar area and number of cord strings

The results match exactly and prove that MSC Marc Mentat only uses the ratio between cord and elastomer. It does not matter, if there are 1000 strings with an area of 1 mm^2 or if there is 1 string with an area of 1000 mm^2, the programme only uses the volume of the cord.

8.2.3 Foldover at the Clamping Ring

Another difference between the three air spring models is the length of the foldovers at the clamping ring as well as at the rim. Since it can be assumed, that the length difference is not just coincidence during the manufacturing process, the influence of the lengths and forms of the foldovers needs to be investigated.

8.2.3.1 Varying Length

The first variation in the outer form of the air spring is the variation of the foldover length at the clamping ring. The length was varied from a minimum, which was defined as 30 mm shorter than the standard, to a maximum of 30 mm longer than the standard length.

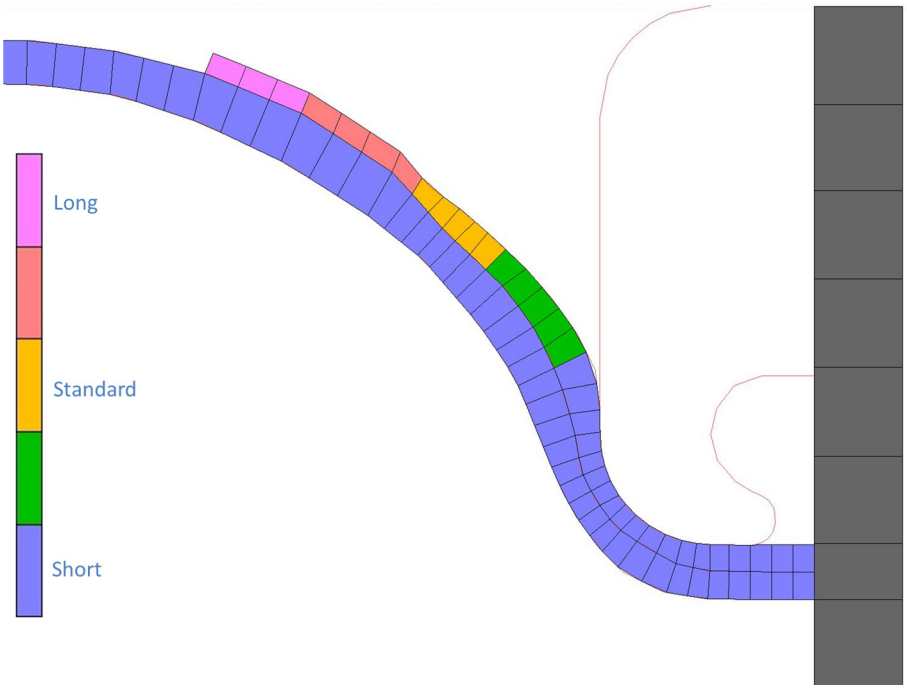

Figure 8-1: Variation of the foldover length at the clamping ring

Model A	%	Axial Force [kN]	Axial Stiffness [N/mm]	%	Lateral Stiffness [N/mm]	%	Torsional Stiffness [Nm/°]	%
Foldover Clamping Ring Length	Short	151.7	909.8	99.7	232.3	98.2	884.9	98.5
		151.8	910.3	99.7	235.0	99.3	891.5	99.2
	Standard	151.9	912.6	100.0	236.7	100.0	898.6	100.0
		152.0	917.6	100.5	239.4	101.2	907.6	101.0
	Long	151.9	920.0	100.8	241.2	101.9	912.0	101.5

Table 8-25: Simulation results for varying foldover length at the clamping ring: Model A

Model B	%	Axial Force [kN]	Axial Stiffness [N/mm]	%	Lateral Stiffness [N/mm]	%	Torsional Stiffness [Nm/°]	%
Foldover Clamping Ring Length	Short	137.0	641.2	99.0	218.9	95.1	955.0	98.6
		137.0	644.1	99.5	225.8	98.1	962.9	99.4
	Standard	137.1	647.4	100.0	230.3	100.0	968.7	100.0
		137.1	650.0	100.4	232.8	101.1	972.7	100.4
	Long	137.0	652.1	100.7	235.2	102.2	976.2	100.8

Table 8-26: Simulation results for varying foldover length at the clamping ring: Model B

Model C	Length	Axial Force [kN]	Axial Stiffness [N/mm]	%	Lateral Stiffness [N/mm]	%	Torsional Stiffness [Nm/°]	%
Foldover Clamping Ring Length	Short	110.4	932.0	99.2	195.8	90.5	469.4	96.3
		110.4	932.4	99.3	210.3	97.2	473.4	97.1
	Standard	110.4	939.2	100.0	216.4	100.0	487.6	100.0
		110.4	934.9	99.5	219.8	101.6	489.6	100.4
	Long	110.4	936.4	99.7	222.1	102.7	491.1	100.7

Table 8-27: Simulation results for varying foldover length at the clamping ring: Model C

The variation of the foldover length at the clamping ring results only in very minor deviations for the axial stiffness and thus renders these values negligible. The torsional stiffness shows a clear tendency to increase with increasing foldover length, but the absolute values do not differ greatly. The lateral stiffness shows a clear tendency, as it increases with increasing foldover length at the clamping ring.

8.2.3.2 Varying Angle

The next possibility to change the foldover area so it might reveal its influence on the air spring characteristics was to change the angle of the foldover with regard to its original position. The thickness and length of the foldover remained the same during the variations so as to minimise influences other than its position.

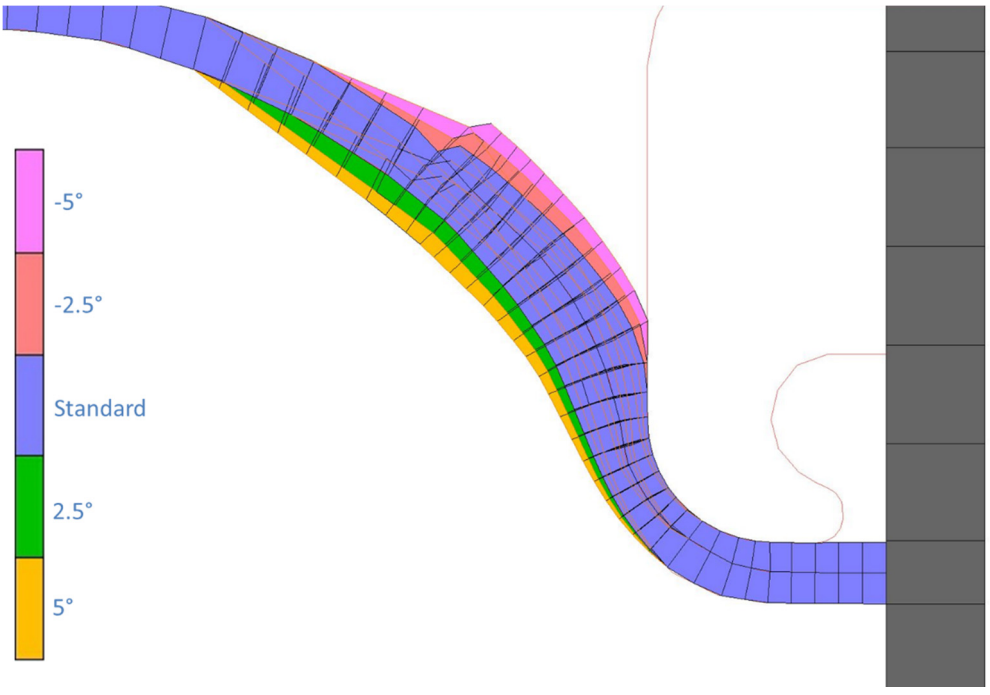

Figure 8-2: Variation of the angle at the clamping ring foldover

Model A	%	Axial Force [kN]	Axial Stiffness [N/mm]	%	Lateral Stiffness [N/mm]	%	Torsional Stiffness [Nm/°]	%
Foldover Clamping Ring Angle	-5.0	152.8	914.7	100.2	212.5	89.8	903.0	100.5
	-2.5	152.2	915.7	100.3	227.6	96.2	901.3	100.3
	Standard	151.9	912.6	100.0	236.7	100.0	898.6	100.0
	2.5	152.2	959.8	105.2	235.6	99.6	897.7	99.9
	5.0	151.6	941.5	103.2	238.7	100.9	897.1	99.8

Table 8-28: Simulation results for varying angle of the foldover area at the clamping ring: Model A

The most interesting stiffness here is the lateral one. As shown above (Table 8-28), the lateral stiffness of model A increases drastically upon variation of the angle from -5° to the standard value of 0°. After this point, the stiffness basically stays the same. This interesting effect is linked to the contact area of the bellows and the clamping ring. In the following figures (Figure 8-3 to Figure 8-7), the contact between those two bodies is displayed. If the bodies are in contact, the area is displayed in yellow and if there is no contact detected, the area is shown in blue. The different shades in-between those colours are irrelevant.

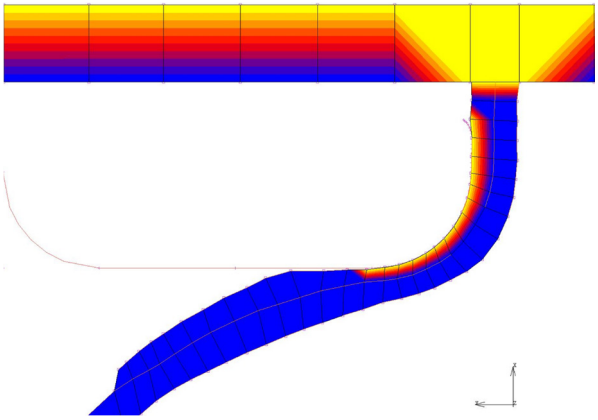

Figure 8-3: Contact status of air spring model A at working pressure: -5°

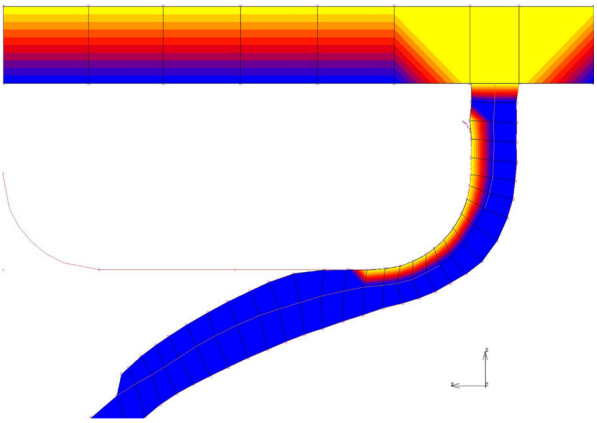

Figure 8-4: Contact status of air spring model A at working pressure: -2.5°

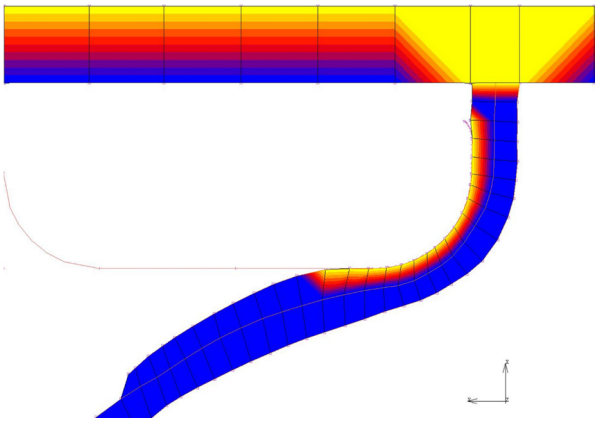

Figure 8-5: Contact status of air spring model A at working pressure: 0°

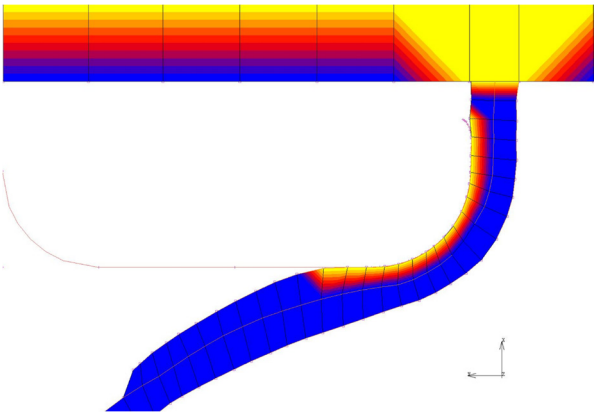

Figure 8-6: Contact status of air spring model A at working pressure: 2.5°

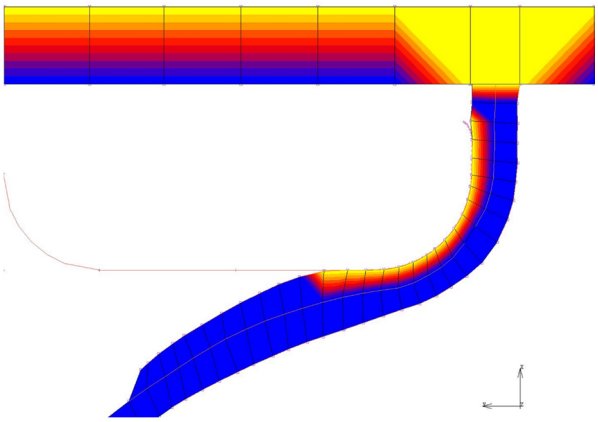

Figure 8-7: Contact status of air spring model A at working pressure: 5°

The first thing that catches the eye is that the contact area of the depictions of the model at 0°, 2.5° and 5° (Figure 8-5 to Figure 8-7) is the same. This correlates with the results presented above (Table 8-28) as the lateral stiffness nearly stays the same during this variation. The contact area of the model at -5° and -2.5° (Figure 8-3, Figure 8-4) is clearly smaller, which corroborates the assumption previously made. Due to the segment-to-segment contact, the element edge is divided by auxiliary points. Apparently, in the model at -5° (Figure 8-3), a smaller number of these auxiliary points is defined as being "in contact" than in the model at -2.5° (Figure 8-4). Due to the fact that these auxiliary points are only available during contact checking, such small differences in contact area can't be displayed in the results file where only the whole elements are shown. This is the reason that the contact area of the models at -5° and -2.5° looks the same but the results still show that the models have different lateral stiffness.

Model B	%	Axial Force [kN]	Axial Stiffness [N/mm]	%	Lateral Stiffness [N/mm]	%	Torsional Stiffness [Nm/°]	%
Foldover Clamping Ring Angle	-5.0	137.6	645.4	99.7	223.7	97.1	969.6	100.1
	-2.5	137.3	647.1	100.0	234.3	101.8	969.4	100.1
	Standard	137.1	647.4	100.0	230.3	100.0	968.7	100.0
	2.5	136.9	649.2	100.3	231.9	100.7	969.2	100.1
	5.0	136.7	650.4	100.5	233.5	101.4	969.5	100.1

Table 8-29: Simulation results for varying angle of the foldover area at the clamping ring: Model B

Model C	Angle	Axial Force [kN]	Axial Stiffness [N/mm]	%	Lateral Stiffness [N/mm]	%	Torsional Stiffness [Nm/°]	%
Foldover Clamping Ring Angle	-5.0	110.7	935.2	100.3	216.6	100.1	477.7	98.0
	-2.5	110.5	934.3	100.1	216.2	99.9	477.0	97.8
	Standard	110.4	939.2	100.0	216.4	100.0	487.6	100.0
	2.5	110.3	939.3	99.9	216.3	100.0	487.3	99.9
	5.0	110.2	933.8	99.8	213.8	98.8	475.8	97.6

Table 8-30: Simulation results for varying angle of the foldover area at the clamping ring: Model C

The effect described above could not be reproduced for model B and C since the contour of those two models is different and the change of the angle of foldover area at the clamping ring did not have enough influence as to change the contact area. The

latter stayed the same throughout the variation process, which is reflected by the results, which in turn never deviate significantly from the standard value.

The torsional stiffness isn't influenced by this effect because the forces of the rotation mainly act at the inner part of the air spring, which is the area of the rim. This effect is tested in the next chapter during the variation of the foldover at the rim.

8.2.4 Foldover at the Rim

8.2.4.1 Varying Length

Analogous to the variation of the foldover length at the clamping ring in chapter 8.2.3.1, the length at the rim will be varied in this chapter. Per simulation, the foldover was lengthened by an average of 15 mm.

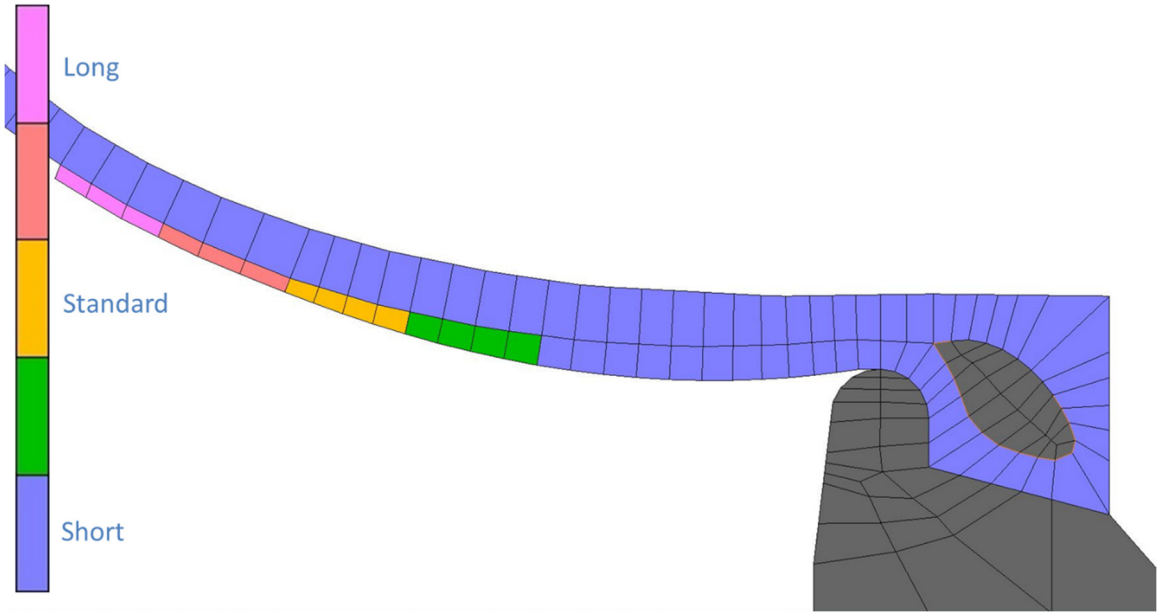

Figure 8-8: Variation of the foldover length at the rim

Model A	%	Axial Force [kN]	Axial Stiffness [N/mm]	%	Lateral Stiffness [N/mm]	%	Torsional Stiffness [Nm/°]	%
Foldover Rim Length	Short	152.6	915.3	100.3	226.9	95.9	837.9	93.2
		152.2	915.7	100.3	230.0	97.2	884.6	98.4
	Standard	151.9	912.6	100.0	236.7	100.0	898.6	100.0
		151.7	913.9	100.1	236.9	100.1	936.6	104.2
	Long	151.5	913.8	100.1	240.0	101.4	965.2	107.4

Table 8-31: Simulation results for varying foldover length at the rim: Model A

Model B	%	Axial Force [kN]	Axial Stiffness [N/mm]	%	Lateral Stiffness [N/mm]	%	Torsional Stiffness [Nm/°]	%
Foldover Rim Length	Short	137.9	645.3	99.7	220.9	95.9	901.3	93.0
		137.4	647.5	100.0	225.8	98.1	950.9	98.2
	Standard	137.1	647.4	100.0	230.3	100.0	968.7	100.0
		136.9	645.8	99.8	232.5	101.0	976.5	100.8
	Long	136.8	644.7	99.6	236.0	102.5	1007.7	104.0

Table 8-32: Simulation results for varying foldover length at the rim: Model B

Model C	Length	Axial Force [kN]	Axial Stiffness [N/mm]	%	Lateral Stiffness [N/mm]	%	Torsional Stiffness [Nm/°]	%
Foldover Rim Length	Short	111.5	918.7	97.8	207.8	96.0	458.8	94.1
		111.0	926.1	98.6	212.0	98.0	474.1	97.2
	Standard	110.4	939.2	100.0	216.4	100.0	487.6	100.0
		110.0	952.2	101.4	217.8	100.7	488.5	100.2
	Long	109.6	941.8	100.3	222.2	102.7	513.0	105.2

Table 8-33: Simulation results for varying foldover length at the rim: Model C

The results show a clear tendency for the axial force to decrease with increasing foldover length. The changes are very small and consequently the axial stiffness does not necessarily follow the reversed trend as would be expected. Model C shows a small increase in axial stiffness, but the other two models have only negligible changes around the standard value. The lateral stiffness as well as the torsional stiffness follow a trend as they increase with increasing foldover length. The torsional stiffness is influenced more than the lateral stiffness by the foldover at the rim, which follow the logic that the rim area should have more influence on the torsional stiffness and the clamping ring area should have more influence on the lateral stiffness.

8.2.4.2 Varying Angle

The variation of the foldover angle at the rim was done exactly the same way as at the clamping ring. The whole foldover area was rotated by the specific angles without changing the length, form or width of the foldover area itself. The only adjustment that had to be made concerned the elements right after the foldover area, which had to be adjusted so as to create a reasonably smooth overall contour.

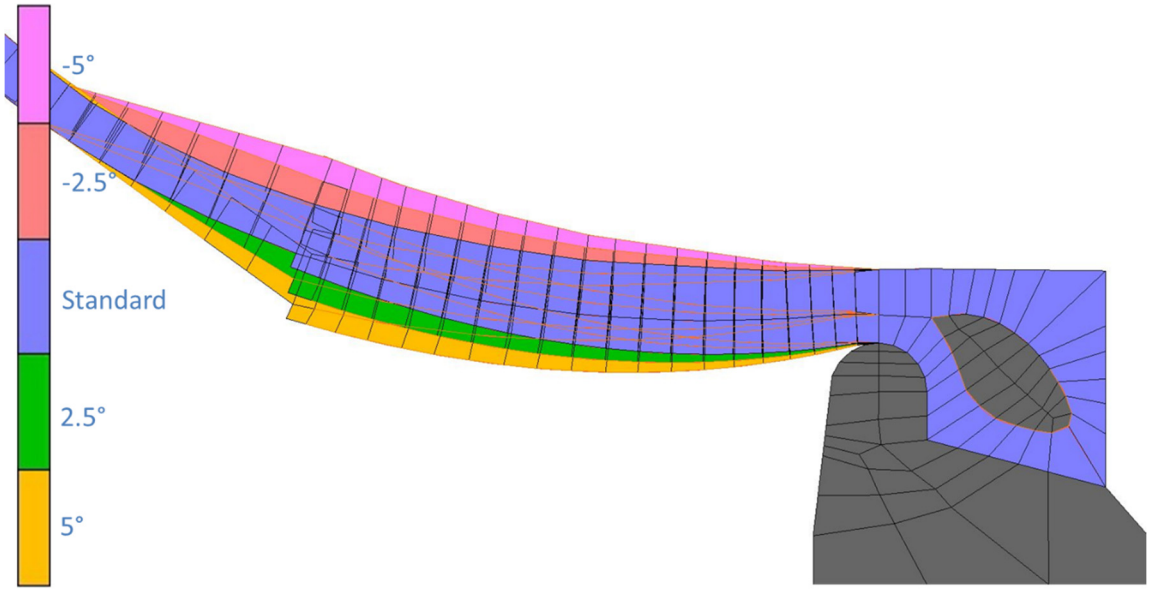

Figure 8-9: Variation of the angle at the rim foldover

Model A	%	Axial Force [kN]	Axial Stiffness [N/mm]	%	Lateral Stiffness [N/mm]	%	Torsional Stiffness [Nm/°]	%
Foldover Rim Angle	-5.0	152.1	915.4	100.3	238.2	100.6	916.0	101.9
	-2.5	151.9	915.0	100.3	233.8	98.8	899.6	100.1
	Standard	151.9	912.6	100.0	236.7	100.0	898.6	100.0
	2.5	152.0	910.6	99.8	232.0	98.0	894.8	99.6
	5.0	152.1	907.7	99.5	234.4	99.1	910.7	101.4

Table 8-34: Simulation results for varying angle of the foldover area at the rim: Model A

Model B	%	Axial Force [kN]	Axial Stiffness [N/mm]	%	Lateral Stiffness [N/mm]	%	Torsional Stiffness [Nm/°]	%
Foldover Rim Angle	-5.0	137.3	650.9	100.5	231.0	100.3	993.1	102.5
	-2.5	137.2	649.2	100.3	230.5	100.1	982.3	101.4
	Standard	137.1	647.4	100.0	230.3	100.0	968.7	100.0
	2.5	137.0	644.7	99.6	229.7	99.7	955.8	98.7
	5.0	136.9	641.6	99.1	229.0	99.4	945.3	97.6

Table 8-35: Simulation results for varying angle of the foldover area at the rim: Model B

Model C	Angle	Axial Force [kN]	Axial Stiffness [N/mm]	%	Lateral Stiffness [N/mm]	%	Torsional Stiffness [Nm/°]	%
Foldover Rim Angle	-5.0	110.6	940.7	100.2	216.2	99.9	485.5	99.6
	-2.5	110.5	939.7	100.1	216.2	99.9	486.4	99.8
	Standard	110.4	939.2	100.0	216.4	100.0	487.6	100.0
	2.5	110.4	936.0	99.7	217.0	100.3	487.7	100.0
	5.0	110.5	932.2	99.3	215.2	99.5	488.2	100.1

Table 8-36: Simulation results for varying angle of the foldover area at the rim: Model C

The results show that the influence of the foldover angle at the rim is negligible for stiffness on all three counts. All values deviate insignificantly from the standard. The reason for this is the constant contact area at the rim in contrast to the angle variation at the clamping ring. Due to this lack of change, the only difference between the simulations is the minimal change in volume of the air spring generated by the change of the angles. This minor change does not influence the stiffness in any noticeable way.

8.2.5 Number of Subdivisions for 2D to 3D Expansion

The standard used for all the simulation models above is an expansion of 15° per subdivision, which is rotated 24 times to get the full 360° 3D model. 15° were chosen because the low number of elements was very beneficial for the simulation times as well as the simulation results. To check the influence of the number of subdivisions, the original model was compared to a model which was rotated 36 times with 10° per subdivision and a model rotated 72 times with 5° per subdivision. Smaller subdivisions were not tested because the simulation times of the 5°x72 model were already very long because it has an enormous total number of 125496 elements for model A. Larger subdivisions than 15° were tested, but the results became less accurate or the simulations did not even work because the elements were too distorted right from the beginning.

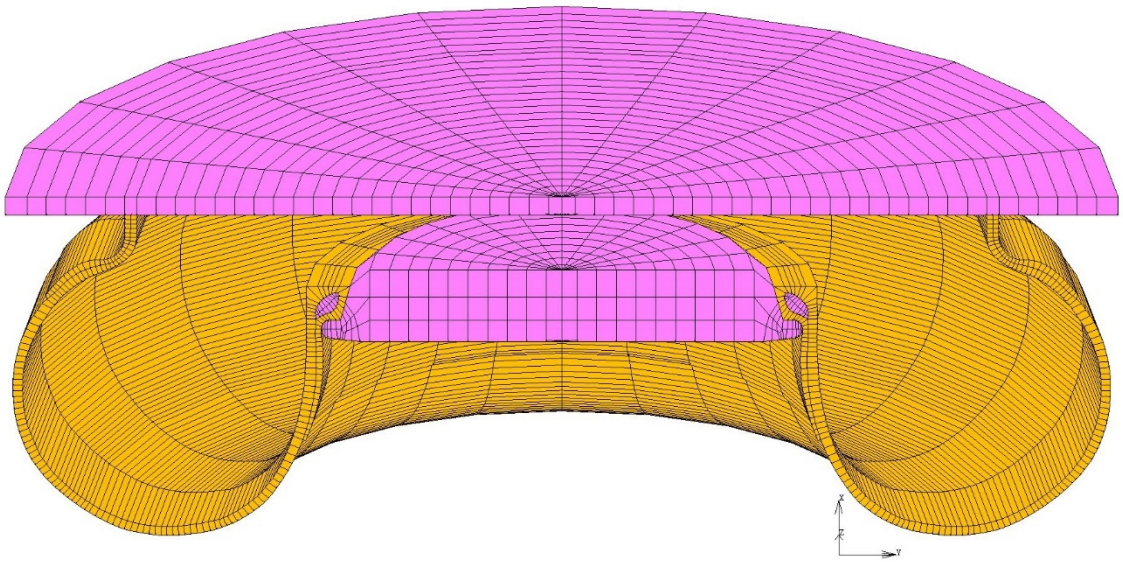

Figure 8-10: Sectional view of model A: Rotation 15°x24

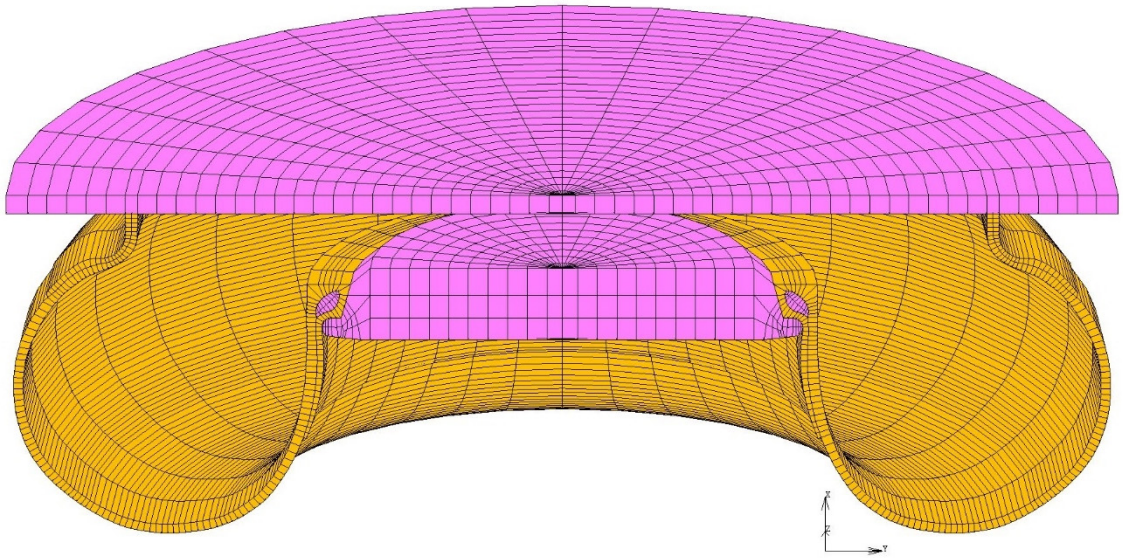

Figure 8-11: Sectional view of model A: Rotation 10°x36

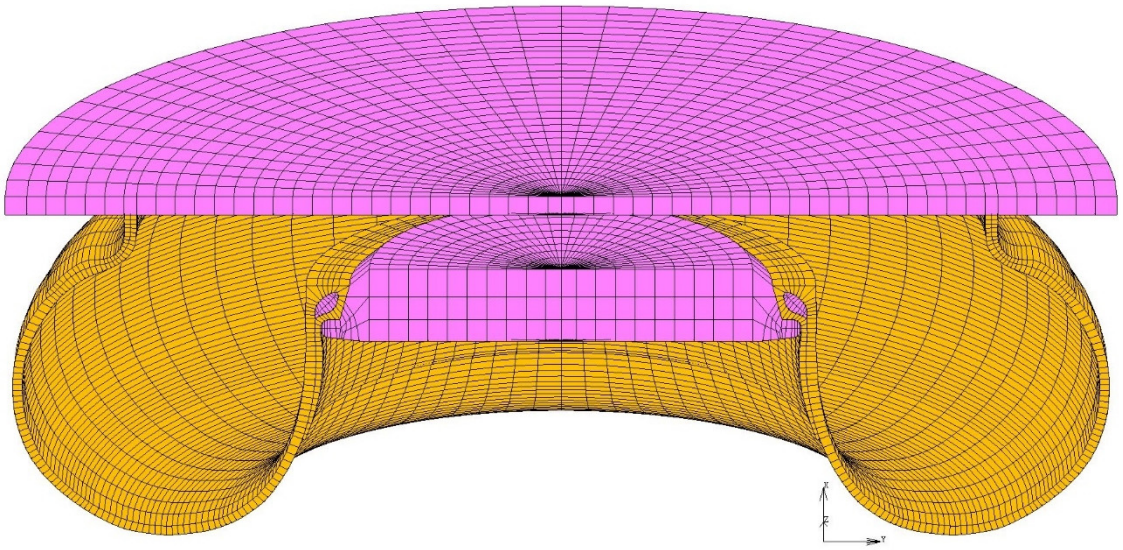

Figure 8-12: Sectional view of model A: Rotation 5°x72

Model A		Axial Force [kN]	Axial Stiffness [N/mm]	%	Lateral Stiffness [N/mm]	%	Torsional Stiffness [Nm/°]	%
Rotation	15°x24	151.9	912.6	100.0	236.7	100.0	898.6	100.0
	10°x36	-	-	-	229.2	96.9	916.0	101.9
	5°x72	-	-	-	227.5	96.1	911.1	101.4

Table 8-37: Results for varying subdivisions during rotation: Model A

Model B		Axial Force [kN]	Axial Stiffness [N/mm]	%	Lateral Stiffness [N/mm]	%	Torsional Stiffness [Nm/°]	%
Rotation	15°x24	137.1	647.4	100.0	230.3	100.0	986.7	100.0
	10°x36	-	-	-	221.3	96.1	970.8	98.4
	5°x72	-	-	-	216.0	93.8	971.6	98.5

Table 8-38: Results for varying subdivisions during rotation: Model B

Model C		Axial Force [kN]	Axial Stiffness [N/mm]	%	Lateral Stiffness [N/mm]	%	Torsional Stiffness [Nm/°]	%
Rotation	15°x24	110.4	939.2	100.0	216.4	100.0	487.6	100.0
	10°x36	-	-	-	213.6	98.7	481.1	98.7
	5°x72	-	-	-	210.7	97.4	477.0	97.8

Table 8-39: Results for varying subdivisions during rotation: Model C

8.2.6 Modelling of the Clamping Ring Area

Since the models used in all the simulations shown above were simplified by excluding the clamping ring area, the influence of this specific area has to be tested. The geometrical difference between the standard model and the model in this chapter is the expansion of the rubber-cord composite elements from the upper plate going around the outer steel-wire core and back to the foldover area. To model the part around the steel core more realistically, five rubber elements had to be inserted to form a buffer between the standard and the foldover part of the air spring. The other difference between the two models is the contact definition between the upper plate and the bellows. In prior models, the contact mode “glue” had to be used to ensure the air tightness of the air spring. In this model, which represents reality more closely, the contact definition was changed to “touching”. This means that the elements of the bellows and the upper plate have friction between them, which means that consequently the elements cannot just slide but have a force working against this motion. If the forces get strong enough, the elements can slide and move away from each other.

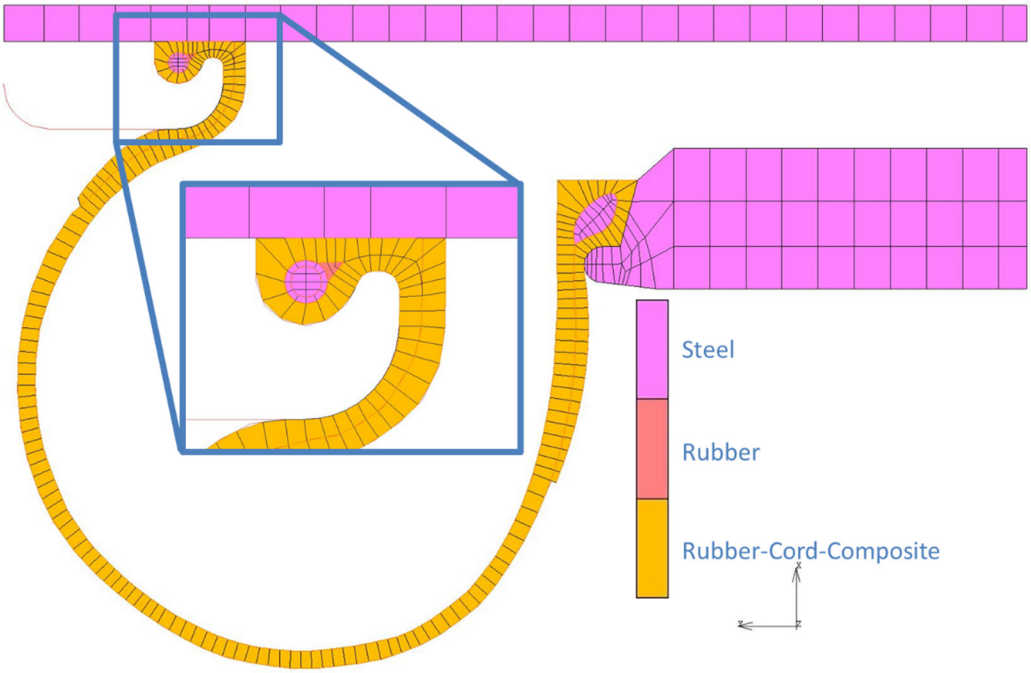

Figure 8-13: Modelling of the clamping ring area

Figure 8-13 shows the model with detailed view of the clamping ring area. In the picture below (Figure 8-14), the same clamping ring area is shown under operating pressure. As can be seen, the innermost elements at the contact area of upper plate and air spring bellows have parted because of inner pressure. This results in a slightly different contour for the whole air spring and explains the deviations of the results compared to the models without the detailed clamping ring area.

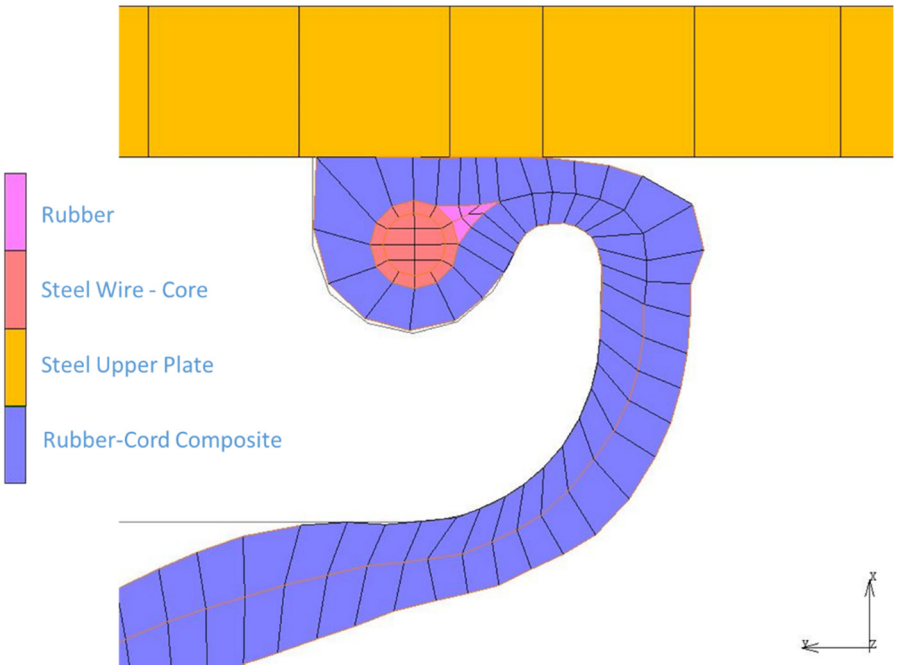

Figure 8-14: Detailed view of the clamping ring area at operating pressure

	Axial Force [kN]	%	Axial Stiffness [N/mm]	%	Lateral Stiffness [N/mm]	%	Torsional Stiffness [Nm/°]	%
Model A								
Standard	151.9		912.6		236.7		898.5	
Clamping Ring - Detail	152.9	100.6	916.5	100.4	217.8	92.0	893.8	99.5
Model B								
Standard	137.1		647.4		230.3		968.7	
Clamping Ring - Detail	137.6	100.4	638.2	98.6	228.2	99.1	920.5	95.0
Model C								
Standard	110.4		939.2		216.4		487.6	
Clamping Ring - Detail	111.7	101.2	938.0	99.9	212.5	98.2	478.7	98.2

Table 8-40: Comparison of simulation models with and without detailed modelling of the clamping ring area

As the results above (Table 8-40) show, the axial force, which is directly connected to the volume of the air spring, tends to increase slightly. The lateral as well as the torsional stiffness decrease within an area of 5 %. The simulations do not run as smoothly as with the standard model and as a consequence, the results, as shown below (Table 8-41), become a little rougher.

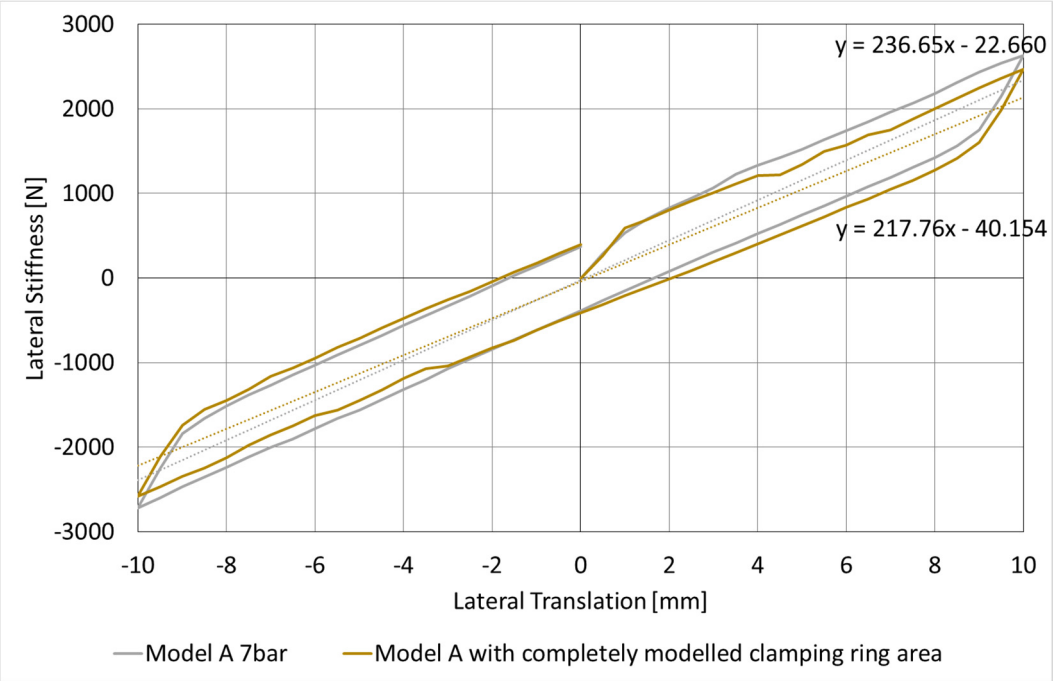

Table 8-41: Simulation result of lateral stiffness of air spring model A with completely modelled clamping ring area

8.2.7 Detailed Model

For the lifespan estimation demanded by Siemens AG, a more detailed model had to be generated. This chapter deals with the development of different models and the problems that were encountered.

8.2.7.1 First Version of a Detailed Model

The first attempt at creating a detailed model can be seen in the figure below (Figure 8-15). The standard model was used as a basis for this new model. The rubber-cord composite elements were subdivided into three different sections: the outer rubber layer, the inner rubber layer and the rubber-cord composite in between. Since air springs are manufactured in this fashion, it was assumed that this subdivision would produce more accurate results. After a large number of tests and different adjustments, the simulations still would not finish. The variation of stiffness between the elements that only used the rubber material and the elements that were reinforced by the cord material in combination with the still relatively large elements led to problems with the stability of the model. During the simulations, some nodes would start to oscillate more and more until the simulation had to be aborted.

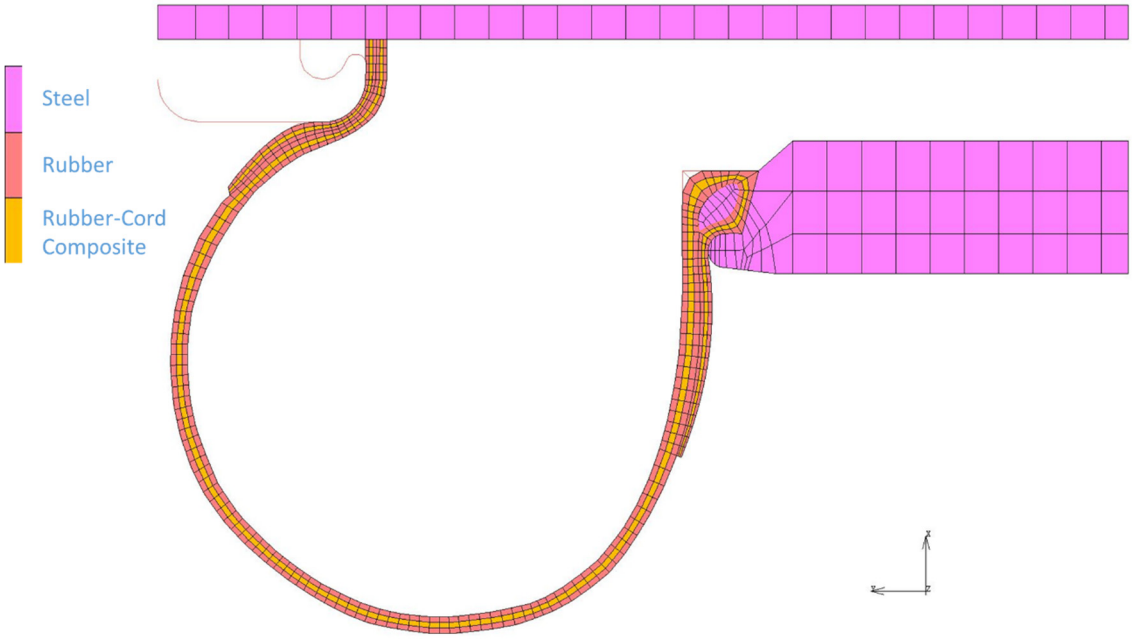

Figure 8-15: First version of a detailed model

8.2.7.2 Detailed Model for Stiffness Simulation

The next step in the development of a detailed model can be seen in the depiction below (Figure 8-16).

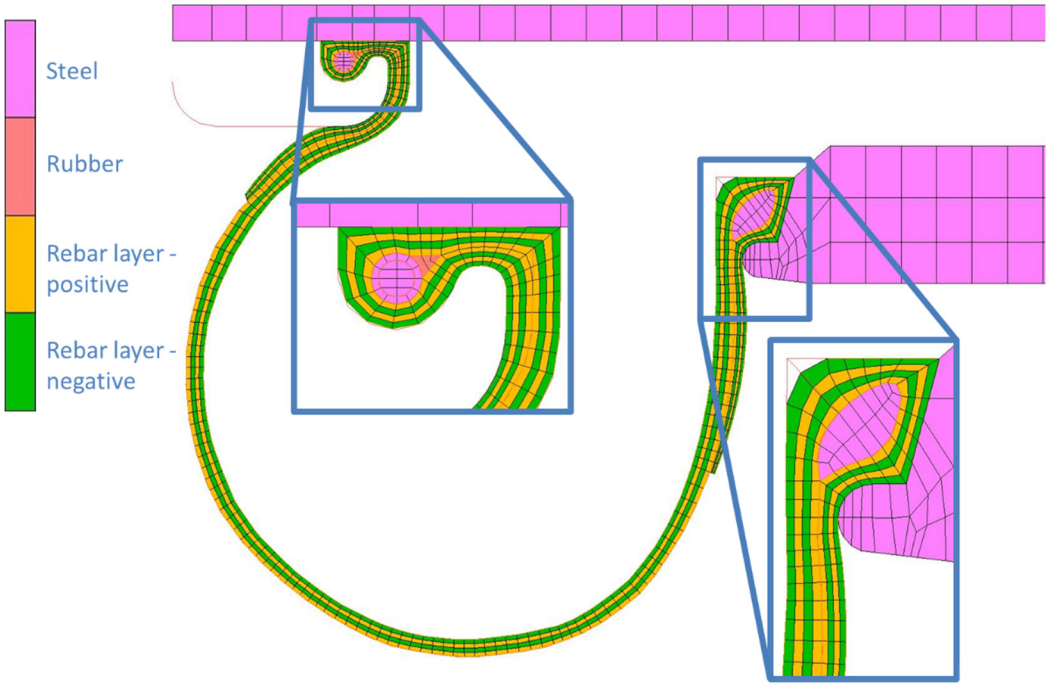

Figure 8-16: Detailed model for stiffness simulation

For this model, a new approach was tested. The rebar layer was divided into the four single layers that are used in the design of the actual air springs, but the inner and outer layer made purely out of rubber were neglected to get a more stable simulation. This model worked well and was further developed by including the detailed model of the clamping ring area. In the picture above (Figure 8-16), the clamping ring area and the area of the inner steel-wire core are enlarged. The positive cord layer is depicted in yellow and the negative layer in green. The limitation of this model is its uselessness for damage evaluation. The problems referenced in the introduction of this thesis always occur at the end of a foldover in the areas that consist solely of rubber. Since these areas were ignored in this model, this problem could not be addressed and necessitated a further stage of model development.

8.2.7.3 Detailed Model for Damage Evaluation

The final model of the development process is the model for damage evaluation depicted below (Figure 8-17).

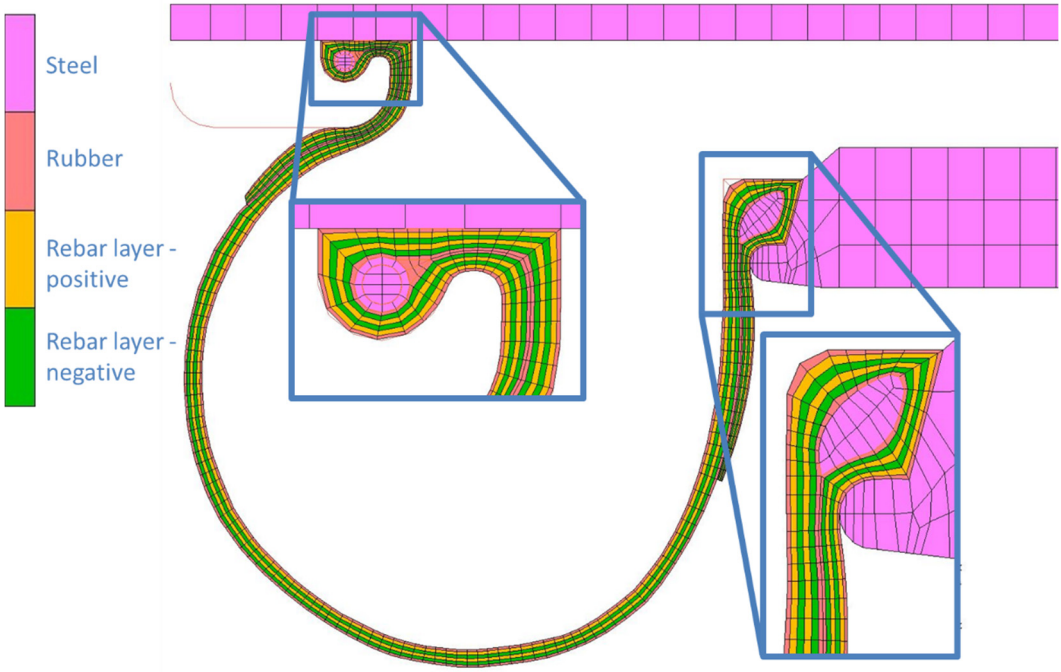

Figure 8-17: Detailed model for damage evaluation

This model is based upon the model used only for the simulation of stiffness (Figure 8-16). However, this time, the inner and outer rubber layer were not ignored. This resulted in an even higher number of elements, and since the rotation of 15° subdivisions did not work due to the high distortion of the elements, a 10°x36 rotation had to be used. Another point is the area between foldover elements and

standard elements. Between those, there is a small double layer of rubber elements, which undergo large deformations due to their low stiffness compared to the rubber-cord composite elements. These large deformations combined with the huge number of elements result in enormous simulation times. Other than that, the model worked relatively well. The results of air spring model A can be seen below (Table 8-42).

Model A	Axial Force [kN]	%	Axial Stiffness [N/mm]	%	Lateral Stiffness [N/mm]	%	Torsional Stiffness [Nm/°]	%
Clamping Ring - Detail	152.9		916.5		217.8		893.8	
Final Detailed Model	154.3	100.9	919.4	100.3	195.6	89.8	945.3	105.8

Table 8-42: Simulation results of the final detailed model compared to the model with completely modelled clamping ring area

The results yielded by the final detailed model are compared to the model with completely modelled clamping ring area, since they share a fully modelled clamping ring area. As shown in the table above (Table 8-42), the axial force increased slightly because the rubber elements on both sides of the composite elements underwent a larger deformation than the elements used in prior models. This increased the effect of the modelled clamping ring area shown in chapter 8.2.6. The lateral stiffness decreased by 10 % whereas the torsional stiffness increased by about 6 %. The simulation was a little more unstable than before, but it still worked and produced relatively good results. The model should be suitable for future damage evaluation.

8.3 Results

This chapter offers a short summary of the simulations and illustrates the influence that specific variations have on the stiffness. These influences will be classified into three groups: negligible, minor and major.

8.3.1 Axial Stiffness

The only major influence on the axial stiffness was the variation of the rebar angle, which resulted in deviations of up to 40 %, depending on the model and its standard rebar angle.

Minor influences include the number of cord strings and the angle of the foldover at the rim. None of these led to a deviation in excess of 3 %.

The rest of the variations are negligible for the axial stiffness, as they are all below 1.5 % deviation.

8.3.2 Lateral Stiffness

Major influences on the lateral stiffness were the rebar angle with a deviation of up to 28 %, as well as the length and the angle of the clamping ring with a simulated deviation of up to 12 % and a suspected deviation of even greater proportions, depending on the change of contact area at the clamping ring. Furthermore, with its 18 % deviation the variation of the stiffness of the second section of the cord material model has to be classified as a major influence, too - as does the number of cord strings with up to 9 %.

Minor influences include the length of the foldover at the rim, the variation of the length of section 1 of the cord material and the material model of the rubber.

The angle variation of the foldover at the rim and the variation of the stiffness of the cord material model's section 1 are negligible influences.

8.3.3 Torsional Stiffness

Finally, the major influences on the torsional stiffness are the rebar angle with up to 60 % deviation, the variation of the stiffness of the second section of the cord material with a deviation of 16 - 24 % and the length variation of the foldover at the rim with up to 14 %.

Minor influences include the number of cord strings and the length of the foldover at the clamping ring.

The rest of the variations were negligible for the torsional stiffness.

9 Conclusion and Future Perspectives

As the previous chapters showed, the two main goals set out in chapter 1.1 were achieved.

Firstly, the standard simulation model was developed on the basis of prior models. This simplified model offers fast simulation results and relatively high accuracy. As such, it fulfills requests for a more efficient and less time-consuming development process of new air spring types and models, demands which have repeatedly been put forward by manufacturers in recent years. The manifold tests done with this model also shed a light on the large number of different factors influencing the stiffness of an air spring, making the guesswork previously associated with this part of the manufacturing process a thing of the past. The new insight gained with the help of the simplified model was then put to use during the development of the considerably more detailed simulation model required for the damage evaluation and lifespan estimation, which is planned for the future. The development process consisted of multiple stages, leading all the way from the simplified first model to the current one, where the level of development is high enough to pronounce the simulation model ready for use.

For the future development of the simulation model and consequently the design and production of new air spring types, it would be both interesting and useful to see how actual air springs based on at least some of the simulated variations perform in real life, outside the simulations. Building and evaluating these air springs will help determine if the simulations were accurate. In turn, this process, if successful, can help strengthen the position of FE-simulations in the development of new air springs in the industry.

Since there was no measurement data available at the time this work was conducted, another interesting area of research would be the verification of air spring model C's simulation results for the torsional stiffness.

Further steps in the current research field should be the use of the detailed model for the demanded lifespan estimation and the further development of detailed submodels, if necessary.

10 List of References

Air Spring Designs - Secondary Suspension Systems, Contitech AG. (n.d.). Retrieved from http://www.contitech.de/pages/produkte/luftfedersysteme/schienenfahrzeuge/produkte_sekundaer_en.html

ContiTech AG. (2006). *Primary and Secondary Suspension Systems for Rail Vehicles.* Retrieved April 18, 2015, from http://www.services-motor.no/filemanager/download_file/file/212384.pdf/Conti%20Produktkatalog%202.pdf

GMT GmbH. (2008, November 04). *Physikalisch-Mechanische Eigenschaften Cordmischung*.

GMT GmbH. (2010, June 21). *Primär- und Sekundärfederung - Schienenfahrzeuge.* Retrieved April 21, 2015, from http://www.gmt-gmbh.de/upload/Kataloge/Schienenfahrzeugtechnik_neu.pdf

Haigermoser, A. (2002, July). Schienenfahrzeuge Vorlesungsskriptum. Graz, Austria: TU Graz, Institute of Lightweight Design.

Lehrstuhl Physikalische Chemie Universität Köln. (2009). *Gummielastizität.* (L. f. Köln, Ed.) Retrieved May 16, 2015, from Versuche im physikalisch - chemischen Praktikum für Fortgeschrittene: http://strey.pc.uni-koeln.de/fileadmin/user_upload/Download/Gummielastizitaet_final_12052009.pdf

MSC Marc Mentat. (2011, September). Basic Nonlinear Analysis using Marc and Mentat - MAR101 Course Notes.

MSC Software Corporation. (2012). Marc 2012 - User's Guide. Santa Ana, CA, USA.

MSC Software Corporation. (2012). Marc 2012 - Volume A: Theory and User Information. Santa Ana, CA, USA.

MSC Software Corporation. (2012). Marc 2012 - Volume B: Element Library. Santa Ana, CA, USA.

Okamoto, I. (1998, December). *How Bogies Work*. Retrieved April 13, 2015, from http://www.jrtr.net/jrtr18/pdf/f52_technology.pdf

Own Picture. (n.d.).

Pahl, H. J. (2002). *Luftfedern in Nutzfahrzeugen.* LFT Luftfedertechnik.

PCI Nylon. (2011). *Polyamide 6.6*. Abgerufen am 17. May 2015 von http://pcinylon.com/index.php/markets-covered/polyamide-66

Prehofer, B. (2014, December 10). Sekundärfedersysteme. Graz, Austria: TU Graz, Institute of Lightweight Design.

Puso, M., & Laursen, T. (2003, October 30). *A Mortar Segment-to-Segment Frictional Contact Method for Large Deformations.* (L. L. Laboratory, Ed.) Retrieved April 22, 2015, from https://e-reports-ext.llnl.gov/pdf/302054.pdf

Railway Technical Web Pages. (1998). Retrieved April 17, 2015, from http://www.railway-technical.com/suspen.shtml

Röthemeyer, F., & Sommer, F. (2006). *Kautschuk Technologie.* München: Carl Hanser Verlag.

Secondary Suspension Systems - Suspension Systems for Rail Vehicles, Contitech AG. (n.d.). Retrieved April 18, 2015, from http://www.contitech.de/pages/produkte/luftfedersysteme/schienenfahrzeuge/sekundaerfederung_en.html

Shetty, K. (2013, 06 06). *Segment to Segment Contact in Marc.* Retrieved 06 07, 2015, from MSC SimAcademy: http://www.mscsoftware.com/support/files/SimAcademy/wm217/SimAcademy_Presentation_Segment_to_segment_contact_in_Marc.pdf

Stumpf, H. (1997). *Handbuch der Reifentechnik.* Wien: Springer.

Talasz, M. (2013). *Simulation der Bauteilsteifigkeit eines Elastomer-Faser-Verbundes.* Graz: TU Graz, Institute for Lightweight Design.

Technische Universität Berlin. (n.d.). *Vorlesungsskriptum FEM2.* (T. U. Berlin, Ed.) Retrieved July 12, 2015, from http://mech2.pi.tu-berlin.de/weinberg/Lehre/fem2/Chapter4.pdf

Wahl, G. (2010, September). Charakterisierung von Festigkeitsträgern. Hannover.

11 List of Figures

12 List of Tables

13 Abbreviations

A_{eff}	Effective area
c	Spring stiffness
F	Spring force
FE	Finite element
n	Polytropic exponent
$p = p_a + p_i$	Absolute pressure
p_a	Pressure outside
p_i	Pressure inside (the air spring)
V	Volume
z	Translation in vertical direction
mm	Millimetres
MPa	Megapascal
GPa	Gigapascal
RBE	Rigid body elements
2d	2-dimensional
3d	3-dimensional
ε	Nominal engineering strain
ε’	True strain
σ	Stress
L_0	Original length

L_x	Deformed length
$\Delta L=L-L_0$	Length change
m	Meters
g	Gram
cm^3	Cubic centimetre
°	Degrees
Θ_1	Rebar angle of layer 1
Θ_2	Rebar angle of layer 2
Θ_x	Absolute rebar angle
MS	Microsoft
Nm	Newton meter
kN	Kilonewton
N	Newton

14 Appendix

Appendix 1: Measurements of the Rebar Angles along the Strap Length of Air Spring: Model B

Distance from inner Wire-Core [mm]	Angle of positive Cord Layerθ_1 [°]	Angle of negative Cord Layerθ_2 [°]	Absolute Cord – Angle θ_x [°]
18	19	-18	18.5
53	19	-21	20.0
88	20	-21	20.5
123	23	-20	21.5
158	27	-24	25.5
193	32	-31	31.5
228	35	-37	36.0
263	41	-41	41.0
298	45	-46	45.5
333	45	-51	48.0
368	46	-47	46.5
403	40	-46	43.0
438	40	-43	41.5
473	43	-34	38.5

Appendix 2: Measurements of the Rebar Angles along the Strap Length of Air Spring: Model C

Distance from inner Wire-Core [mm]	Angle of positive Cord Layerθ_1 [°]	Angle of negative Cord Layerθ_2 [°]	Absolute Cord – Angle θ_x [°]
11	8	-5	6.5
30	8	-6	7
49	8	-6	7
70	8	-7	7.5
91	9	-7	8
111	12	-7	9.5
133	14	-7	10.5
154	15	-8	11.5
173	16	-10	13

202	15	-12	13.5
217	13	-14	13.5
238	14	-14	14
255	15	-13	14
280	13	-15	14
305	14	-15	14.5
331	13	-14	13.5
344	13	-11	12
358	11	-13	12

Appendix 3: Simulation of axial stiffness at different pressure levels: Model B

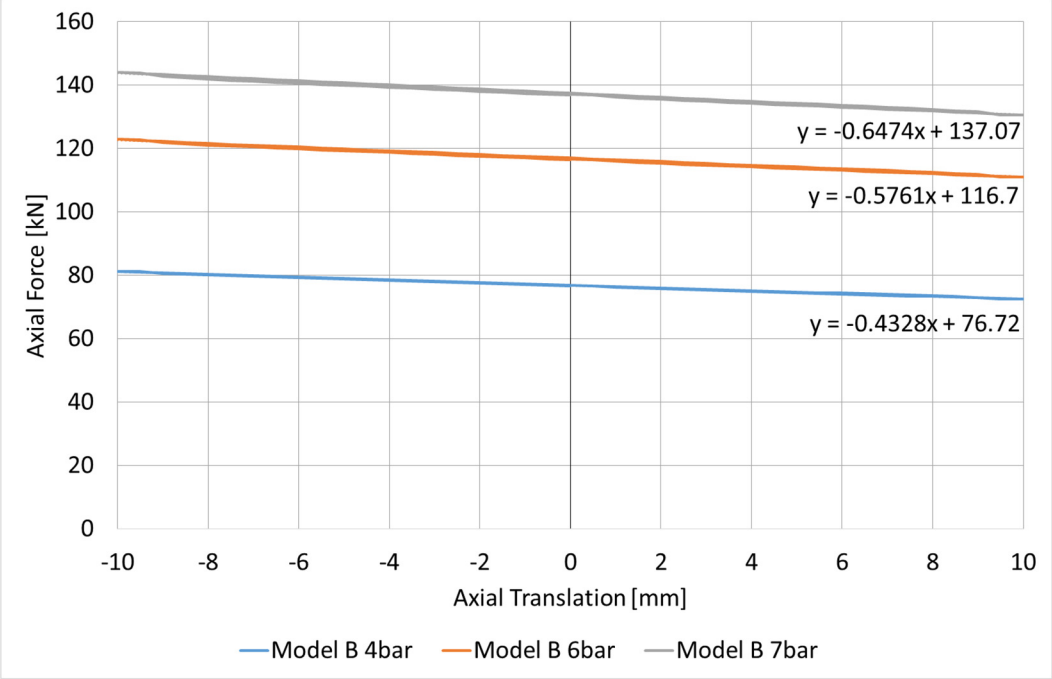

Appendix 4: Simulation of lateral stiffness at different pressure levels: Model B

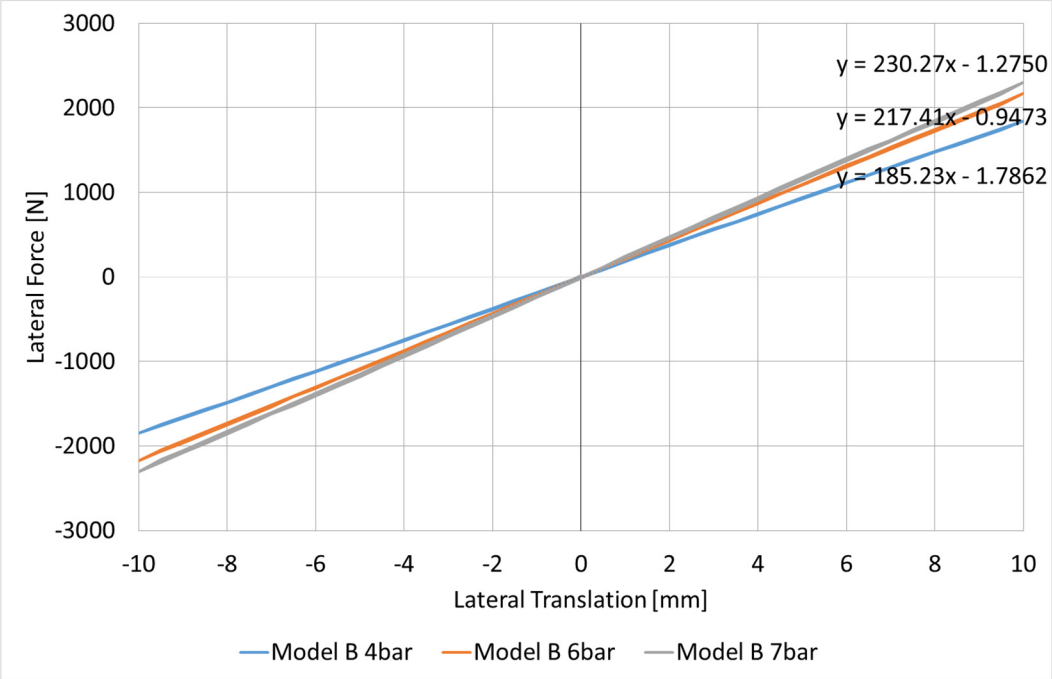

Appendix 5: Simulation of torsional stiffness at different pressure levels: Model B

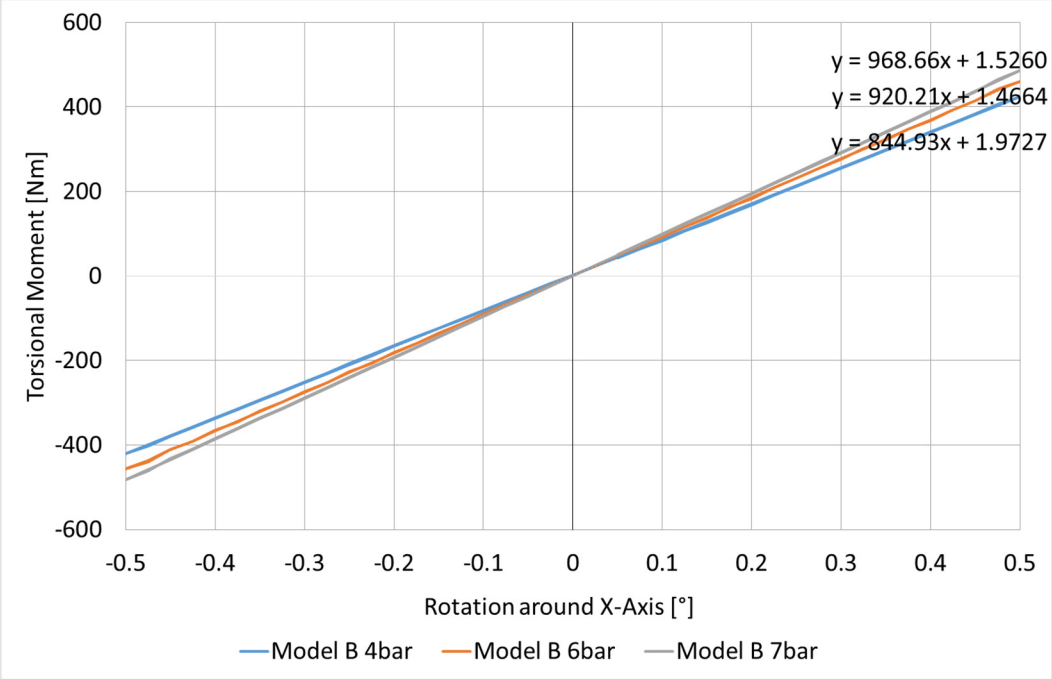

Appendix 6: Simulation of axial stiffness at different pressure levels: Model C

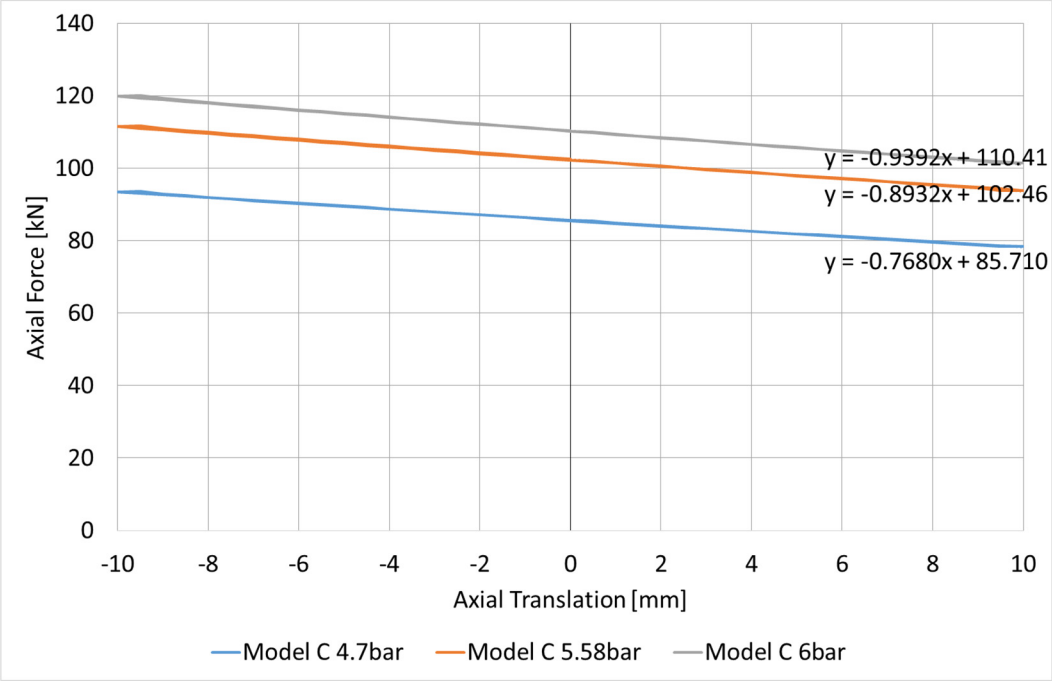

Appendix 7: Simulation of lateral stiffness at different pressure levels: Model C

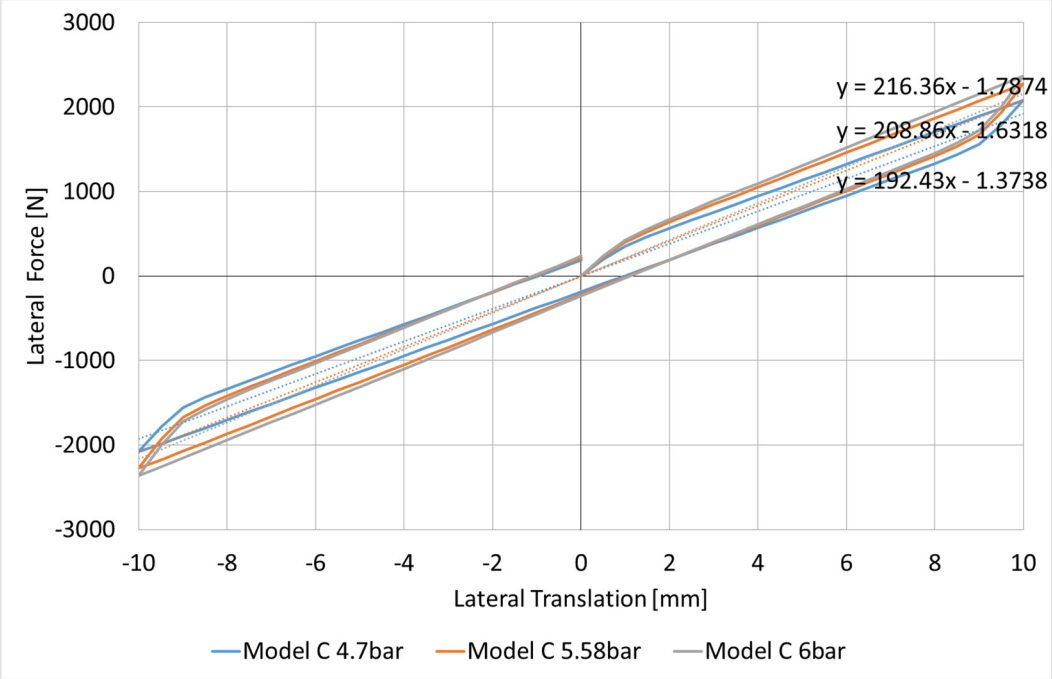

Appendix 8: Simulation of torsional stiffness at different pressure levels: Model C